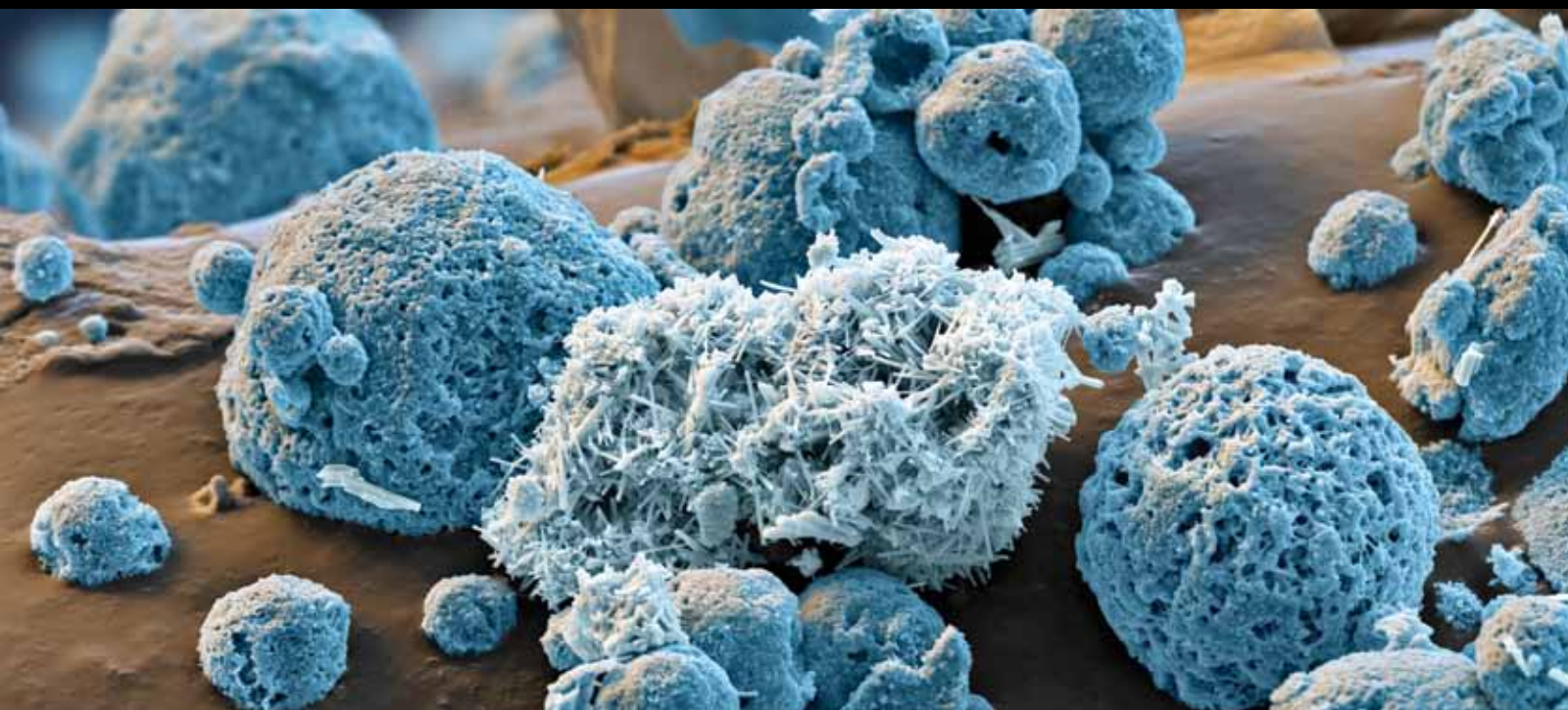


Electrocatalysis: Fundamentals and Applications

Guest Editors: Carlos F. Zinola, Maria E. Martins, Elena Pastor Tejera,
and Newton Pimenta Neves Jr.





**Electrocatalysis:
Fundamentals and Applications**

International Journal of Electrochemistry

**Electrocatalysis:
Fundamentals and Applications**

Guest Editors: Carlos F. Zinola, Maria E. Martins,
Elena Pastor Tejera, and Newton Pimenta Neves Jr.



Copyright © 2012 Hindawi Publishing Corporation. All rights reserved.

This is a special issue published in "International Journal of Electrochemistry." All articles are open access articles distributed under the Creative Commons Attribution License, which permits unrestricted use, distribution, and reproduction in any medium, provided the original work is properly cited.

Editorial Board

Maria Carmen Arévalo, Spain
Shen-Ming Chen, Taiwan
Abel César Chialvo, Argentina
Jean-Paul Chopart, France
A. Rodrigues de Andrade, Brazil
Sergio Ferro, Italy
Gerd-Uwe Flechsig, Germany
Rubin Gulaboski, Germany
Shengshui Hu, China
Mehran Javanbakht, Iran
Jiye Jin, Japan

Emilia Kirowa-Eisner, Israel
Boniface Kokoh, France
Emmanuel Maisonhaute, France
Grzegorz Milczarek, Poland
Valentin Mirceski, Macedonia
Mohamed Mohamedi, Canada
Angela Molina, Spain
Davood Nematollahi, Iran
K. I. Ozoemena, South Africa
María Isabel Pividori, Spain
Miloslav Pravda, Ireland

Manfred Rudolph, Germany
Benjamín R. Scharifker, Venezuela
Auro Atsushi Tanaka, Brazil
Germano Tremiliosi-Filho, Brazil
Hamilton Varela, Brazil
Jay D. Wadhawan, UK
Jose H. Zagal, Chile
Sheng S. Zhang, USA
Jiujun Zhang, Canada
Xueji Zhang, USA

Contents

Electrocatalysis: Fundamentals and Applications, Carlos F. Zinola, Maria E. Martins, Elena Pastor Tejera, and Newton Pimenta Neves Jr.

Volume 2012, Article ID 874687, 2 pages

Ethanol Electrooxidation on Pt with Lanthanum Oxide as Cocatalyst in a DAFC, T. A. B. Santoro, A. Oliveira Neto, C. A. L. G. de O. Forbicini, M. Linardi, J. L. Rodríguez, and E. Pastor

Volume 2012, Article ID 674150, 6 pages

Influence of Synthesis pH on Textural Properties of Carbon Xerogels as Supports for Pt/CXs Catalysts for Direct Methanol Fuel Cells, C. Alegre, M. E. Gálvez, D. Sebastián, R. Moliner, and M. J. Lázaro

Volume 2012, Article ID 267893, 9 pages

Carbon-Supported Fe Catalysts for CO₂ Electroreduction to High-Added Value Products: A DEMS Study: Effect of the Functionalization of the Support, S. Pérez-Rodríguez, G. García, L. Calvillo, V. Celorrio, E. Pastor, and M. J. Lázaro

Volume 2011, Article ID 249804, 13 pages

Investigation of the Performance of Au_{core}-Pd_{shell}/C as the Anode Catalyst of Direct Borohydride-Hydrogen Peroxide Fuel Cell, Hong Wang, Ying Wang, Xianyou Wang, Peiyong He, Lanhua Yi, Wei Yi, and Xue Liu

Volume 2011, Article ID 129182, 7 pages

Use of Dendrimers during the Synthesis of Pt-Ru Electrocatalysts for PEM Fuel Cells: Effects on the Physical and Electrochemical Properties, J. C. Calderón, L. Calvillo, M. J. Lázaro, and E. Pastor

Volume 2011, Article ID 564828, 7 pages

Investigation of IrO₂/Pt Electrocatalysts in Unitized Regenerative Fuel Cells, V. Baglio, C. D'Urso, A. Di Blasi, R. Ornelas, L. G. Arriaga, V. Antonucci, and A. S. Aricò

Volume 2011, Article ID 276205, 5 pages

Electrocatalytic Reduction of Hydrogen Peroxide on Palladium-Gold Codeposits on Glassy Carbon: Applications to the Design of Interference-Free Glucose Biosensor, Elena Horozova, Totka Dodevska, Nina Dimcheva, and Ruska Mussarlieva

Volume 2011, Article ID 697698, 8 pages

The Electrochemical Development of Pt(111) Stepped Surfaces and Its Influence on Methanol Electrooxidation, E. Teliz, V. Díaz, R. Faccio, A. W. Mombrú, and C. F. Zinola

Volume 2011, Article ID 289032, 9 pages

Some Applications of Bayes' Rule in Probability Theory to Electrocatalytic Reaction Engineering, Thomas Z. Fahidy

Volume 2011, Article ID 404605, 5 pages

Chiral Recognition of Amino Acids by Magneto-electrodeposited Cu Film Electrodes, Iwao Mogi and Kazuo Watanabe

Volume 2011, Article ID 239637, 6 pages

Editorial

Electrocatalysis: Fundamentals and Applications

Carlos F. Zinola,¹ Maria E. Martins,² Elena Pastor Tejera,³ and Newton Pimenta Neves Jr.⁴

¹ *Electrochemical Engineering Group, School of Sciences and School of Engineering, Fundamental Electrochemistry Laboratory, J. R. Rodó No. 1843, UDELAR, C.P.11100 Montevideo, Uruguay*

² *Electrocatalysis Laboratory, INIFTA, UNLP, C.C. 16, Suc. 4, 1900 La Plata, Argentina*

³ *Departamento de Química-Física, P.O. Box 38207 ULL, La Laguna, Spain*

⁴ *Laboratório de Hidrogênio, Instituto de Física "Gleb Wataghin", Universidade Estadual de Campinas (UNICAMP), Campinas, SP, Brazil*

Correspondence should be addressed to Carlos F. Zinola, fzinola@fcien.edu.uy

Received 28 December 2011; Accepted 28 December 2011

Copyright © 2012 Carlos F. Zinola et al. This is an open access article distributed under the Creative Commons Attribution License, which permits unrestricted use, distribution, and reproduction in any medium, provided the original work is properly cited.

Electrocatalysis is a special field in Electrochemistry that has gained a special growth after the late eighties due to the application of new hybrid techniques. However, most of the applications have run for academic purposes but not for technical uses in the industry. Nowadays, the application of new concepts of electrocatalysis for industrial electrochemical processes has appeared as a necessity and not only attracting attention for chemists but for engineers. Therefore, industrial electrocatalytic processes have only been presented in the literature from the chemical engineering point of view with few further electrochemical explanations and mainly during the late seventies. The design and preparation of an electrocatalyst (electrodes for technological uses) are based on new concepts such as a controlled surface roughness, atomic topographic profiles, defined catalytic centre sites, atomic rearrangements, and phase transitions in the course of the electrochemical reactions.

Maybe the best interpretation of electrocatalysis is due to A. J. Appleby as an electrochemical reaction with an adsorbed species, either as reactant and/or product, which can change the kinetics of the reaction and in some cases also the mechanism. Although the old conception of electrocatalysis is mainly related to an experimental field of electrochemistry when using platinum-type metals, the advances in theory and modeling are main keys for a successful interpretation of the data.

The perspective and limitations of electrocatalysis in the laboratory together with their theoretical implications are also presented to give the readers a clearer view of

the problems inside electrocatalytic reactions. This special issue also gathers the experiences of different authors who have worked on the principles of electrocatalysis with relevancy to experimental situations of particular importance in electrochemical engineering. This is the case of the work by T. Fahidy in the use of the Bayer's rule for an electrochemical reactor in order to avoid the possibility of reactor breakdown, reactor's safety, and environmental considerations well beyond purely scientific quantities.

One of the most important features of electrocatalysis arises from the different electrode kinetics using different crystallographic orientations for the electrode surface. A cathodic treatment develops (111) stepped planes similarly to the electrofacetting performed after applying the square wave program shown with X-ray diffraction patterns. These arrangements are well explained in the paper by C. Zinola, using combined techniques and particularly studying the methanol electrooxidation reaction. In spite of being most of the electrocatalytic reactions studied in the scientific community only for rather simple species, some of them involve low-weight amino acids, showing changes in the adsorbed configurations and chiral responses when the nature of the electrode surface is changed, as shown by K. Watanabe. Chiral behavior was clearly observed as an oxidation current difference between the enantiomers of alanine, aspartic acid, and glutamic acid.

The fast and contemporary advances in electrocatalysis have been already treated in other books but only considering the progress in the application of surface science and

ultrahigh vacuum techniques to electrochemistry with no extrapolation to the possible industrial applications of these findings. Some combined techniques, such as differential electrochemical mass spectrometry, show the possibility of the continuous analysis of an electrode reaction with the detection of volatile or gaseous products in the course of the electrochemical reaction as shown by M. J. Lázaro for carbon dioxide electroreduction. Differential electrochemical mass spectrometry studies showed that the carbon support degradation, the distribution of products, and the catalytic activity toward the carbon dioxide electroreduction depend significantly on the surface chemistry of the carbon support.

There are various applications of electrocatalysis for technological electrochemical reactions, organic electrosynthesis, galvanoplasty, electrode sensors, fuel cells, batteries preparations, and so forth. Some of them are presented here in order to give an insight into the possibilities of this science. Thus, the avoiding of interferences in the case of hydrogen peroxide electroreduction has been gained using alloys such as palladium-gold electrodes as reported by R. Mussarlieva with application for glucose biosensors. The surface topography of the electrode modified with Pd + Au mixed in proportions 90:10, exhibiting optimal combination of sensitivity and linear dynamic range towards hydrogen peroxide electrochemical reduction.

However, it seems that the main application is the case of fuel cells and one of the scopes is the possibility of long-lasting experiments without contamination or poisoning of the electrode surfaces. A. S. Aricó studied the continuous use of IrO₂/Pt electrocatalysts in fuel cells with good results that are also presented in this special issue. The IrO₂/Pt composition of 14/86 showed the highest performance for water electrolysis and the lowest one as fuel cell. Polymer electrolyte fuel cells are one of the most used devices for low-to-medium power density sizes. However, platinum electrocatalysts are often changed to platinum/ruthenium alloys because of the application of the electrocatalytic Langmuir-Hinshelwood surface mechanism. In this issue the use of dendrimers during the synthesis of platinum/ruthenium electrocatalysts for polymer electrolyte fuel cells shows interesting results that are strongly dependent on the physical characteristics of the alloy as presented by E. Pastor. After the activation of the catalysts by heating at 350°C, the real importance of the use of these encapsulating molecules and the effect of the generation of the dendrimer become visible. Not only the use of alloys of combined electrodeposited species offers electrocatalytic differences for fuel cell application, but also the preparation of Au core-Pd shell/C electrodes as shown by X. Liu for a direct borohydride-hydrogen peroxide fuel cell. The results show that the Au-Pd/C catalyst with core-shell structure exhibits much higher catalytic activity for the direct oxidation of NaBH₄ than pure Au/C catalyst, i.e. a direct borohydride-hydrogen peroxide fuel cell, in which the Au-Pd/C with core-shell structure is used as the anode catalyst and the Au/C as the cathode catalyst.

New advances relevant to electrocatalysis such as spectroscopic or hybrid techniques with new theoretical considerations act as a final point from them it is possible to evolve to a new projection of the electrocatalytic reaction

itself. One of the purposes of this special issue is to present the field of electrocatalysis as an interfacial approach to a dynamic and permanently changing electronic-to-ionic conductor interphase with real technical applications.

Carlos F. Zinola

Maria E. Martins

Elena Pastor Tejera

Newton Pimenta Neves Jr.

Research Article

Ethanol Electrooxidation on Pt with Lanthanum Oxide as Cocatalyst in a DAFC

**T. A. B. Santoro,^{1,2} A. Oliveira Neto,² C. A. L. G. de O. Forbicini,² M. Linardi,²
J. L. Rodríguez,¹ and E. Pastor¹**

¹Departamento de Química Física, Instituto Universitario de Materiales y Nanotecnología, Universidad de La Laguna, C/Astrofísico Francisco Sánchez s/n, 38071 La Laguna, Spain

²Instituto de Pesquisas Energéticas e Nucleares (IPEN), CNEN-SP, Avenida Professor Lineu Prestes 2242, Cidade Universitária, 05508-900 São Paulo, SP, Brazil

Correspondence should be addressed to T. A. B. Santoro, thaisabsantoro@yahoo.com.br

Received 1 May 2011; Revised 1 November 2011; Accepted 24 November 2011

Academic Editor: Newton Pimenta Neves Jr.

Copyright © 2012 T. A. B. Santoro et al. This is an open access article distributed under the Creative Commons Attribution License, which permits unrestricted use, distribution, and reproduction in any medium, provided the original work is properly cited.

Electrocatalytic activity toward ethanol electrooxidation of Pt particles in PtLa/C catalysts with different Pt : La ratios has been studied with different electrochemical and spectroscopic techniques, and the results were compared to those of Pt/C catalyst. Significant enhancement in the electrocatalytic activity has been achieved by depositing the Pt particles with lanthanum oxides/hydroxides using an alcohol reduction method. Compared to Pt/C catalyst, PtLa/C materials exhibit a lower onset potential and a higher electron-transfer rate constant for the investigated reaction. These studies illustrate the possibility of utilizing Pt/C with La oxides/hydroxides as electrocatalyst for direct alcohol fuel cells (DAFCs).

1. Introduction

In catalysis, numerous applications can be found for lanthanum oxide. It is used as support for metals that catalyze reactions such as methanol decomposition, ammonia oxidation, and methane dry reforming [1–4]. It is also recognized as an active and selective catalyst for several processes [5–7]. It has been shown that lanthanum oxides can substantially modify the chemical behaviour of highly dispersed metal catalysts [6]. In this system, several chemical species are present such as La_2O_3 or $\text{La}(\text{OH})_3$ [8], which could be implied in the electrooxidation of alcohols like methanol or ethanol, for example.

In the past decades, direct alcohol fuel cells (DAFCs) have received much attention due to their possible applications in transportation and portable electronic devices [9–15]. Methanol or ethanol can be directly used as fuel in DAFCs without external reformer. Ethanol has higher energy density compared with methanol [15, 16] and it is more attractive as fuel for DAFCs: it is safer and can be produced in great quantities from biomass. However, the ethanol electrooxidation has slow reaction kinetics that is still the main problem for its

direct application in an ethanol fuel cell (DEFC). A lot of work has been done with the purpose to prepare catalysts with sufficiently high catalytic activity and CO tolerance for ethanol electrooxidation. It is accepted that the coexistence of some metal oxides with Pt can improve the catalytic activity of Pt-based catalysts for this reaction.

In the present work, the effect of the addition of La oxides/hydroxides to Pt/C is investigated for ethanol electrooxidation [16]. PtLa/C catalyst powders with different compositions were prepared and compared to Pt/C. X-ray diffraction (XRD), cyclic voltammetry (CV), steady-state polarization experiments, and Fourier transform IR spectroscopy (FTIRS) were employed as characterization techniques to provide information on the physicochemical properties as well as on the catalytic activity of these materials towards the electrochemical reactions of ethanol.

2. Experimental

PtLa/C with different Pt : La atomic ratios and Pt/C catalysts were prepared by an alcohol reduction process in alkaline

environment (KOH/Pt:La molar ratio of 8) using Vulcan XC 72R as support. Metal precursors were $\text{H}_2\text{PtCl}_6 \cdot 6\text{H}_2\text{O}$ (Aldrich) and $\text{LaCl}_3 \cdot x\text{H}_2\text{O}$ (Aldrich), and ethylene glycol (Merck) was employed as solvent and reducing agent [17–19]. The reduction potential of La is about 3.5 V more negative than that of Pt [20]. Therefore, it is not possible to reduce La(III) ions to La^0 in the conditions of the chosen methodology. Thus, in alkaline medium La(III) ions are deposited as lanthanum oxide and/or hydroxide. On the other hand, Pt (IV) ions can be reduced by ethylene glycol to metallic Pt nanoparticles, which are placed on the carbon support. Characterization of prepared materials by XRD and transmission electron microscopy (TEM) has been described in a previous work where it was proved that La is deposited in the form of oxides and hydroxides by this procedure [21]. The diffractograms of PtLa/C electrocatalysts showed the peaks characteristic of fcc Pt and the presence of the contributions of La_2O_3 at 26°, 29°, 34°, and 56° (JPDF 000–83–1354) and those of $\text{La}(\text{OH})_3$ at 27°, 31°, and 43° (JPDF 000–75–1900) [21, 22].

Dispersive X-ray (EDX) analysis using a scanning electron microscope Philips XL30 with a 20 keV electron beam and provided with EDAX DX-4 microanalyser was used to establish the real composition of the materials investigated in the present paper.

The electrochemical measurements for the ethanol oxidation reaction were carried out with a three-electrode flow cell. A hydrogen electrode in the electrolyte solution (RHE) was used as reference and a glassy carbon as counter electrode. The working electrode was prepared with 40 μL of a homogeneous mixture of 4 mg of powder electrocatalyst, ultrasonically dispersed in 1 mL of Milli-Q ultrapure water, and 38 μL of Nafion (Aldrich, 5 wt.%) [23]. This ink was deposited onto a glassy carbon polished surface disc, with geometric area of 0.28 cm^2 , and dried in N_2 atmosphere before its utilization.

Electrochemical experiments were performed in a 1 mol L^{-1} $\text{CH}_3\text{CH}_2\text{OH}$ + 0.5 mol L^{-1} H_2SO_4 solution for both PtLa/C and Pt/C electrocatalysts. Cyclic voltammograms (CVs) were recorded in the 0.05–0.90 V potential range at 0.01 Vs^{-1} and the current-time curves at a constant potential of 0.55 V. Activation pretreatment by potential cycling between 0.05 and 0.40 V in the base electrolyte (H_2SO_4 0.5 mol L^{-1}) was applied until a stabilized CV was achieved (the upper potential was set to 0.40 V in order to avoid La dissolution from the alloy). A potentiostat/galvanostat Autolab PGSTAT30 was used for these studies.

Electroactive area was calculated from the hydrogen adsorption/desorption region assuming 0.210 mC/cm^2 for the oxidation of an H adsorbed monolayer. Density current values in the paper are calculated with respect to the electroactive areas.

Fourier transform IR spectroscopy (FTIRS) experiments were carried out with a Bruker Vector 22 spectrometer equipped with an MCT (mercury cadmium telluride) detector. A small glass flow cell with a 60° CaF_2 prism at its bottom was employed. For each spectrum, 128 interferograms were collected at selected potentials with a resolution of 8 cm^{-1} , by applying 0.05 V single potential steps from a reference

TABLE 1: Pt:La ratios from EDX analysis and current density from chronoamperometric curves obtained at 0.55 V.

Electrocatalysts	Atomic ratios (Pt:La)	$\text{CV}_{0.55}$ (mA cm^{-2})
PtLa 30:70	37:63	0.288
PtLa 50:50	57:43	0.213
Pt	—	0.092

potential (0.05 V) in the positive going direction. Spectra are represented as the ratio R/R_0 , where R and R_0 are the reflectance at the sample and reference spectra, respectively [11]. In this way, positive bands represent the loss and negative bands the gain of species at the sampling potential.

The working electrodes for FTIRS consist of a thin layer of a certain amount of the metal/C catalysts deposited over a polycrystalline gold disk. The geometric area of the disk was 0.85 cm^2 . 40 μL of the homogeneous mixture of powder electrocatalyst was pipetted on the top of the gold disk and dried at ambient temperature. The electrolyte was 0.1 mol L^{-1} HClO_4 containing 1.0 mol L^{-1} of ethanol.

3. Results and Discussion

The real compositions of the catalysts were established from EDX analysis and results are summarized in Table 1. The measured atomic ratios of PtLa/C were close to nominal ones, so it can be deduced that Pt and La oxides/hydroxides were successfully loaded on the carbon support without metal loss.

The cyclic voltammograms for ethanol oxidation on PtLa/C and Pt/C electrodes in 1.0 mol L^{-1} $\text{CH}_3\text{CH}_2\text{OH}$ + 0.5 mol L^{-1} H_2SO_4 solution at room temperature are given in Figure 1. It can be observed that the CVs exhibit the irreversible nature of the ethanol electrooxidation that is characteristic of Pt-based catalysts. The onset for ethanol electrooxidation occurs at approximately 0.50 V but a shift to more negative potentials is clearly apparent when introducing La species in the material, especially in the case of the PtLa/C (30:70) catalyst. Moreover, different maximum current densities are achieved during the positive potential scan. The highest current density is apparent for PtLa/C (30:70) catalysts, and it is about twice that obtained for Pt/C. The PtLa/C (50:50) electrocatalyst also increases the catalytic activity, by a factor of 1.5 when compared to Pt/C. Therefore, the activity order towards ethanol electrooxidation can be established as follows: PtLa/C (30:70) > PtLa/C (50:50) > Pt/C. Then, the content of La oxides/hydroxides in the PtLa/C catalysts affects the catalytic activity for ethanol electrochemical oxidation allowing the oxidation at lower potentials and increasing the current density values.

Considering that ethanol does not react on La oxides/hydroxides, from these data it can be concluded that the addition of La oxides/hydroxides significantly increases the catalytic activity of Pt towards ethanol electrooxidation. Probably this result is related to the improvement of the kinetics of CO and other adspecies oxidation on Pt through

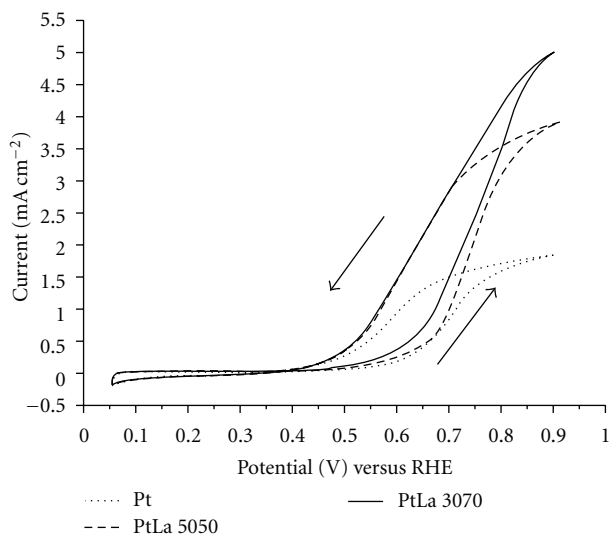


FIGURE 1: Cyclic voltammograms for ethanol electrooxidation on Pt/C, PtLa/C (50:50), and PtLa/C (30:70) electrocatalysts in $1.0 \text{ mol L}^{-1} \text{ CH}_3\text{CH}_2\text{OH} + 0.5 \text{ mol L}^{-1} \text{ H}_2\text{SO}_4$ in the 0.05 to 0.90 V potential range at room temperature. Scan rate: 0.010 Vs^{-1} .

a bifunctional mechanism [24] (as no alloy is formed in these materials according to previous results in [21]).

To compare the cyclic voltammetric and the potentiostatic responses of the electrocatalysts, chronoamperometric curves in $1.0 \text{ mol L}^{-1} \text{ CH}_3\text{CH}_2\text{OH} + 0.5 \text{ mol L}^{-1} \text{ H}_2\text{SO}_4$ were recorded at 0.55 V during 900 s. Results are given in Figure 2 and stable current density values summarized in Table 1. The same trend previously established from the CVs is observed.

All current-time curves display an initial fast current drop in the first 90 seconds followed by a slower rise only apparent for PtLa materials. This observation could be explained assuming that a fast poisoning of the Pt surface takes place in the first instants, but, in the presence of La oxides/hydroxides, slower oxidation of the poisons occurs to a certain extent at 0.55 V. Thus, the current increases until achieving a stable value when the concurrence between both processes (poisoning and oxidation of the adspecies) acquires the equilibrium. In other words, PtLa/C electrocatalysts are more resistant to the poisoning caused by ethanol intermediate adspecies causing a significant increase of performance with the augment of La oxides/hydroxides content. This behaviour could be attributed to the oxophilic character of La in $\text{La}(\text{OH})_2$ and La_2O_3 [25].

Using CeO_2 , an increment in performance was also described by Xua and coworkers [24]. They attributed the activity enhancement for alcohol electrooxidation after the addition of CeO_2 to the Pt catalysts to the bifunctional mechanism, where the formation of chemisorbed oxygen species was favoured by CeO_2 and promotes the oxidation of adsorbed carbon monoxide on the surface of Pt. Neto et al. [26] observed an improvement in ethanol electrooxidation using nanocrystalline Pt/ CeO_2 composite electrodes. From the studies of carbon monoxide oxidation over Pt- CeO_2 and Pt- SnO_2 , these authors associated the increase in the activity with the oxygen spillover from the oxides onto the Pt sites

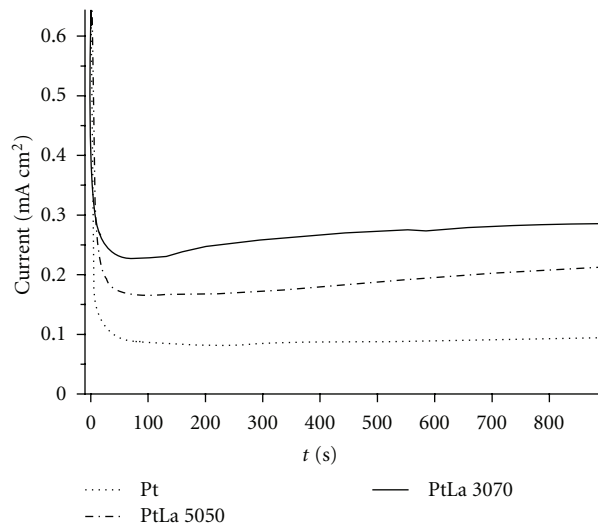


FIGURE 2: Current-time curves at 0.55 V in $1.0 \text{ mol L}^{-1} \text{ CH}_3\text{CH}_2\text{OH} + 0.5 \text{ mol L}^{-1} \text{ H}_2\text{SO}_4$ solution for Pt/C, PtLa/C (50:50) and PtLa/C (30:70) electrocatalysts.

[26]. In a similar way, it is also possible that, in our case, the release of oxygen from the surface of La oxides/hydroxides particles contributes to facilitating the oxidation of adsorbed CO and other intermediate species on the Pt surface.

To provide complementary information on the electrochemical oxidation of ethanol, Fourier transform IR spectroscopy (FTIRS) was employed as catalyst characterization technique. According to Iwasita et al. [27], possible products during ethanol electrooxidation are CO_2 , acetaldehyde, and acetic acid, although ethyl acetate could also be produced by the reaction of acetic acid with ethanol. Figure 3 presents the IR spectra acquired with p-polarized light in $1.0 \text{ mol L}^{-1} \text{ CH}_3\text{CH}_2\text{OH} + 0.5 \text{ mol L}^{-1} \text{ H}_2\text{SO}_4$ solution during the progressive ethanol electrooxidation from 0.05 V up to 0.90 V for PtLa/C (50:50) catalyst. HClO_4 was used instead of H_2SO_4 in order to avoid the bands related to the adsorption of sulphate/bisulphate species.

In Figure 3, the growing in CO_2 production is indicated by the asymmetric stretching vibration band at 2343 cm^{-1} . The positive going features at 2983 and 2901 cm^{-1} correspond to $\text{CH}_3\text{CH}_2\text{OH}$ and indicate the consumption of the alcohol in the thin layer. At 0.80 V all other contributions in the spectrum are well developed. At 1715 cm^{-1} , the stretching band of the carbonyl group ($\text{C}=\text{O}$) is observed. Both acetaldehyde and acetic acid could be responsible for this band, so it is not appropriated for identification purposes [27]. As the potential is stepped to more positive values, two other negative features at 1354 and 1278 cm^{-1} appear in the spectrum, parallel to the carbonyl band. According to Iwasita et al. [27], the spectrum of pure acetic acid presents in this region two bands due to the coupled C-O stretching and OH deformation.

These results confirm that CO_2 and acetic acid are produced during ethanol oxidation. On the other hand, the identification of acetaldehyde in the presence of comparable quantities of acetic acid is difficult. The characteristic features

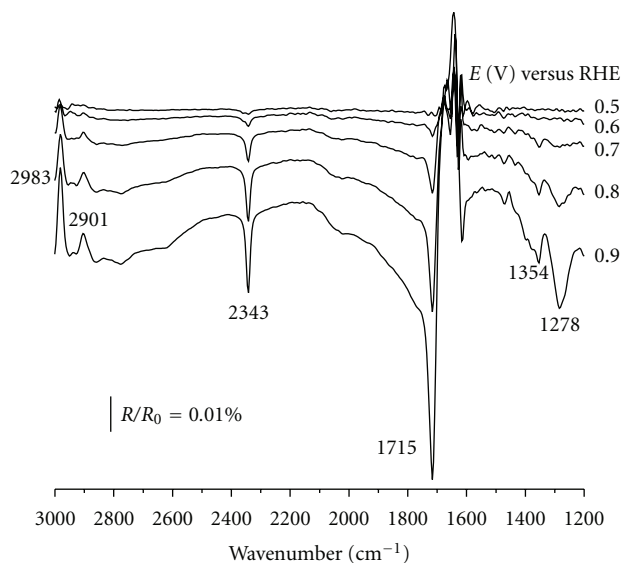


FIGURE 3: In situ FTIR spectra obtained in $1.0 \text{ mol L}^{-1} \text{ CH}_3\text{CH}_2\text{OH} + 0.1 \text{ mol L}^{-1} \text{ HClO}_4$ solution for PtLa/C (50:50) electrocatalysts. P-polarized light; resolution: 8 cm^{-1} ; $E_{\text{ref}} = 0.05 \text{ V}$.

of acetaldehyde are the C=O stretch (in the region of the signal at 1715 cm^{-1}) and the symmetric CH_3 deformation (in the region of the signal at 1354 cm^{-1}). These bands can be then strongly overlapped with those of acetic acid. Assuming that the dual-path mechanism is acting for ethanol electrooxidation, CO_2 and acetic acid can be considered as representative of the two reactions pathways (acetaldehyde is produced in the same route as acetic acid).

The acetic acid (1278 cm^{-1}) and CO_2 (2343 cm^{-1}) productions can be followed integrating their characteristic bands from the spectra in Figure 3 and plotting the result as a function of the potential. The integrated intensity values are given in Figures 4 and 5, respectively. The same procedure for spectra collection has been followed with PtLa/C (30:70) and Pt/C, and the results for their integration are also included in Figures 4 and 5.

The bands at 2343 and 1278 cm^{-1} in Figures 4 and 5 follow similar potential dependences, increasing the intensity as the sample potential is set more positive. It is also observed that the amount of both acetic acid and CO_2 rises with the increment of La oxides/hydroxides content in the catalyst. However, some differences are apparent between the two PtLa/C electrocatalysts and have to be remarked.

In general, the onset electrooxidation potential observed in the CVs in Figure 1 is related to the onset in the CO_2 production (Figure 5) in all catalysts, whereas the formation of acetic acid starts at more positive potentials (Figure 4). This result suggests that it is necessary that adsorbed species initiate their oxidation to CO_2 in order to liberate Pt sites, where ethanol molecules from the solution can further react and produce acetaldehyde and acetic acid. Although the onset potentials for both CO_2 and acetic acid are similar for the three catalysts studied, from a detailed inspection of Figures 4 and 5, it is clearly observed a faster increase in the production of both CO_2 and acetic acid in the presence of

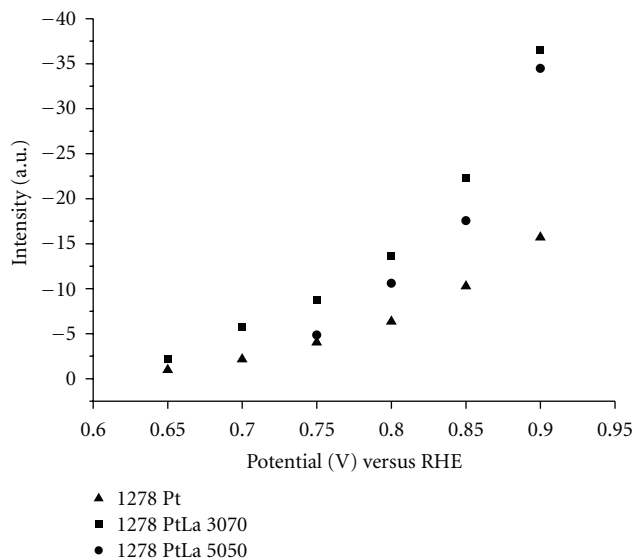


FIGURE 4: Potential dependence of the integrated band intensity (1278 cm^{-1}) from Figure 3 corresponding to acetic acid, for Pt/C, PtLa/C (50:50), and PtLa/C (30:70) electrocatalysts.

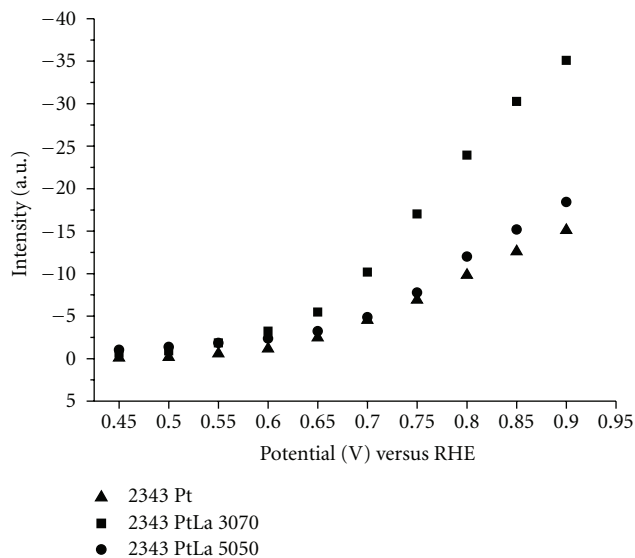


FIGURE 5: Potential dependence of the integrated band intensity (2343 cm^{-1}) from Figure 3 corresponding to CO_2 , for Pt/C, PtLa/C (50:50), and PtLa/C (30:70) electrocatalysts.

La oxides/hydroxides. In the case of Pt:La 50:50, the higher currents observed in Figure 1 with respect to Pt are due to the formation of higher amounts of acetic acid (Figure 4). For Pt:La 30:70, both CO_2 (Figure 5) and acetic acid (Figure 4) productions are enlarged with respect to Pt, but mainly CO_2 when compared with PtLa 50:50. Therefore, it seems that initially the presence of La oxides/hydroxides contributes to enhancing the catalytic activity facilitating the bulk ethanol reaction; but increasing its content in the catalyst, also the electrooxidation of adsorbed intermediates to CO_2 (and, therefore, the cleavage of the ethanol molecule) is favoured.

To produce CO_2 or CH_3COOH , $\text{CH}_3\text{CH}_2\text{OH}$ needs at least a second oxygen atom. The reaction mechanism must involve some form of adsorbed oxygen species, which probably come from La oxides/hydroxides in addition to PtOH from water splitting. Although there is an evident rise in the performance of the catalyst with the increment of La oxides/hydroxides content, this is mainly due to a faster oxidation of bulk ethanol to acetic acid, that is, without breaking the C–C bond. However, it is also shown that with appropriate amounts of La oxides/hydroxides also the efficiency to CO_2 (and, therefore, the cleavage of the molecule) can be enhanced.

4. Conclusions

The combination of electrochemical and spectroscopic techniques has allowed a comparative analysis of the behaviour of Pt/C, PtLa/C (50 : 50) and PtLa/C (30 : 70) electrocatalysts towards ethanol electrooxidation. A significant increase of performance was observed with the increment of La oxides/hydroxides content, indicating that the addition of La species improves the activity of Pt for this reaction. FTIR results show that higher amounts of acetic acid are produced during ethanol oxidation at PtLa/C (50 : 50). Also the formation of CO_2 is favoured if the La oxides/hydroxides content is raised to Pt : La 30 : 70, and, therefore, the presence of these compounds as oxygen source can favour both bulk alcohol reactions (acetic acid formation) and adsorbed species oxidation (CO_2 production).

The onset for ethanol oxidation is observed at 0.50 V, that is, in the potential range used for a DAFC. The enhancement of activity towards alcohol electrooxidation in this potential region due to the addition of La oxides/hydroxides to Pt opens a possibility to utilize these materials as electrocatalysts for these devices. However, the detection of representative amounts of acetic acid clearly indicates that the C–C bond is not completely broken and further optimization of the catalysts is needed to improve the energy efficiency of ethanol electrooxidation.

Acknowledgments

The authors thank FAPESP (Process 03/03127-0), CNPq (CTENERG 504793/2004-0), CAPES (Process 3982-07-6), MICINN (MAT2008-06631-C03-02), and ACIISI (PI2007/023) for the financial support.

References

- [1] G. Mul and A. S. Hirschon, "Effect of preparation procedures on the activity of supported palladium/lanthanum methanol decomposition catalysts," *Catalysis Today*, vol. 65, no. 1, pp. 69–75, 2001.
- [2] J. Petryk and E. Kolakowska, "Cobalt oxide catalysts for ammonia oxidation activated with cerium and lanthanum," *Applied Catalysis B*, vol. 24, no. 2, pp. 121–128, 2000.
- [3] S. Irusta, L. M. Cornaglia, and E. A. Lombardo, "Hydrogen production using Ni–Rh on La," *Journal of Catalysis*, vol. 210, no. 1, pp. 7–16, 2002.
- [4] O. V. Manoilova, S. G. Podkolzin, B. Tope et al., "Surface acidity and basicity of La," *Journal of Physical Chemistry B*, vol. 108, no. 40, pp. 15770–15781, 2004.
- [5] S. J. Huang, A. B. Walters, and M. A. Vannice, "Adsorption and decomposition of NO on lanthanum oxide," *Journal of Catalysis*, vol. 192, no. 1, pp. 29–47, 2000.
- [6] M. Traykova, N. Davidova, J. S. Tsaih, and A. H. Weiss, "Oxidative coupling of methane—the transition from reaction to transport control over La," *Applied Catalysis A*, vol. 169, no. 2, pp. 237–247, 1998.
- [7] H. Vidal, S. Bernal, R. T. Baker, G. A. Cifredo, D. Finol, and J. M. Rodríguez-Izquierdo, "Catalytic behavior of lanthana promoted Rh/SiO₂," *Applied Catalysis A*, vol. 208, no. 1–2, pp. 111–123, 2001.
- [8] L. M. Cornaglia, J. Múnera, S. Irusta, and E. A. Lombardo, "Raman studies of Rh and Pt on La," *Applied Catalysis A*, vol. 263, no. 1, pp. 91–101, 2004.
- [9] W. Zhou, Z. Zhou, S. Song et al., "Pt based anode catalysts for direct ethanol fuel cells," *Applied Catalysis B*, vol. 46, no. 2, pp. 273–285, 2003.
- [10] A. O. Neto, A. Y. Watanabe, M. Brandalise et al., "Preparation and characterization of Pt–Rare Earth/C electrocatalysts using an alcohol reduction process for methanol electro-oxidation," *Journal of Alloys and Compounds*, vol. 476, no. 1–2, pp. 288–291, 2009.
- [11] G. García, J. A. Silva-Chong, O. Guillén-Villafuerte, J. L. Rodríguez, E. R. González, and E. Pastor, "CO tolerant catalysts for PEM fuel cells. Spectroelectrochemical studies," *Catalysis Today*, vol. 116, no. 3, pp. 415–421, 2006.
- [12] S. Song and P. Tsiakaras, "Recent progress in direct ethanol proton exchange membrane fuel cells (DE-PEMFCs)," *Applied Catalysis B*, vol. 63, no. 3–4, pp. 187–193, 2006.
- [13] A. O. Neto, R. R. Dias, M. M. Tusi, M. Linardi, and E. V. Spinacé, "Electro-oxidation of methanol and ethanol using PtRu/C, PtSn/C and PtSnRu/C electrocatalysts prepared by an alcohol-reduction process," *Journal of Power Sources*, vol. 166, no. 1, pp. 87–91, 2007.
- [14] E. V. Spinacé, L. A. Farias, M. Linardi, and A. O. Neto, "Preparation of PtSn/C and PtSnNi/C electrocatalysts using the alcohol-reduction process," *Materials Letters*, vol. 62, no. 14, pp. 2103–2106, 2008.
- [15] E. Antolini, J. R. C. Salgado, L. G. R. A. Santos et al., "Carbon supported Pt–Cr alloys as oxygen-reduction catalysts for direct methanol fuel cells," *Journal of Applied Electrochemistry*, vol. 36, no. 3, pp. 355–362, 2006.
- [16] Y. Bai, J. Wu, X. Qiu et al., "Electrochemical characterization of Pt–CeO₂/C and Pt–Ce_xZr_{1–x}O₂/C catalysts for ethanol electro-oxidation," *Applied Catalysis B*, vol. 73, no. 1–2, pp. 144–149, 2007.
- [17] E. V. Spinacé, A. O. Neto, T. R. R. Vasconcelos, and M. Linardi, "Electro-oxidation of ethanol using PtRu/C electrocatalysts prepared by alcohol-reduction process," *Journal of Power Sources*, vol. 137, no. 1, pp. 17–23, 2004.
- [18] E. V. Spinacé, A. O. Neto, T. R. R. Vasconcelos, and M. Linardi, *Brazilian Patent INPI-RJ, PI0304121-2*, 2003.
- [19] F. Colmati, W. H. Lizcano-Valbuena, G. A. Câmara, E. A. Ticianelli, and E. R. Gonzalez, "Carbon monoxide oxidation on Pt–Ru electrocatalysts supported on high surface area carbon," *Journal of the Brazilian Chemical Society*, vol. 13, no. 4, pp. 474–482, 2002.
- [20] K. W. Lux and E. J. Cairns, "Lanthanide-platinum intermetallic compounds as anode electrocatalysts for direct ethanol PEM fuel cells," *Journal of the Electrochemical Society*, vol. 153, no. 6, pp. A1132–A1138, 2006.

- [21] T. A. B. Santoro, A. O. Neto, R. Chiba, E. S. M. Seo, and E. G. Franco, "Characterization of proton exchange membrane fuel cell cathode catalysts prepared by alcohol-reduction process," *Materials Science Forum*, vol. 660-661, pp. 94–99, 2010.
- [22] X. Wang, M. Wang, H. Song, and B. Ding, "A simple sol-gel technique for preparing lanthanum oxide nanopowders," *Materials Letters*, vol. 60, no. 17-18, pp. 2261–2265, 2006.
- [23] T. A. B. Santoro, C. A. L. G. de O. Forbicini, A. O. Neto et al., "Synthesis of PtLa/C catalysts for polymer electrolyte membrane fuel cells," in *Proceedings of the 1st Simposium Ibérico de Hidrógeno, Pilas de Combustible y Baterías Avanzadas (HYCEL-TEC '08)*, Bilbao, Spain, 2008.
- [24] C. Xu, R. Zeng, P. K. Shen, and Z. Wei, "Synergistic effect of CeO₂ modified Pt/C catalysts on the alcohols oxidation," *Electrochimica Acta*, vol. 51, no. 6, pp. 1031–1035, 2005.
- [25] L. M. Cornaglia, J. Múnera, S. Irusta, and E. A. Lombardo, "Raman studies of Rh and Pt on La₂O₃ catalysts used in a membrane reactor for hydrogen production," *Applied Catalysis A*, vol. 263, no. 1, pp. 91–101, 2004.
- [26] A. O. Neto, L. A. Farias, R. R. Dias, M. Brandalise, M. Linardi, and E. V. Spinacé, "Enhanced electro-oxidation of ethanol using PtSn/CeO₂-C electrocatalyst prepared by an alcohol-reduction process," *Electrochemistry Communications*, vol. 10, no. 9, pp. 1315–1317, 2008.
- [27] T. Iwasita, B. Rasch, E. Cattaneo, and W. Vielstich, "A sniftirs study of ethanol oxidation on platinum," *Electrochimica Acta*, vol. 34, no. 8, pp. 1073–1079, 1989.

Research Article

Influence of Synthesis pH on Textural Properties of Carbon Xerogels as Supports for Pt/CXs Catalysts for Direct Methanol Fuel Cells

C. Alegre, M. E. Gálvez, D. Sebastián, R. Moliner, and M. J. Lázaro

Instituto de Carboquímica (CSIC), Miguel Luesma Castán 4, 50018 Zaragoza, Spain

Correspondence should be addressed to M. J. Lázaro, mlazaro@icb.csic.es

Received 1 May 2011; Revised 4 September 2011; Accepted 19 September 2011

Academic Editor: Elena Pastor Tejera

Copyright © 2012 C. Alegre et al. This is an open access article distributed under the Creative Commons Attribution License, which permits unrestricted use, distribution, and reproduction in any medium, provided the original work is properly cited.

Carbon xerogels (CXs) have been prepared by polycondensation of resorcinol and formaldehyde. Two synthesis pHs were studied in order to evaluate its influence on the electrochemical behaviour of Pt catalysts supported on previous carbon xerogels, synthesized by conventional impregnation method. Catalysts were also synthesized over a commercial carbon black (Vulcan-XC-72R) for comparison purposes. Characterization techniques included nitrogen physisorption, scanning electron microscopy, and X-ray diffraction. Catalysts electrochemical activity towards the oxidation of carbon monoxide and methanol was studied by cyclic voltammetry and chronoamperometry to establish the effect of the carbon support on the catalysts performance. Commercial Pt/C catalyst (E-TEK) was analyzed for comparison purposes. It was observed that the more developed and mesopore-enriched porous structure of the carbon xerogel synthesized at a higher initial pH resulted in an optimal utilization of the active phase and in an enhanced and promising catalytic activity in the electrooxidation of methanol, in comparison with commercial catalysts.

1. Introduction

One of the main challenges nowadays in polymer-electrolyte fuel cell technology is the optimization of the catalytic systems employed in anode (fuel oxidation) and cathode (oxygen reduction), towards the enhancement of their catalytic activity and durability, at each time lower noble metal—normally Pt—loads. In the case of the anode of direct methanol fuel cells (DMFCs), the detailed mechanism of methanol oxidation has been elucidated during the last decades using a variety of experimental procedures, and several reviews can serve as a reference for the reader [1, 2]. Basically, the electrochemical oxidation of methanol on Pt involves several intermediate steps such as dehydrogenation, CO-like species chemisorption, OH (or H₂O) species adsorption, chemical interaction between adsorbed CO and OH compounds, and CO₂ evolution. The catalytic activity strongly depends on the metallic composition (it is well known that the presence of a second metal like Ru or Sn considerably enhances the OH adsorption and, consequently, the electrocatalytic activity), the particle size, the metallic surface structure, and the metal-support interaction [1–3].

Employing high-surface area carbon supports has been regarded as one of the most plausible options for achieving an optimal utilization of the active phase. Thus, in the last decade, an increasing number of publications report the synthesis and use of advanced carbon supports for fuel cell systems, such as carbon nanotubes [4, 5], carbon nanofibers [6, 7], ordered mesoporous carbons [8], and carbon xerogels and aerogels [4, 8–13], which can lead to more stable, highly active catalysts, at lower platinum loadings ($<0.1 \text{ mg} \cdot \text{cm}^{-2}$) than in the case of using conventional carbon black supports, leading therefore to lower catalyst cost [14]. In the preparation of carbon-supported catalysts, textural properties of the support can be properly adjusted in order to overcome mass transfer limitations while favouring an adequate dispersion of the active phase. This fact becomes especially significant in the case of the preparation of catalysts for electrochemical applications; their electrochemical properties may become strongly dependent on their final textural features, with adequate specific surface area and abundance of mesopores in the pore size range of 20–40 nm, resulting fundamental for a highly accessible catalytic surface area [15].

Since their introduction by Pekala in 1989 [16], resorcinol-formaldehyde aqueous gels have received considerable attention, due to the possibility of fine-tuning their textural properties by adequately modifying different parameters involved in their preparation [17]. In this way, it is possible to obtain a wide variety of materials with different properties which can be used in a wide range of applications [18]. Apart from this fact, these synthetic carbon materials possess high purity, and, moreover, whereas carbon blacks are constituted of aggregates connected through van der Waals bonds, carbon gels display monolithic structures at the micrometer scale, and, as a consequence, the pore texture of a carbon gel micromonolith remains identical in the catalytic layer of a membrane-electrode assembly [14, 19]. In previous studies [14, 19], PEMFCs cathodes were prepared from Pt catalyst supported on carbon aerogels and xerogels. The results obtained clearly evidenced that an adequate choice of the carbon pore texture can in fact lead to a significant decrease of the diffusion-induced potential losses. Liu and Creager [20] have recently reported as well evidence of lower mass transfer resistance in Pt-loaded carbon xerogels vis-à-vis the same electrocatalyst prepared using carbon black Vulcan XC-72 R as support.

Arbizzani et al. [15] studied the specific catalytic activity of DMFC anodes based on PtRu catalysts deposited by chemical and electrochemical route on mesoporous cryo- and xerogel carbons. Their results were compared with those obtained with PtRu supported on Vulcan, being the specific catalytic activity more than double when Vulcan is substituted by former carbons.

Job et al. [21] also synthesized highly mesoporous carbon via sol-gel condensation of resorcinol and formaldehyde. Electrooxidation of methanol in alkaline electrolyte was carried out using Pt and PtNi catalysts supported on highly mesoporous carbon xerogels. The electrocatalytic tests showed better performance of the catalysts when impregnated on this kind of carbon support.

In a more recent work [5], the same group prepared multiwalled carbon nanotubes and high surface area mesoporous carbon xerogel and used them as supports for monometallic Pt and bimetallic PtRu catalysts. In order to assess the influence of the oxygen surface groups of the support, the mesoporous carbon xerogel was also oxidized with diluted oxygen before impregnation. A remarkable increase in the activity was observed when the PtRu catalysts were supported on the oxidized xerogel. This effect was explained in terms of the metal oxidation state. It was shown that the oxidized support helps to maintain the metals in the metallic state, as required for the electrooxidation of methanol.

However, carbon gels have also been tested as carbon supports in several applications different from the field of electrocatalysis. For example, Job et al. [9] prepared Pt/C catalysts by impregnation of three xerogels possessing various pore textures. They observed that the specific catalytic activity measured towards benzene hydrogenation was 4–10 times higher in the presence of the carbon-xerogel-supported catalysts than the one determined for analogous active charcoal-supported ones. This enhanced catalytic activity was attributed to higher Pt dispersion on the carbon

surface, due to the abundant presence of large mesopores and wide mesopores in the carbon xerogel pore structure, which in the end facilitated its impregnation with the precursor of the active phase.

Carbon gels preparation comprises several steps, basically, (i) sol-gel synthesis and gel curing, (ii) drying, for removing the excess solvent, and (iii) carbonization of the organic gel. Carbon aerogels differ from carbon xerogels in the drying procedure applied in each case. While supercritical drying is used to synthesize carbon aerogels, carbon xerogels are prepared using conventional evaporative drying. This last option results in the shrinkage of the initial porous structure of the gel [22, 23], but its consequences can be really advantageous, depending on the final application of the carbon material. Furthermore, synthesis costs are also substantially reduced by means of choosing evaporative drying. Carbon xerogels possessing microporous, micro-mesoporous, to micro-macroporous structures can be produced by varying the morphologies of the primary particles that compose them, the degree of interconnectivity among primary particles, and by means of controlling gel structure shrinkage during drying, which is as well determined by the original structure of the organic gel. Resorcinol to formaldehyde molar ratio, kind and amount of catalyst used, solvent, dilution, and pH have a decisive influence in final gel properties. With respect to pH effect on the porosity of carbon gels, Mahata et al. [24] prepared carbon xerogels at two different pH values, 5.5 and 6, observing that the materials prepared at the lower pH values possessed considerably higher mesopore area but lower average pore diameter. Lin and Ritter [25] previously reported similar observations. They prepared carbon xerogels at pH values between 5.5 and 7.0, observing, that as the pH decreased from 7.0 to 6.5, the surface area increased sharply from 0 to $600 \text{ m}^2 \cdot \text{g}^{-1}$, then remained constant over the pH range from 6.5 to 5.5. In contrast, the pore volume increased almost linearly as the pH decreased between 7.0 and 5.7, and then remained constant at around $0.8 \text{ cm}^3 \cdot \text{g}^{-1}$ over the pH range from 5.7 to 5.5. These results indicate that the increase in the pore volume that occurred with a decrease in the pH from 6.5 to 5.5 corresponded to the creation of larger pores which did not contribute much to the surface area. They also observed that higher pH values led to carbon gels with a weaker pore structure which collapsed easily after drying and pyrolysis. They stated that higher pH hindered the condensation reaction leading to less cross-linking of the structures and resulting in a much weaker gel structure than at lower pH. A few years later, Zanto et al. [23] claimed the opposite, comparing carbon aerogels and xerogels synthesized at pH values of 5.5 and 7.0. The highest pH corresponded to the highest development of surface area and porosity. These authors explained this fact by stating, that at their higher pH setting, cross-linking of the already formed clusters occurred to a greater extent due to lower concentration of protons in the media, what resulted in a more porous polymeric structure. Zubizarreta et al. [26] noticed that the time required for gelation, curing, and drying of their organic gels depended on the pH of the initial solution. This parameter also influenced the structure of the materials

after drying, being less compact at the lowest pH values employed. In consequence, surface area and pore volume of the carbon gels decreased with increasing synthesis pH. Job and coworkers reported as well the strong influence that the pH of the solution in the synthesis of a carbon xerogel exerts on the final properties of these carbon materials [27]. As pH was increased from 5.45 to 7.35, carbon gels evolved from micro-macroporous to exclusively microporous materials, that is, pore size distribution becoming narrower at higher pHs, whereas surface area passed through a maximum at a pH of 6.50. However, these series of published works also evidence that there is no general agreement on the influence of this parameter in controlling the carbon gel final structure and that this might depend as well on the rest of the parameters involved in the gel synthesis and, in general, on the experimental procedure and setup used in each case.

In the present paper, mesoporous carbon xerogels have been synthesized at two pH values: 5.5 and 5.8, with the aim of evaluating its influence on the carbonaceous textural properties and, in turn, on the electrochemical behaviour of Pt-supported electrocatalysts. Although in recent years, PtRu, PtSn, and other Pt alloys have replaced Pt for the preparation of anodic catalysts, due to their enhanced performance and resistance towards CO poisoning [25–28], Pt was exclusively used as active metal through the present work in order to simplify the catalytic system. In this sense, this is a preliminary study focused on the evaluation of the particular influence of the carbon support in the catalyst activity, independently of the influence of other parameters such as Pt: M (Ru, Sn, etc.) atomic ratio, oxidation state, or the interaction between the bimetallic sites. Future works will comprise the introduction of bimetallic systems on the best support. Commercial Pt-supported catalyst (E-TEK) has also been studied for comparison. Moreover, in order to compare the results obtained using the synthesised carbon xerogels as supports, a catalyst was prepared using a commercial carbon black (Vulcan-XC-72 R) instead. Voltamperometric studies towards carbon monoxide and methanol oxidation were carried out in order to analyze the influence of the carbon support on the electrochemical behaviour of Pt catalysts [29].

2. Experimental

2.1. Synthesis of Carbon Xerogels. Resorcinol (1,3-dihydroxybenzoic acid)-formaldehyde organic gels were synthesized following the procedure described in detail in [27]. 9.91 g of resorcinol (99% Vol) were first mixed with 18.8 mL of deionised water under magnetic stirring and poured into sealable flasks. After dissolution, the pH value was generally close to 2 and was first increased close to the chosen value (5.5 and 5.8) by addition of concentrated sodium hydroxide solution (5 and 2 N solutions were used). Afterwards 13.5 mL of formaldehyde solution (Aldrich, 37% wt. in water, stabilized by 10–15% wt. methanol) were added to the mixture (resorcinol/formaldehyde ratio was 0.5), and the pH value was then finally adjusted by addition of diluted sodium hydroxide solution (0.5 N). The use of three different alkaline

solutions of various concentrations enabled us to minimize the amount of water added during pH adjustment.

Gelation was performed at 85°C in an oven. The obtained aqueous gels were then dried without any pretreatment, at 65°C for 5 h, and then, temperature was risen up to 110°C and held for another 5 h, as described elsewhere [25]. After drying, the gels were pyrolyzed at 800°C under nitrogen flow in a tubular oven, following the heating pattern described elsewhere [27]. Carbon xerogels obtained were named: CX_550, the one synthesized at pH = 5.5, and CX_580, in the case of adjusting to pH = 5.8 during its synthesis.

2.2. Pt Catalysts Synthesis. Pt was deposited on carbon xerogels by impregnation and reduction with sodium borohydride [2]. The amount of metallic precursors was adjusted in order to obtain a final nominal metal loading of 20% w/w. An aqueous solution of H₂PtCl₆ (Sigma-Aldrich) was slowly added into a dispersion of carbon xerogel or carbon black in ultrapure water under sonication. pH was adjusted to 5 with a 5 N NaOH solution. The loaded metal was reduced by addition of sodium borohydride, maintaining temperature around 18°C. Subsequently, catalysts were filtered and thoroughly washed with ultrapure water and dried overnight at 60°C.

2.3. Carbon Xerogels and Catalysts Textural and Morphological Characterization. The textural and morphological features of the synthesized carbon xerogels were determined by means of nitrogen physisorption at –196°C (Micromeritics ASAP 2020) and scanning electron microscopy (SEM, Hitachi S-3400 N). Textural properties such as specific surface area, pore volume, and pore size distribution were calculated from each corresponding nitrogen adsorption-desorption isotherms applying the Brunauer-Emmett-Teller (BET) equation, Barrett-Joyner-Halenda (BJH), and *t*-plot methods.

SEM combined with energy dispersive X-ray spectroscopy (SEM-EDX) was used to determine the amount of metal deposited. An analyzer EDX Röntec XFlash de Si(Li) was employed with this purpose. Catalysts were as well characterized by X-ray diffraction (XRD), using a Bruker AXS D8 Advance diffractometer, with a θ - θ configuration and using Cu-K α radiation.

2.4. Electrochemical Characterization. Electrochemical characterization has proven to be of key importance in determining the electrocatalytic activity of these materials [29, 30]. Catalysts electrochemical activity towards the oxidation of carbon monoxide and methanol was studied by cyclic voltammetry and chronoamperometry at room temperature as in previous works [6, 8, 31]. A cell with a three-electrode assembly at room temperature and an AUTOLAB potentiostat-galvanostat were used to carry out the electrochemical characterization. The counter electrode consisted on a pyrolytic graphite rod, while the reference electrode was a reversible hydrogen electrode (RHE). Therefore, all potentials in the text are referred to the latter. The working electrode consisted of a pyrolytic graphite disk (7 mm) with

a thin layer of the electrocatalyst under study deposited onto it. For the preparation of this layer, an aqueous suspension consisting of 2 mg of Pt/C catalyst was obtained by ultrasonically dispersing it in Nafion solution 10% wt. (15 μL) and ultrapure water (500 μL) (Millipore). Subsequently an aliquot of 40 μL of the dispersed suspension was deposited on top of the graphite disk (7 mm) and dried under inert atmosphere prior to its use.

After preparation, the electrode was immersed into de-aerated 0.5 M H_2SO_4 electrolyte, prepared from high purity reagents (Merck) and ultrapure water (Milli-Q). The electrolyte was saturated with pure N_2 or CO (99.997%, Air Liquide), depending on the experiments. Prior to the electrochemical characterization, the electrode was subjected to potential cycling between 0.05 and 1.10 V versus RHE at a scan rate of 500 $\text{mV}\cdot\text{s}^{-1}$ until a stable voltammogram in the base electrolyte (0.5 M H_2SO_4) was obtained. CO stripping voltammograms were obtained after bubbling this gas in the cell for 10 min at 0.20 V versus RHE, followed by nitrogen purging to remove the excess of CO. The admission potential was selected considering that, for this value, maximum adsorbate coverage is achieved for CO adsorption on Pt. Afterwards, potential cycling between 0.05 V and 1.10 V versus RHE at 20 $\text{mV}\cdot\text{s}^{-1}$ was carried out to follow CO oxidation. Electrochemical Pt active areas were determined from the integration of the current involved in the oxidation of a CO monolayer, taking into account that CO linearly adsorbs on Pt and assuming 420 $\mu\text{C}/\text{cm}^2$ involved in the oxidation process. Current values were normalized with respect to the electroactive area.

Cyclic voltammograms for the electrooxidation of methanol were carried out in a 2 M CH_3OH + 0.5 M H_2SO_4 solution, at scan rate of 20 $\text{mV}\cdot\text{s}^{-1}$, between 0.05 and 1.10 V versus RHE, and current was normalized with respect to each catalyst electroactive area.

Chronoamperometries were performed at 0.60 V versus RHE in a 2 M CH_3OH + 0.5 M H_2SO_4 solution, in order to evaluate the evolution of the electrocatalytic activity with time of the prepared catalysts in the electrooxidation of methanol. All the experiments were carried out at room temperature ($25 \pm 1^\circ\text{C}$), and current was normalized with respect to each catalyst electroactive area.

3. Results and Discussion

3.1. Influence of Synthesis pH in Carbon Xerogel Textural Features. Surface areas and pore volumes (total, mesopore and micropore) of the synthesized carbon xerogels and the commercial carbon black (Vulcan) determined from nitrogen physisorption isotherms are shown in Table 1. High values of surface area, 436 and 493 m^2/g , were measured for the carbon xerogels CX_550 and CX_580, respectively, considerably higher than the one obtained for Vulcan XC-72R, 223 m^2/g . Total pore volume in the case of the carbon xerogel synthesized at the highest pH, CX_580, 1.09 cm^3/g , is also noticeably higher than for the carbon black Vulcan and carbon xerogel CX_550, 0.47 cm^3/g . The pH of the initial solution clearly plays a definitive roll in the development

TABLE 1: Carbon supports (xerogels and carbon black) textural properties.

Sample	Surface area, S_{BET} (m^2g^{-1})	Total pore volume (cm^3g^{-1})	Mesopore volume $V_{\text{meso,BJH}}$ (cm^3g^{-1})	Micropore volume $V_{\text{micro,t-plot}}$ (cm^3g^{-1})
CX_550	436	0.47	0.25	0.21
CX_580	493	1.09	0.87	0.20
Vulcan	224	0.47	0.41	0.04

of porosity: a slight pH increase led to an almost two-fold higher pore volume and about 10% higher surface area. The main difference between CX_550 and CX_580 is the total pore volume which is more than double for the latter (1.09 cm^3/g for CX_580) than for the former (0.47 cm^3/g for CX_550). Mesopore volume values reflect that these are the pores which are preferentially formed when using a higher solution pH. In fact, a 3-fold increase in mesopore volume value can be observed when comparing CX_580 to CX_550, while it almost doubles the value determined for Vulcan carbon black. In the case of the synthesized carbon xerogels, micropore volume remains constant, independently of the synthesis pH, and, in any case, substantially higher than for Vulcan carbon black.

With respect to the morphology of carbon xerogels, SEM images (Figure 1) show that carbon xerogel synthesized at the lowest pH value of 5.5, CX_550, is formed by small polymer particles that are interconnected with large necks giving the gel a fibrous appearance. The appearance of the carbon xerogel synthesized at the highest pH, CX_580, differs slightly from the one observed for CX_550. At higher pH carbon gel structure looks less defined, more compact, and conformed by smaller polymeric particles pointing either to a higher degree of cross-linking, as suggested by Zanto et al. [23] or even due to a partial collapse of porosity during drying and pyrolysis, as stated by Lin and Ritter [25].

3.2. Pt/Carbon Xerogel Catalysts Physico-Chemical Characterization. Pt catalysts supported on the synthesized carbon xerogels were characterized by SEM-EDX and XRD. Their properties are summarized in Table 2. SEM-EDX analyses were carried out to determine the metal concentration in the electrocatalysts. Pt concentrations around 17-18% weight were obtained, close to 20% nominal loading. XRD patterns (Figure 2) show the typical reflectances of the face-centered cubic structure of platinum. Pt crystallite sizes obtained from the 220 peak in the XRD diffractograms (shown in Figure 2) using the Scherrer's equation are shown in Table 2.

Platinum supported on low pore volume carbon xerogel (Pt/CX_550) presents the highest crystal size of 6.2 nm, whereas using the carbon xerogel with the high pore volume (CX_580) leads to a considerable decrease in crystal size to 4.5 nm. This result highlights the importance of the support textural properties in the metallic crystal growth, where the impregnation of the carbon support can be impeded to a certain extent when there is a low presence of mesopores. Moreover, using Vulcan carbon black with a similar pore

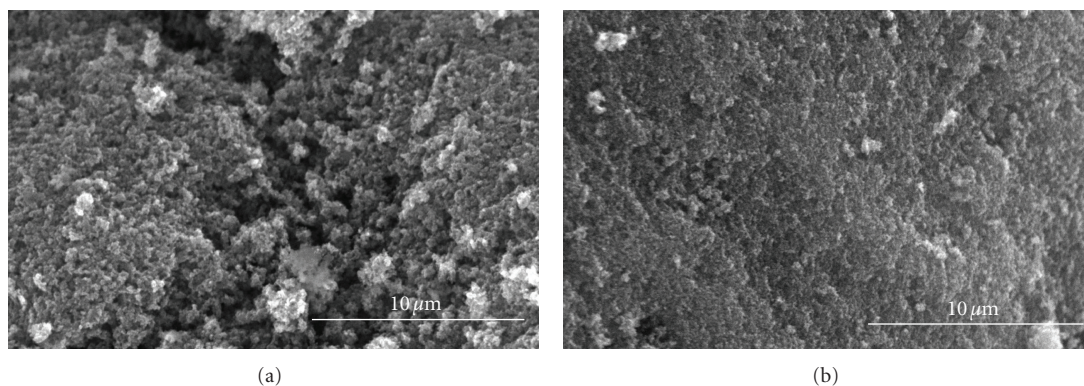


FIGURE 1: SEM micrographs of carbon xerogels: (a) CX_550; (b) CX_580.

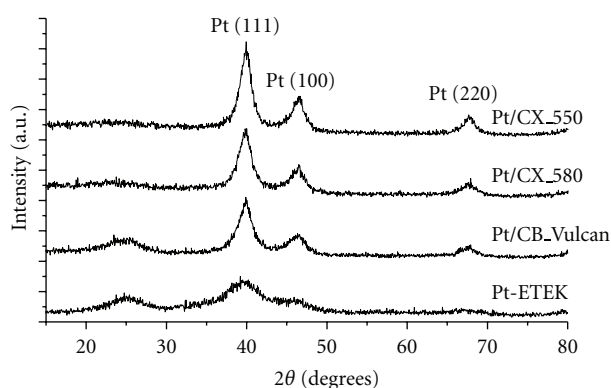


FIGURE 2: Diffractograms obtained by XRD for Pt catalysts assayed.

TABLE 2: Pt electrocatalysts properties.

Sample	% w/w Pt	Pt crystal size (nm)
Pt/CX_550	17	6.2
Pt/CX_580	18	4.5
Pt/CB_Vulcan	17	4.0
Pt-E-TEK	18	3.0

volume than CX_550 and half the surface area leads to a similar crystal size than the other CX_580, pointing out that not only textural properties are important but carbonaceous surface structure plays a role. On the other hand, the commercial catalyst (Pt-E-TEK) presents the lowest Pt crystal size of 3.0 nm. These differences in crystal domain size of the active phase will result in different electrocatalytic behaviour, which is the main purpose of the next section.

3.3. Electrochemical Characterization and Catalytic Activity.

Pt catalysts supported on carbon xerogels were characterized by cyclic voltammetry (CV). CO stripping was performed in order to establish the influence of the textural properties of the different supports in the electrochemical performance of each of the Pt catalysts towards CO electrooxidation. The electrooxidation of CO presents a strong dependence on the electrode surface state in terms of morphology and

structure [32–34]. CO stripping voltammograms obtained are shown in Figure 3. The second cycles recorded after CO-stripping, which correspond to the voltammograms in the base electrolyte for clean surfaces, are also shown.

The CO_{ad} oxidation peak for Pt/CX catalysts was obtained around 0.82 V versus RHE, as for Pt-E-TEK, as reported in the literature for commercial catalysts [34]. Whereas the maximum occurs at similar potential values, slight differences are observed as a contribution at more negative potentials (0.68–0.74 V versus RHE). The catalysts prepared by impregnation (Pt/CX_550, Pt/CX_580, and Pt/CB_Vulcan) present an onset potential at around 0.68 V versus RHE with a small shoulder not observed for Pt-E-TEK. This contribution to CO oxidation could be ascribed to the presence of certain surface arrangements in which CO is adsorbed with a slightly lower energy to platinum. Nevertheless, this contribution, although small compared to the peak observed at 0.82 V versus RHE, is independent of the crystal size (from 4.0 nm for CB_Vulcan up to 6.2 nm for CX_550), which is important to remark for the subsequent discussion about methanol oxidation. The charge observed at potential values higher than 0.9 V versus RHE could be attributed to the oxidation of the active phase or even the support to form oxygen functional groups [35], but, in any case, it represents a reversible process since the second cycle corresponds to the voltammogram in the base electrolyte, which means that a complete oxidation of the CO monolayer has been achieved in the first scan and the hydrogen adsorption-desorption region remains the same. Further spectroelectrochemical studies will be conducted and will serve to analyze these effects in deep.

To sum up, it can be concluded that, in this case, a different textural structure of the carbon xerogels does not seem to be a determinant factor for obtaining increased catalytic activity in the electrooxidation of CO.

The analysis of the CVs also shows some differences in the current densities observed in the double-layer region (0.4–0.6 V), between the catalysts supported on carbon xerogels (Pt/CX_550 and Pt/CX_580) and on carbon blacks (Pt-E-TEK and Pt/CB_Vulcan). At 0.4 V, the double-layer current density (obtained during the second voltammetric scan) is about 4 times higher for Pt/CXs. This fact implies

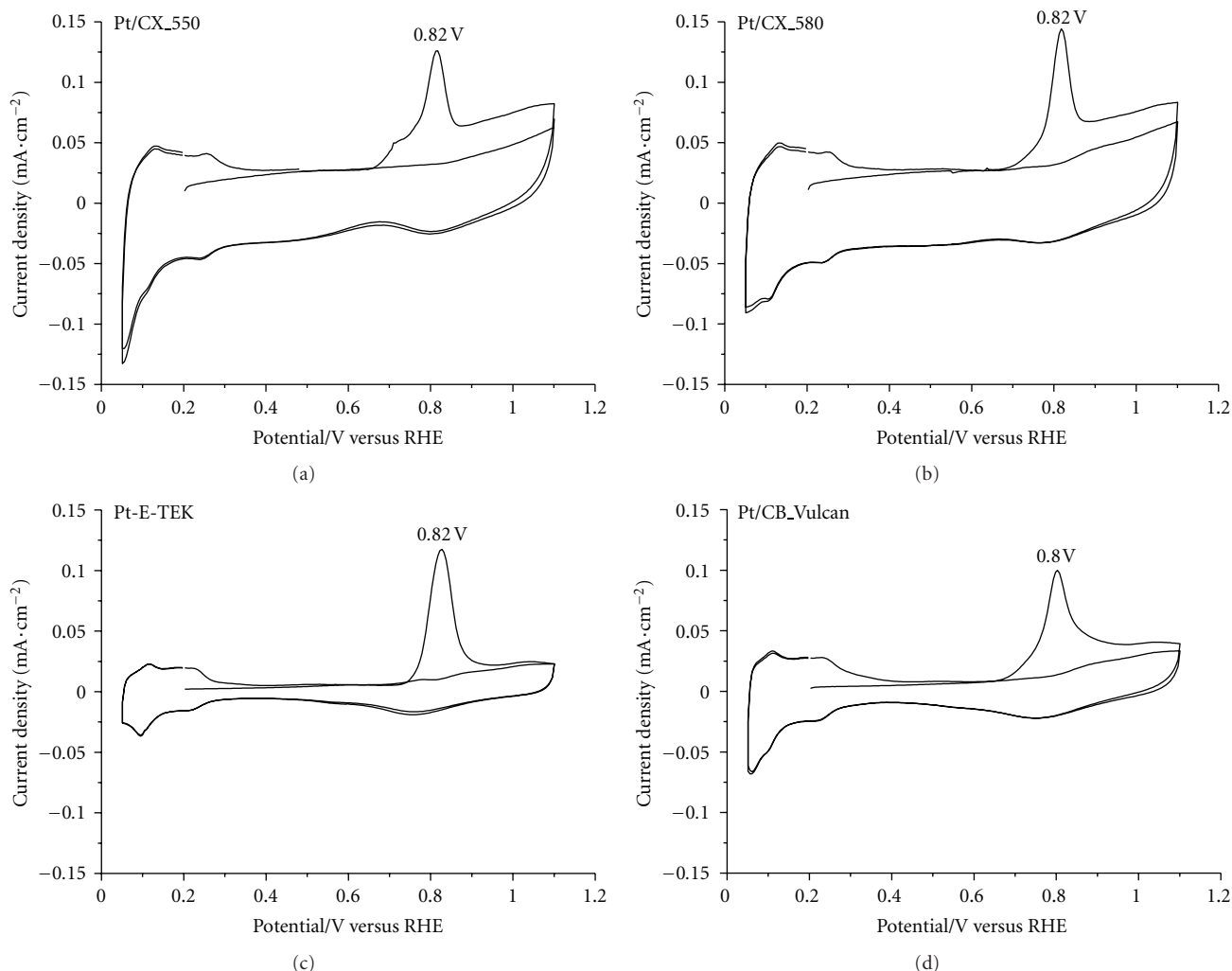


FIGURE 3: Cyclic voltammograms during CO stripping for Pt catalysts assayed in a 0.5 M H_2SO_4 solution. Scan rate $\nu = 0.02$ V/s.

that the capacitive behaviour is more apparent for the catalysts supported on the carbon xerogels than in the case of the one prepared using Vulcan XC-72 R or for Pt/E-TEK commercial catalysts, as previously reported in [31]. In this sense, the more developed textural properties (higher surface area) of the carbon xerogels employed as supports favours the capacitive behaviour of the catalysts.

The activity of the electrocatalysts towards the oxidation of methanol was studied by means of cyclic voltammetry, in a deaerated 2 M $\text{CH}_3\text{OH} + 0.5$ M H_2SO_4 solution at room temperature. Onset potentials and peak current densities measured obtained from the cyclic voltammograms (Figure 4) are shown in Table 3. Main differences can be observed at the sight of the current densities measured. While current densities are quite similar for catalysts prepared using CX_550, CX_580, and CB_Vulcan as supports, considerably lower current densities were determined for the commercial catalyst Pt/E-TEK.

The specific activity increases as a function of particle size [36]. Pt/CX_550 presents the higher particle size, but on the contrary does not present the higher specific activity.

On the other hand, Watanabe et al. found that the specific activity for methanol oxidation on a carbon-supported Pt electrocatalyst does not change for a particle size above 2 nm (Pt fcc structure); thus, the mass activity increases as the dispersion of the metal phase is increased [37]. In the case of our Pt/CXs catalysts, Pt catalyst prepared using the carbon xerogel synthesized at a higher pH shows a higher catalytic activity, which may be due to its better metal phase dispersion, when compared to the Pt catalyst prepared using the carbon xerogel synthesized at a lower pH, that presents a higher particle size.

When comparing Pt/CX_580 with Pt/CB_Vulcan, with similar Pt crystal sizes (4.5 versus 4.0), Pt/CX_580 shows a slightly higher specific activity. In this case, the nature of the support may have some kind of positive influence on this parameter, presumably in terms of diffusion, since the CO stripping studies do not show, as explained before, a preferential surface structure for platinum independent of the carbon support. Carbon xerogel possess a highly developed mesopore structure (high pore volume and average pore size), what favours the diffusion of reactants towards Pt

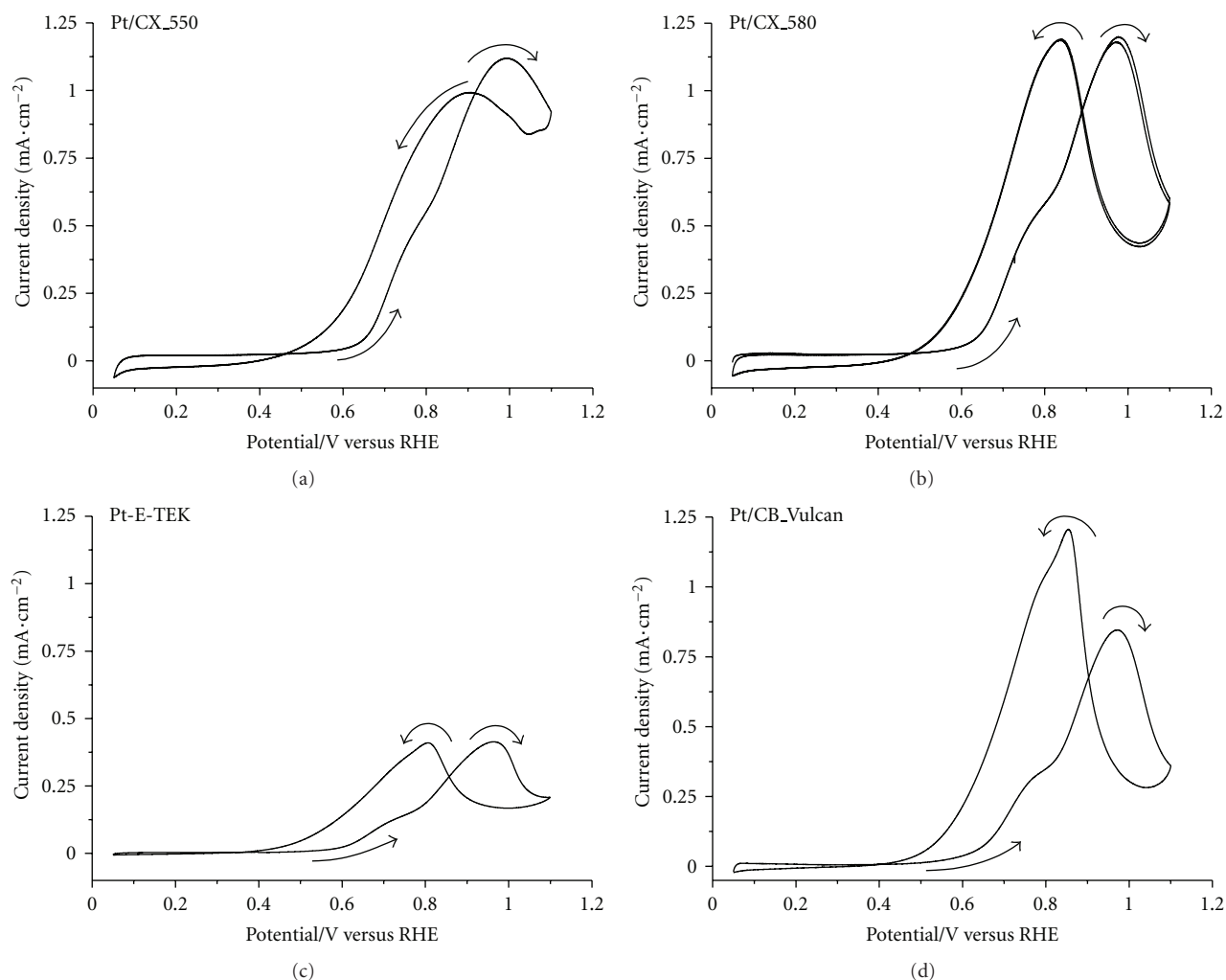


FIGURE 4: Cyclic voltammograms for the electrooxidation of methanol in a 2 M CH_3OH + 0.5 M H_2SO_4 solution at Pt catalysts and Pt-E-TEK. Scan rate $\nu = 0.02$ V/s.

TABLE 3: Onset and peak potentials extracted from methanol oxidation cyclic voltammograms measured for both the synthesised and commercial catalysts.

Catalyst	Onset potential/V versus RHE	Forward anodic peak/ mA cm^{-2}	Reverse anodic peak/ mA cm^{-2}
Pt/CX_550	0.53	1.13	1.00
Pt/CX_580	0.51	1.24	1.21
Pt/CB_Vulcan	0.49	0.86	1.23
Pt-E-TEK	0.48	0.43	0.42

particles. In fact, the most active catalyst towards methanol oxidation reaction is Pt/CX_580, which support presents the best textural features among the studied materials in this work.

Methanol electrooxidation chronoamperometric measurements presented in Figure 5 show that Pt/CX_580 reaches initially the highest current density, what it may be favoured

due to its enriched mesopore structure, favouring reactants diffusion. However, current density in the case of carbon xerogels supported catalysts decay uniformly with time, which is not the case of carbon-black-supported catalysts. This effect may be attributed to the accumulation of intermediate products that will be clarified with further spectroelectrochemical studies.

4. Conclusions

With the aim of analyzing the influence of the pH during carbon xerogel synthesis in their final textural properties and behaviour as supports in the preparation of Pt electrocatalysts, two different carbon xerogels were synthesized adjusting each corresponding initial solution to different pH values, namely, 5.5 and 5.8. The determination of their textural and morphological properties by means of nitrogen physisorption evidenced notably higher development of mesoporosity and more compact structure (studied by means of scanning electron microscopy) in the case of

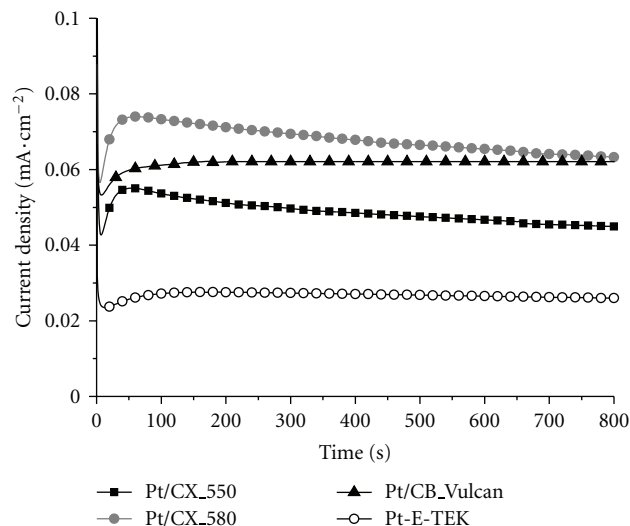


FIGURE 5: Current density-time curves recorded in a 2 M CH_3OH + 0.5 M H_2SO_4 solution at $E = 0.60$ V versus RHE for Pt-supported and Pt-E-TEK catalysts.

the carbon xerogel synthesized at the highest pH. Both materials show higher surface areas than those measured for Vulcan XC-72R; however, the carbon xerogel synthesized at the lower pH showed an important contribution of microporosity and lower amount of mesopores than this commercial carbon black. Pt catalysts were synthesized using the carbon xerogels prepared and Vulcan XC-72R as supports. XRD analysis showed smaller Pt crystallite size in the case of the carbon xerogel possessing a more developed porous structure, that is, the one synthesized at higher initial pH. More developed porosity, concretely abundance of mesopores, resulted in an optimized impregnation of the carbon surface, contributing to a more adequate active-phase dispersion.

Electrochemical characterization showed similar tolerance towards CO poisoning for the catalysts prepared using the synthesized carbon xerogels and the analogous catalysts prepared using Vulcan XC-72R as supports. Among carbon xerogels, slight differences were observed with small contributions to CO oxidation at more negative potentials.

Methanol electrooxidation studied by voltamperometric analyses showed that current densities obtained were considerably higher in the case of the carbon-xerogel-based catalysts and the Pt/CB_Vulcan catalyst, compared to the commercial Pt/E-TEK. Pt/CX_580 showed the highest specific activity which may be a combination of both adequate metal dispersion and a highly developed mesoporous structure, that may favour reactants diffusion towards reactive sites.

In fact, methanol chronoamperometry showed higher initial current density in this case, although electrocatalytic activity soon decreased with time reaching similar current density values than CB_Vulcan supported catalyst. At the beginning of the curves, the higher catalytic activity of the Pt/CX_580 catalyst may be due to diffusional effects that are favoured for Pt/CX catalyst (given its higher mesopore structure when compared to Vulcan).

Nevertheless, at the sight of the results obtained in this work, it can be concluded that the more developed and mesopore-enriched porous structure of the carbon xerogel synthesized at a higher initial pH resulted in a more optimal utilization of the active phase and in an enhanced and promising catalytic activity in the electrooxidation of methanol, in comparison to analogous catalysts prepared using Vulcan carbon black as support and to commercially available Pt catalysts.

Acknowledgments

The authors wish to thank “FEDER” and the Spanish MICINN for financial support MAT2008-06631-C03-01. M. E. Gálvez is indebted to the Spanish Ministry of Science and Innovation for its “Juan de la Cierva” postdoctoral grant.

References

- [1] S. Wasmus and A. Küver, “Methanol oxidation and direct methanol fuel cells: a selective review,” *Journal of Electroanalytical Chemistry*, vol. 461, no. 1-2, pp. 14–31, 1999.
- [2] J. R. C. Salgado, E. Antolini, and E. R. Gonzalez, “Structure and activity of carbon-supported Pt-Co electrocatalysts for oxygen reduction,” *Journal of Physical Chemistry B*, vol. 108, no. 46, pp. 17767–17774, 2004.
- [3] E. Teliz, V. Díaz, R. Faccio, A. W. Mombro, and F. Zinola, “The electrochemical development of Pt(111)stepped surfaces and its influence on methanol electrooxidation,” *International Journal of Electrochemistry*, vol. 2011, Article ID 289032, 9 pages, 2011.
- [4] Z. Cui, C. Liu, J. Liao, and W. Xing, “Highly active PtRu catalysts supported on carbon nanotubes prepared by modified impregnation method for methanol electro-oxidation,” *Electrochimica Acta*, vol. 53, no. 27, pp. 7807–7811, 2008.
- [5] J. L. Figueiredo, M. F. R. Pereira, P. Serp, P. Kalck, P. V. Samant, and J. B. Fernandes, “Development of carbon nanotube and carbon xerogel supported catalysts for the electro-oxidation of methanol in fuel cells,” *Carbon*, vol. 44, no. 12, pp. 2516–2522, 2006.
- [6] D. Sebastián, J. C. Calderón, J. A. González-Expósito et al., “Influence of carbon nanofiber properties as electrocatalyst support on the electrochemical performance for PEM fuel cells,” *International Journal of Hydrogen Energy*, vol. 35, no. 18, pp. 9934–9942, 2010.
- [7] L. Calvillo, M. Gangeri, S. Perathoner, G. Centi, R. Moliner, and M. J. Lázaro, “Effect of the support properties on the preparation and performance of platinum catalysts supported on carbon nanofibers,” *Journal of Power Sources*, vol. 192, no. 1, pp. 144–150, 2009.
- [8] L. Calvillo, M. J. Lázaro, E. García-Bordejé et al., “Platinum supported on functionalized ordered mesoporous carbon as electrocatalyst for direct methanol fuel cells,” *Journal of Power Sources*, vol. 169, no. 1, pp. 59–64, 2007.
- [9] N. Job, M. F. R. Pereira, S. Lambert et al., “Highly dispersed platinum catalysts prepared by impregnation of texture-tailored carbon xerogels,” *Journal of Catalysis*, vol. 240, no. 2, pp. 160–171, 2006.
- [10] P. V. Samant, J. B. Fernandes, C. M. Rangel, and J. L. Figueiredo, “Carbon xerogel supported Pt and Pt-Ni catalysts for electro-oxidation of methanol in basic medium,” *Catalysis Today*, vol. 102-103, pp. 173–176, 2005.

- [11] H. J. Kim, W. I. Kim, T. J. Park, H. S. Park, and D. J. Suh, "Highly dispersed platinum-carbon aerogel catalyst for polymer electrolyte membrane fuel cells," *Carbon*, vol. 46, no. 11, pp. 1393–1400, 2008.
- [12] J. Marie, S. Berthon-Fabry, P. Achard, M. Chatenet, A. Pradourat, and E. Chainet, "Highly dispersed platinum on carbon aerogels as supported catalysts for PEM fuel cell-electrodes: comparison of two different synthesis paths," *Journal of Non-Crystalline Solids*, vol. 350, pp. 88–96, 2004.
- [13] N. Job, J. Marie, S. Lambert, S. Berthon-Fabry, and P. Achard, "Carbon xerogels as catalyst supports for PEM fuel cell cathode," *Energy Conversion and Management*, vol. 49, no. 9, pp. 2461–2470, 2008.
- [14] X. Yu and S. Ye, "Recent advances in activity and durability enhancement of Pt/C catalytic cathode in PEMFC. Part I. Physico-chemical and electronic interaction between Pt and carbon support, and activity enhancement of Pt/C catalyst," *Journal of Power Sources*, vol. 172, no. 1, pp. 133–144, 2007.
- [15] C. Arbizzani, S. Beninati, E. Manferrari, F. Soavi, and M. Mastragostino, "Cryo- and xerogel carbon supported PtRu for DMFC anodes," *Journal of Power Sources*, vol. 172, no. 2, pp. 578–586, 2007.
- [16] R. W. Pekala, "Organic aerogels from the polycondensation of resorcinol with formaldehyde," *Journal of Materials Science*, vol. 24, no. 9, pp. 3221–3227, 1989.
- [17] H. T. Gomes, P. V. Samant, P. Serp, P. Kalck, J. L. Figueiredo, and J. L. Faria, "Carbon nanotubes and xerogels as supports of well-dispersed Pt catalysts for environmental applications," *Applied Catalysis B*, vol. 54, no. 3, pp. 175–182, 2004.
- [18] N. Job, A. Théry, R. Pirard et al., "Carbon aerogels, cryogels and xerogels: influence of the drying method on the textural properties of porous carbon materials," *Carbon*, vol. 43, no. 12, pp. 2481–2494, 2005.
- [19] M. Kim, J. N. Park, H. Kim, S. Song, and W. H. Lee, "The preparation of Pt/C catalysts using various carbon materials for the cathode of PEMFC," *Journal of Power Sources*, vol. 163, no. 1, pp. 93–97, 2006.
- [20] B. Liu and S. Creager, "Carbon xerogels as Pt catalyst supports for polymer electrolyte membrane fuel-cell applications," *Journal of Power Sources*, vol. 195, no. 7, pp. 1812–1820, 2010.
- [21] N. Job, M. F. R. Pereira, S. Lambert et al., "Highly dispersed platinum catalysts prepared by impregnation of texture-tailored carbon xerogels," *Journal of Catalysis*, vol. 240, no. 2, pp. 160–171, 2006.
- [22] S. A. Al-Muhtaseb and J. A. Ritter, "Preparation and properties of resorcinol-formaldehyde organic and carbon gels," *Advanced Materials*, vol. 15, no. 2, pp. 101–114, 2003.
- [23] E. J. Zanto, S. A. Al-Muhtaseb, and J. A. Ritter, "Sol-gel-derived carbon aerogels and xerogels: design of experiments approach to materials synthesis," *Industrial and Engineering Chemistry Research*, vol. 41, no. 13, pp. 3151–3162, 2002.
- [24] N. Mahata, M. F. R. Pereira, F. Suárez-García, A. Martínez-Alonso, J. M. D. Tascón, and J. L. Figueiredo, "Tuning of texture and surface chemistry of carbon xerogels," *Journal of Colloid and Interface Science*, vol. 324, no. 1–2, pp. 150–155, 2008.
- [25] C. Lin and J. A. Ritter, "Effect of synthesis PH on the structure of carbon xerogels," *Carbon*, vol. 35, no. 9, pp. 1271–1278, 1997.
- [26] L. Zubizarreta, A. Arenillas, A. Domínguez, J. A. Menéndez, and J. J. Pis, "Development of microporous carbon xerogels by controlling synthesis conditions," *Journal of Non-Crystalline Solids*, vol. 354, no. 10–11, pp. 817–825, 2008.
- [27] N. Job, R. Pirard, J. Marien, and J. P. Pirard, "Porous carbon xerogels with texture tailored by pH control during sol-gel process," *Carbon*, vol. 42, no. 3, pp. 619–628, 2004.
- [28] A. S. Arico, S. Srinivasan, and V. Antonucci, "DMFCs: from fundamental aspects to technology development," *Fuel Cells*, vol. 1, pp. 133–161, 2001.
- [29] S. Srinivasan, *Fuel Cells: From Fundamentals to Applications*, Springer, New York, NY, USA, 2006.
- [30] V. S. Bagotzky and Y. B. Vassilyev, "Mechanism of electrooxidation of methanol on the platinum electrode," *Electrochimica Acta*, vol. 12, no. 9, pp. 1323–1343, 1967.
- [31] C. Alegre, L. Calvillo, R. Moliner et al., "Pt and PtRu electrocatalysts supported on carbon xerogels for direct methanol fuel cells," *Journal of Power Sources*, vol. 196, no. 9, pp. 4226–4235, 2011.
- [32] B. Beden, C. Lamy, N. R. de Tacconi, and A. J. Arvia, "The electrooxidation of CO: a test reaction in electrocatalysis," *Electrochimica Acta*, vol. 35, no. 4, pp. 691–704, 1990.
- [33] J. M. Feliu, J. M. Orts, A. Fernandez-Vega, A. Aldaz, and J. Clavilier, "Electrochemical studies in sulphuric acid solutions of adsorbed CO on Pt (111) electrodes," *Journal of Electroanalytical Chemistry*, vol. 296, no. 1, pp. 191–201, 1990.
- [34] G. García, J. A. Silva-Chong, O. Guillén-Villafuerte, J. L. Rodríguez, E. R. González, and E. Pastor, "CO tolerant catalysts for PEM fuel cells. Spectroelectrochemical studies," *Catalysis Today*, vol. 116, no. 3, pp. 415–421, 2006.
- [35] J. S. Ye, X. Liu, H. F. Cui, W. D. Zhang, F. S. Sheu, and T. M. Lim, "Electrochemical oxidation of multi-walled carbon nanotubes and its application to electrochemical double layer capacitors," *Electrochemistry Communications*, vol. 7, no. 3, pp. 249–255, 2005.
- [36] J. A. Poirier and G. E. Stoner, "Microstructural effects on electrocatalytic oxygen reduction activity of nano-grained thin-film platinum in acid media," *Journal of the Electrochemical Society*, vol. 141, no. 2, pp. 425–430, 1994.
- [37] M. Watanabe, S. Saegusa, and P. Stonehart, "High platinum electrocatalyst utilizations for direct methanol oxidation," *Journal of Electroanalytical Chemistry*, vol. 271, no. 1–2, pp. 213–220, 1989.

Research Article

Carbon-Supported Fe Catalysts for CO₂ Electroreduction to High-Added Value Products: A DEMS Study: Effect of the Functionalization of the Support

S. Pérez-Rodríguez,¹ G. García,^{2,3} L. Calvillo,¹ V. Celorrio,¹ E. Pastor,² and M. J. Lázaro¹

¹ Instituto de Carboquímica CSIC, Miguel Luesma Castán 4, 50018 Zaragoza, Spain

² Departamento de Química-Física, Instituto Universitario de Materiales y Nanotecnología, Universidad de La Laguna, Avenida Astrofísico F. Sánchez s/n, 38071 La Laguna, Spain

³ Instituto de Catálisis y Petroleoquímica, CSIC, c/Marie Curie 2, 2. 28049 Madrid, Spain

Correspondence should be addressed to G. García, gonzalo@icp.csic.es and M. J. Lázaro, mlazaro@carbon.icb.csic.es

Received 30 April 2011; Accepted 9 September 2011

Academic Editor: Maria E. Martins

Copyright © 2011 S. Pérez-Rodríguez et al. This is an open access article distributed under the Creative Commons Attribution License, which permits unrestricted use, distribution, and reproduction in any medium, provided the original work is properly cited.

Vulcan XC-72R-supported Fe catalysts have been synthesised for the electroreduction of CO₂ to high-added value products. Catalysts were obtained by the polyol method, using ethylene glycol as solvent and reducing agent. Prior to the metal deposition, Vulcan was subjected to different oxidation treatments in order to modify its surface chemistry and study its influence on the physicochemical and electrochemical properties of the catalysts, as well as on the product distribution. The oxidation treatments of the supports modify their textural properties, but do not affect significantly the physicochemical properties of catalysts. However, DEMS studies showed that the carbon support degradation, the distribution of products, and the catalytic activity toward the CO₂ electroreduction reaction depend significantly on the surface chemistry of the carbon support.

1. Introduction

Carbon dioxide (CO₂) emissions are the inevitable result from the burning of fossil fuels for electricity and energy (80% anthropogenic CO₂) [1]. During the last years, CO₂ concentration in the atmosphere has been increasing, being the major responsible of global warming. Therefore, reducing the CO₂ concentration in the atmosphere has become a critical issue. Different methods have been developed to reduce its emissions, such as chemical, thermochemical, photochemical, electrochemical, and biochemical procedures [2–4]. Among them, the electrochemical reduction seems to be of particular interest since it could both mitigate the greenhouse gas emission and use CO₂ as carbon source for producing a variety of useful products like (e.g., formic acid, methanol, etc.) for energy source [1, 4–8]. CO₂ reduction would be carried out making use of renewable energy to result in a net decrease of CO₂ emissions [9, 10].

In recent years, different metallic electrodes have been studied for the electrochemical reduction of carbon dioxide,

since the product distribution strongly depends on the used material, surface metallic arrangement, and surface energy [11–17]. Copper has been found to be one of the most effective electrode materials for the CO₂ reduction process at atmospheric pressure and room temperature in aqueous solutions [11, 12, 16]. On the other hand, CO₂ is hardly reduced on group VIII-X metal electrodes such as Fe, Co, and Ni, under similar conditions [15–17].

One of the main problems of this process is the low solubility of CO₂ in water at atmospheric pressure and room temperature. For this reason, in the last years, the electroreduction of CO₂ has been studied at high pressure [18–21] or low temperatures [21–24] on different metal electrodes. It has been reported that, at low temperatures (ca. 2°C) or high pressures (ca. 30 atm), the catalytic activity of the electrodes toward the electrochemical CO₂ reduction increases and the selectivity of the resultant products can change, even for metal catalysts of the group VIII-X [18–24]. In this context, Azuma et al. reported that the CO₂

reduction efficiency increased dramatically on some metal electrodes, such as Ni, as the temperature decreased [24]. Conversely, at high pressure, formic acid and/or carbon monoxide are efficiently formed on metal electrodes of the group VIII-X. Moreover, the formation of short and long chain hydrocarbons such as methane, ethane, propane, and iso- and normal-butananes has also been observed on Fe, Co, and Ni electrodes [18–20].

Since the solubility of CO₂ in aprotic solvents is higher than in water, the electroreduction of CO₂ has also been studied using organic molecules (methanol, acetonitrile, dimethyl formamide, propylene carbonate, etc.) as reaction medium [25–32]. Higher CO₂ solubility increases the current density, however, the low electrolytic conductivity gives high ohmic losses. For this reason, methanol is often added into a supporting electrolyte in order to balance these two aspects. For example, Kaneco et al. reported that the faradic efficiencies for CO₂ reduction products using Cu electrode in a methanol solution at low temperatures were better than those obtained without methanol at ambient temperature [29, 30]. In addition, Ohta et al. reported the formation mainly of methane, carbon monoxide and ethane, on different metal electrodes (among them Fe, Co, and Ni) using methanol into the supporting electrolyte [27].

Therefore, the effective electrochemical reduction of CO₂ on metal surfaces of the group VIII-X using high pressures, low temperatures, and/or nonaqueous solvents has been demonstrated. Among these metals, Fe is well known as catalyst for the hydrocarbon formation in the Fischer-Tropsch reaction. Therefore, its catalytic activity toward the electrochemical CO₂ reduction is expected to be interesting [33].

On the other hand, carbon materials have also been used as electrodes for the electrochemical CO₂ reduction. However, until now, the electrocatalytic activity of these electrodes is not clear. Christensen et al. reported that CO₂ is reduced to CO and carbonate on a glassy carbon electrode in acetonitrile solution [32]. Moreover, Hara et al. reported the formation of hydrocarbons such as methane, ethane, ethylene, propane, and n-butane during the electrochemical CO₂ reduction on a glassy carbon electrode under 30 atm [34]. However, there are not many studies about the electroreduction of CO₂ on metal catalysts supported on carbon materials in aqueous electrolytes. These electrodes could have different properties than those of the corresponding metal or carbon material. The support could improve the dispersion of the metal and, therefore, the activity and/or selectivity could be changed. Nowadays, among all kinds of carbon supports, carbon blacks are the most commonly used, especially for electrochemical applications (e.g., in the fuel cells field), due to their mesoporous distribution and their graphite characteristics. Vulcan XC-72 is the most frequently used because of its good compromise between electrical conductivity and high specific surface area [35, 36]. The surface chemistry of carbon materials can be modified by oxidation treatments in gas or liquid phase in order to create functional groups. These functional groups may significantly affect the dispersion and anchoring of the metal on the carbon materials and, therefore, may affect the

TABLE 1: Nomenclature of functionalized Vulcan XC-72R.

Sample	Oxidizing agent	Temperature (°C)	Time (h)
Vulcan	—	—	—
Vulcan NSTa0.5	HNO ₃ -H ₂ SO ₄ 1 : 1 (v/v)	25	0.5
Vulcan NcTb0.5	Concentrated HNO ₃ (65%)	115	0.5
Vulcan NcTb2	Concentrated HNO ₃ (65%)	115	2

performance of the electrocatalysts. In addition, it is well known that surface oxygen groups are the responsible for both the acid-base and the redox properties of the carbon materials. It has been reported that the acidic groups on the carbon surface decrease the hydrophobicity of the carbon, whereas the less acidic groups improve the interaction between metal particles and carbon materials [37]. However, the functionalization of Vulcan XC-72R has not been studied for the CO₂ electroreduction reaction.

In this work, different Fe catalysts supported on Vulcan XC-72R have been prepared for studying the electroreduction of CO₂ in aqueous solution under 1 atm and room temperature. Prior to the metal deposition, Vulcan was subjected to different oxidation treatments, using HNO₃ or HNO₃-H₂SO₄ 1 : 1 (v/v) mixture as oxidizing agents, in order to create functional groups. In this way, the influence of the surface chemistry of the carbon support on the physicochemical and electrochemical properties of the catalysts for the CO₂ electroreduction process can be studied.

In the present communication, the modified and unmodified carbon supports were characterized by X-ray diffraction (XRD), scanning electron microscopy (SEM), temperature programmed desorption (TPD), and N₂-physisorption. On the other hand, carbon-supported catalysts (Fe/C) were characterized by energy dispersive X-ray analysis (EDX), XRD, SEM, and N₂-physisorption. In addition, the electrochemical properties of the catalysts and the formation of gaseous and volatile products of the reduction of CO₂ were followed by *in-situ* differential electrochemical mass spectrometry (DEMS).

2. Experimental

2.1. Functionalization of Vulcan XC-72R. In order to create functional groups, Vulcan XC-72R (Cabot) was modified with different oxidation treatments in liquid phase, using concentrated HNO₃ (65% wt.) (Nc) and an HNO₃-H₂SO₄ 1 : 1 (v/v) mixture (NS) as oxidizing agents [38]. The oxidation treatments were carried out at room (T_a) and boiling temperature (T_b) for 0.5 or 2 h. The nomenclature used for the different materials and the oxidation conditions are summarized in Table 1.

2.2. Synthesis of the Carbon-Supported Fe Electrocatalysts. Fe electrocatalysts were prepared by polyol method, using ethylene glycol (EG) as solvent and reducing agent. The

synthesis involved the following steps: first, the metal precursor, $\text{Cl}_3\text{Fe} \cdot 6\text{H}_2\text{O}$ (Sigma-Aldrich), was dissolved in ethylene glycol under sonication and the pH was adjusted to 11 using a 1 M NaOH/EG solution. Then, a known amount of Vulcan was added to the metal solution and the resultant suspension was heated at 195°C for 2 h under mechanical stirring. Subsequently, the mixture was quickly cooled in a cold-water bath and the pH was adjusted to 1 using HCl (37%, Sigma-Aldrich). Finally, catalysts were filtered, washed with water, and dried at 70°C . Appropriate amounts of metal precursors were used to obtain a theoretical metal loading of 20 wt.%.

2.3. Physicochemical Characterization. Metal content of the electrocatalysts was obtained using a Hitachi S-3400 N microscope coupled to a Röntec XFlash analyzer.

Temperature programmed desorption (TPD) experiments were carried out in a U-shaped quartz reactor using a Micromeritics Pulse Chemisorb 2700. The temperature was increased positively at a rate of $10^\circ\text{C min}^{-1}$ up to 1050°C under Ar flow. The amounts of CO and CO_2 desorbed from the carbon samples were analyzed online by mass spectroscopy using a ThermoStar GSD 301 T (Balzers).

Nitrogen adsorption and desorption isotherms were measured at -196°C using a Micromeritics ASAP 2020. The total surface area was determined using the (Brunauer, Emmett and Teller) BET equation and total pore volume was determined using the single point method at $P/P_0 = 0.99$. The micropore volume was determined using the t-plot method. Pore size distribution (PSD) curves were obtained from the analysis of the adsorption branch of the nitrogen isotherm using the (Barrett, Joyner and Halenda) BJH method. The maximum of the PSD was used as the average pore diameter.

X-Ray diffraction (XRD) patterns were recorded using a Bruker AXS B8 Advance diffractometer with a θ - θ configuration and using Cu $K\alpha$ radiation.

2.4. Preparation of Working Electrodes. The working electrodes (7 mm of diameter, 0.25 mm of thickness) were prepared depositing a layer of the catalysts ink onto one side of a carbon cloth previously treated at 320°C for 1 h. Catalyst inks were prepared by mixing 0.5 mg of catalyst, 0.01 g of Nafion dispersion (5 wt.%, Sigma-Aldrich), and $10 \mu\text{L}$ of ultrapure water. The final metal load of the working electrodes was 0.26 mg Fe/cm^2 .

2.5. DEMS Setup. A scheme of the DEMS setup used for the in situ spectrometric and electrochemical measurements is described in detail in [39]. Briefly, the working electrode (WE) is fixed between a PTFE membrane (Scimat) and a carbon glassy rod, which also keeps the electric contact. The cell was designed to follow “in-situ” the electrochemical properties of electrodes and, simultaneously, the gaseous species produced on the electroactive surface through mass spectrometry. Thus, the experimental setup allows the simultaneous acquisition of mass spectrometric cyclic voltammograms (MSCVs) for selected m/z (mass to charge) ratios and

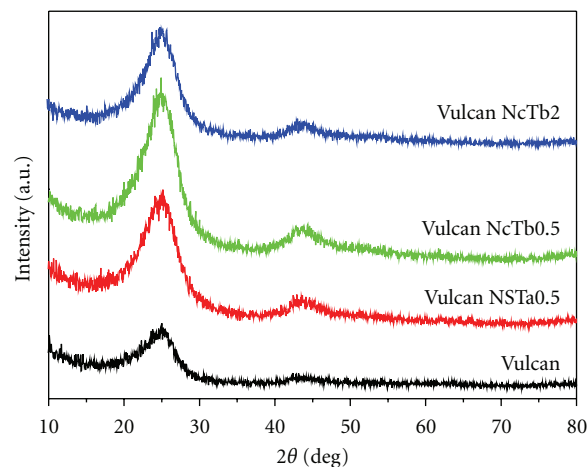


FIGURE 1: XRD patterns of carbon supports.

conventional voltammograms (CVs) or simultaneous mass spectrometric transients (MSTs) and conventional current transient curves.

2.6. Electrochemical Measurements. Electrochemical experiments were carried out in a three-electrode electrochemical cell at room temperature and atmospheric pressure. A large area carbon rod was used as a counter electrode, whereas an Ag/AgCl/Sat. KCl electrode placed inside a Luggin capillary was employed as reference. All potentials in the text are referred to this electrode. The potentiostat-galvanostat was an Autolab PGSTAT302 (Ecochemie). The electrochemical cell was directly attached to the vacuum chamber of a mass spectrometer (Balzers QMG112) with a Faraday cup detector.

The working electrode was immersed into 0.5 M H_2SO_4 (Merck, p.a.) electrolyte solution, which was deaerated with argon (N50). In order to analyze the activity of catalysts towards the reduction of CO_2 , previously to each measure, CO_2 (99,99%, Air Liquide) was bubbled during 30 min.

3. Results

3.1. Characterization of the Supports. SEM and XRD techniques were used to study the morphology of carbon support, before and after the oxidation treatments. SEM images (not shown) prove that Vulcan XC-72R is formed by an aggregation of spherical carbon nanoparticles (primary particles) with range sizes of 30–60 nm. After the oxidation treatments, the structure of Vulcan was not altered significantly. However, the most severe oxidation treatment (NcTb2) resulted in a partial destruction of its morphology, since primary particles did not show a spherical shape.

Figure 1 shows the XRD patterns of all the carbon supports. In all the samples, a peak around $2\theta = 25^\circ$ was observed, which is associated to the graphite (002) diffraction line. Also, (100) and (101) reflections of the graphite, at $2\theta = 24.8^\circ$ and $2\theta = 43.5^\circ$, can be observed. These peaks confirm that Vulcan has an intermediate structure between

TABLE 2: Quantification of surface oxygen groups as CO and CO₂ amounts desorbed during the TPD experiments.

Sample	CO ₂ and CO peak area (μmolg^{-1})					CO + CO ₂ (μmolg^{-1})	CO/CO ₂
	Carboxylic	Lactone	Anhydride	Phenol	Quinone + carbonyl		
Vulcan	—	—	—	—	—	—	—
Vulcan NSTa0.5	545	256	65	412	881	2160	1.54
Vulcan NcTb0.5	556	243	58	480	699	2037	1.42
Vulcan NcTb2	799	362	63	632	963	2819	1.34

TABLE 3: Textural properties of the supports and Fe electrocatalysts.

Sample	S_{BET} (m^2/g)	S_{MICRO} (m^2/g)	S_{MESO} (m^2/g)	V_{TOTAL} (cm^3/g)	V_{MICRO} (cm^3/g)	V_{MESO} (cm^3/g)
Vulcan	210	102	108	0.38	0.06	0.32
Vulcan NSTa0.5	200	104	96	0.40	0.06	0.34
Vulcan NcTb0.5	181	91	90	0.38	0.05	0.33
Vulcan NcTb2	159	77	82	0.38	0.04	0.33
Fe/Vulcan	175	76	99	0.41	0.04	0.36
Fe/Vulcan NSTa0.5	166	55	111	0.49	0.03	0.46
Fe/Vulcan NcTb0.5	148	58	90	0.41	0.03	0.37
Fe/Vulcan NcTb2	139	54	85	0.42	0.03	0.38

amorphous and graphitic. After the oxidation treatments, the same peaks were observed, indicating that the original structure of Vulcan was maintained. However, the intensity of the peaks increased with the severity of the oxidation treatment, except for the sample Vulcan NcTb2. This increase is attributed to the removal of the more amorphous carbon. In other words, the structure ratio crystalline/amorphous increases. On the other hand, the sample Vulcan NcTb2 did not follow the same tendency, which is attributed to the partial destruction of the original structure of Vulcan (i.e., both amorphous and crystalline structures are damaged), as observed by SEM.

The surface chemistry of the supports was studied by TPD experiments. These measurements give information about the surface oxygen groups created during the oxidation treatments. Acidic groups (carboxylic groups, lactones, and anhydrides) are decomposed into CO₂ at lower temperatures and basic and neutral groups (anhydrides, phenols, quinones and carbonyls) are decomposed into CO at higher temperatures during the TPD experiments [40]. In order to estimate the type and the amount of oxygen groups created during the oxidation treatments, CO₂ and CO profiles can be deconvoluted. Thus, the decomposition temperature can be related to the type of the functional groups created [40]. Deconvolution profiles were carried out with Excel software, using a Gaussian function to fit each functional group contribution and the corresponding addition of Gaussian curves was fitted minimizing the square of the deviations by a numerical routine (conjugate gradient method). Other authors have used this method [41].

As can be seen in Table 2, the original material had a negligible amount of surface oxygen groups. After the oxidation treatments, the number of surface oxygen groups increased, being the treatment with HNO₃ at boiling temperature during 2 h (NcTb2) the most effective at creating functional groups. In addition, it is observed that the ratio CO/CO₂, which can be taken as a measure of the surface acidity [42], decreased as the severity of the treatment increased.

Deconvolution of CO₂ profiles showed that carboxylic groups were mainly created. It is expected that these groups decrease the hydrophobic character of the carbon materials, improving their interaction with the metal. On the other hand, deconvolution of CO profiles showed that phenols, quinones, and carbonyls were mainly created. It is expected that these groups, which are stable at higher temperatures, act as metal anchoring sites, hindering the agglomeration of metal particles [42].

In order to further investigate how the pore structure and textural properties of the Vulcan XC-72R were changed during the oxidation treatments (see Section 2.1 for oxidation treatments details), supports were characterized by means of N₂-physisorption. Table 3 contains the textural properties of the carbon materials obtained by N₂-physisorption. Vulcan XC-72R has a high specific surface area (210 m² g⁻¹) and a large total pore volume (0.38 cm³ g⁻¹). Nevertheless, after the oxidation treatments, the specific surface area of all the samples decreased indicating a partial destruction of the original morphology, being this effect more significant at the carbon material oxidized with the most severe treatment (Vulcan NcTb2). However, no significant change

TABLE 4: Metal load of the carbon-supported Fe electrocatalysts.

Electrocatalysts	% metal (wt.)
Fe/Vulcan	16.7
Fe/Vulcan NSTa0.5	18.4
Fe/Vulcan NcTb0.5	18.9
Fe/Vulcan NcTb2	21.8

was observed in the pore volume. In fact, carbon supports are mainly mesoporous materials but also contain an appreciable amount of micropores, which is maintained after the surface oxidation. Results suggest that all carbon materials present a broad pore size distribution (PSD) in the range of mesoporosity.

3.2. Physicochemical Characterization of the Electrocatalysts.

The catalysts metal loading was determined by SEM-EDX. All catalysts present similar iron content to the nominal value of 20% (Table 4). However, a clear correlation between oxygen groups present in the surface and metal loading can be discerned. As the number of oxygenated groups increased, the amount of deposited Fe increased, since these oxygenated groups acted as anchoring sites. Additionally, homogeneous metal dispersion and deposition on all the carbon materials was observed by SEM images.

Fe/C catalysts were analyzed by XRD technique and their patterns are given in Figure 2. In all the electrocatalysts, except in the sample Fe/Vulcan NSTa0.5, six characteristic peaks appeared at $2\theta = 30.1, 35.5, 43.1, 57.0, 62.6$, which can be assigned to (2 2 0), (3 1 1), (4 0 0), (5 1 1), and (4 4 0) planes of Fe_3O_4 (magnetite) (JCPDS 88-0866), respectively. No diffraction peaks corresponding to iron metal or iron oxides species (FeO or Fe_2O_3) were observed. However, the intensity of the Fe_3O_4 diffraction peaks was not so relevant than that expected for 20 wt.% of iron load. This result suggests that another crystal phase with particle size inferior to 2 nm coexisted with Fe_3O_4 crystals and/or part of the metal was deposited on carbon materials forming a stable but not crystalline structure. In this context, it is important to mention that particle size smaller than 2 nm cannot be achieved by XRD analysis. Other authors have obtained similar results depositing Fe on carbon supports [43]. Additionally, it is noticeable that the diffraction peak at ca. $2\theta = 25^\circ$, which is associated to the graphite (002) diffraction line of the support, is still observed after the iron deposition.

Textural properties of catalysts obtained by N_2 -physorption are summarized in Table 3. Catalysts showed a lower surface area than the corresponding carbon supports, which is attributed to the metal particles loading on the pore surface. In particular, a reduction of the microporosity was observed after the catalysts loading, indicating that the metal was mainly distributed in the micropore structure of the support. PSD continued being broad in the mesoporosity range. However, the pore volume in the 20–50 nm pore diameter range is reduced, whereas in the 50–100 nm pore diameter range is increased. These results indicate that iron

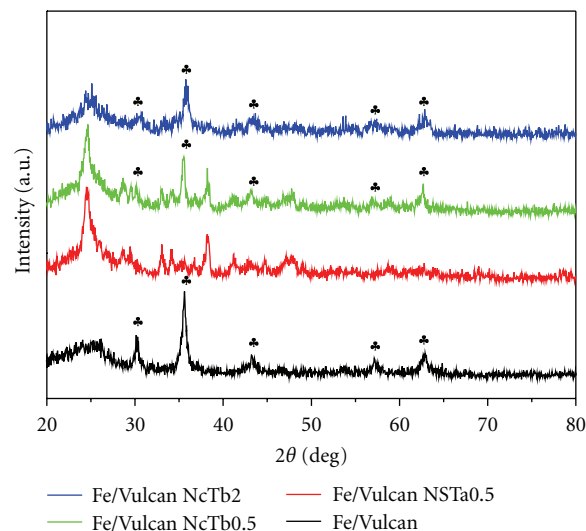


FIGURE 2: XRD patterns of 20% Fe/C catalysts.

was deposited on the micropores or mesopores with average pore diameter lower than 50 nm, in agreement with the N_2 -physorption results.

3.3. Electrochemical Performances of the Fe Electrocatalysts.

The electrochemical properties of the Fe catalysts were studied in 0.5 M H_2SO_4 , at room temperature and atmospheric pressure by DEMS. In this sense, DEMS studies provide more information than a simple electrochemical technique (i.e., cyclic voltammetry or chronoamperometry) such as the detection of volatile and gaseous products and intermediates generated in the electrochemical reactions with excellent sensibility. In this context, to the best of our knowledge, this is the first time that CO_2 reduction on carbon-supported Fe catalysts is analyzed by DEMS technique.

First, several potential cycles (not shown) between -0.2 and -1.8 V in 0.5 M H_2SO_4 , previously deaerated with Ar, were recorded to clean and activate the catalyst surface. In this context, the voltammetric profile remains similar during the activation step for all catalysts, indicating a minimal (or inexistent) alteration of the electroactive surface. After that, *in situ* spectroelectrochemical experiments were carried out in acid solution with and without dissolved CO_2 .

3.3.1. Cyclic Voltammetry (CV) and Mass Spectrometric Cyclic Voltammetry (MSCV).

Figure 3 shows the CVs and the corresponding MSCVs for all the carbon-supported Fe catalysts in free CO_2 sulphuric acid solution. The CVs for all the catalysts (Figure 3(a)) present a similar feature, that is, a very high cathodic current at potentials lower than -0.5 V, which may be related to the hydrogen evolution reaction. However, a close inspection of the same figure shows up that the onset potential for the cathodic current starts at different potentials for the different electrodes. The latter becomes clear from the MSCVs for $m/z = 2$ (Figure 3(c)), which is related to the molecular hydrogen formation. Therefore, it is possible to state that the previous carbon treatment

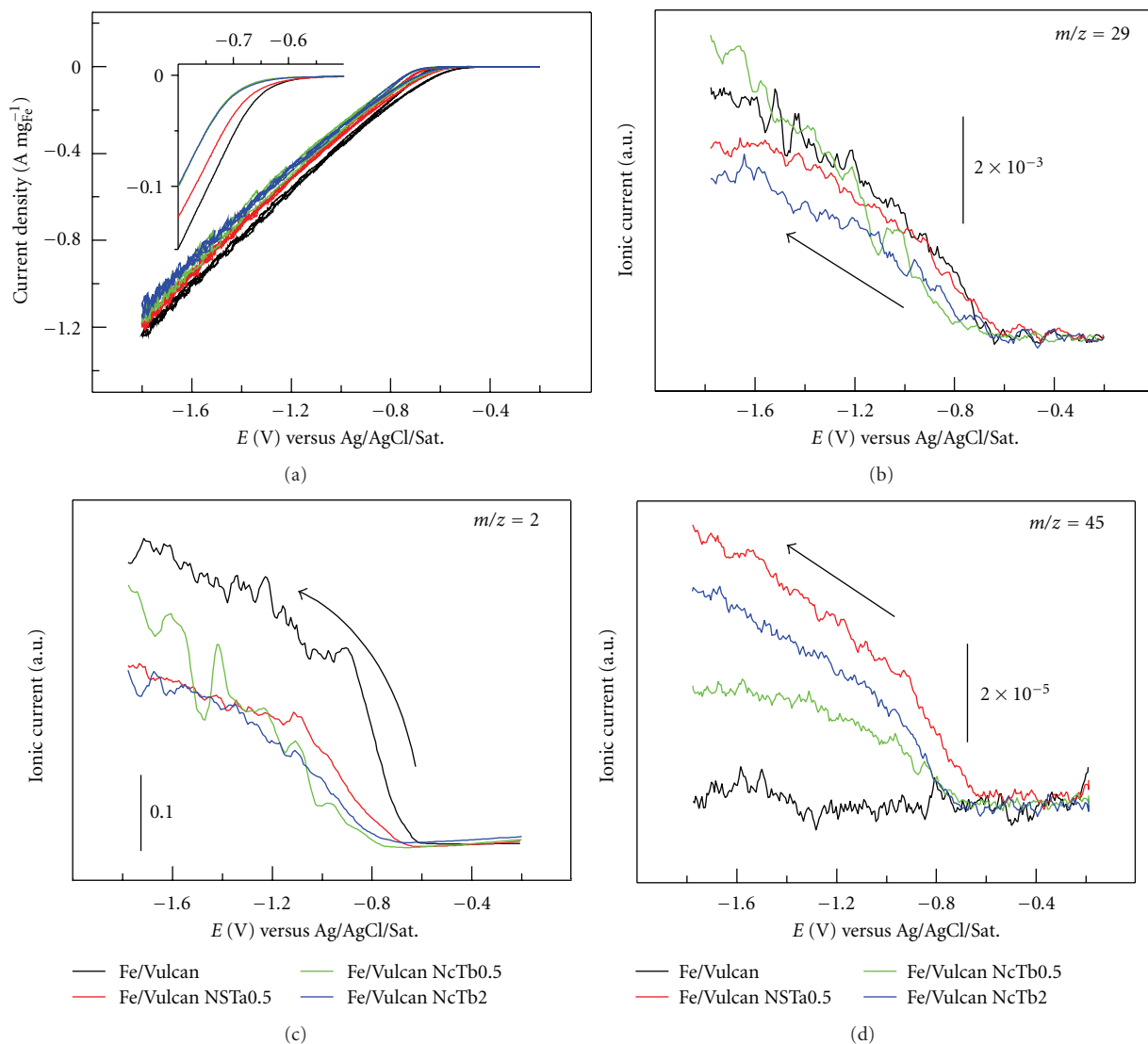


FIGURE 3: CVs and MSCVs for Fe/C catalysts in 0.5 M H₂SO₄ (sweep rate 10 mV s⁻¹, $E_i = -0.2$ V versus Ag/AgCl/Sat.). Inset shows a zoom of the onset potential region during the cathodic scan.

influences the water electro-reduction, and that the catalytic activity towards this reaction on the present Fe/C electrodes in a CO₂ free acid solution increases in the following way: Fe/Vulcan NcTb2 \approx Fe/Vulcan NcTb0.5 < Fe/Vulcan NSTa0.5 \ll Fe/Vulcan. Also, it is important to mention that the electrochemical behavior of all the electrodes remains similar after the electrochemical study without CO₂. The latter indicates that the electroactive surface is not damaged (or it is minimum) by these experiments.

Additionally to the H₂ formation, the mass signals $m/z = 16$ (CH₄⁺: methane), 30 (CH₃CH₃⁺ or H₂CO⁺: ethane or formaldehyde), 29 (CH₃CH₂⁺ or CHO⁺: ethane/ethanol or an aldehyde), and 45 (HCOO⁺ or CH₃CHOH⁺: formic acid or ethanol) were monitored during the cathodic scan. Figures 3(b) and 3(d) show the only two signals ($m/z = 29$ and 45) that increase during the excursion toward negative potentials. In this condition (no presence of dissolved CO₂),

the species associated to the mass signals 29 and 45 must be formed from the carbon support degradation. Interestingly, the mass signal 45 depends strongly on the carbon support treatment and its intensity rises in the order: Fe/Vulcan < Fe/Vulcan NcTb0.5 < Fe/Vulcan NcTb2 < Fe/Vulcan NSTa0.5. It is noticeable that the onset potential for the mass signal 45 formation at the catalyst previously treated with a mix of nitric and sulphuric acid is much lower than at the other catalysts (around 0.2 V), while the nontreated catalyst (Fe/Vulcan) presents a very small $m/z = 45$ signal at potentials more negative than -1.3 V. In the same way, both catalysts treated only with nitric acid develop the same onset potential for this m/z ratio, but its production on the Fe/Vulcan NcTb2 is somehow higher.

On the other hand, the ion current intensity and onset potential for the mass signal 29 are quite similar for all Fe/C catalysts. However, a close inspection of this figure shows

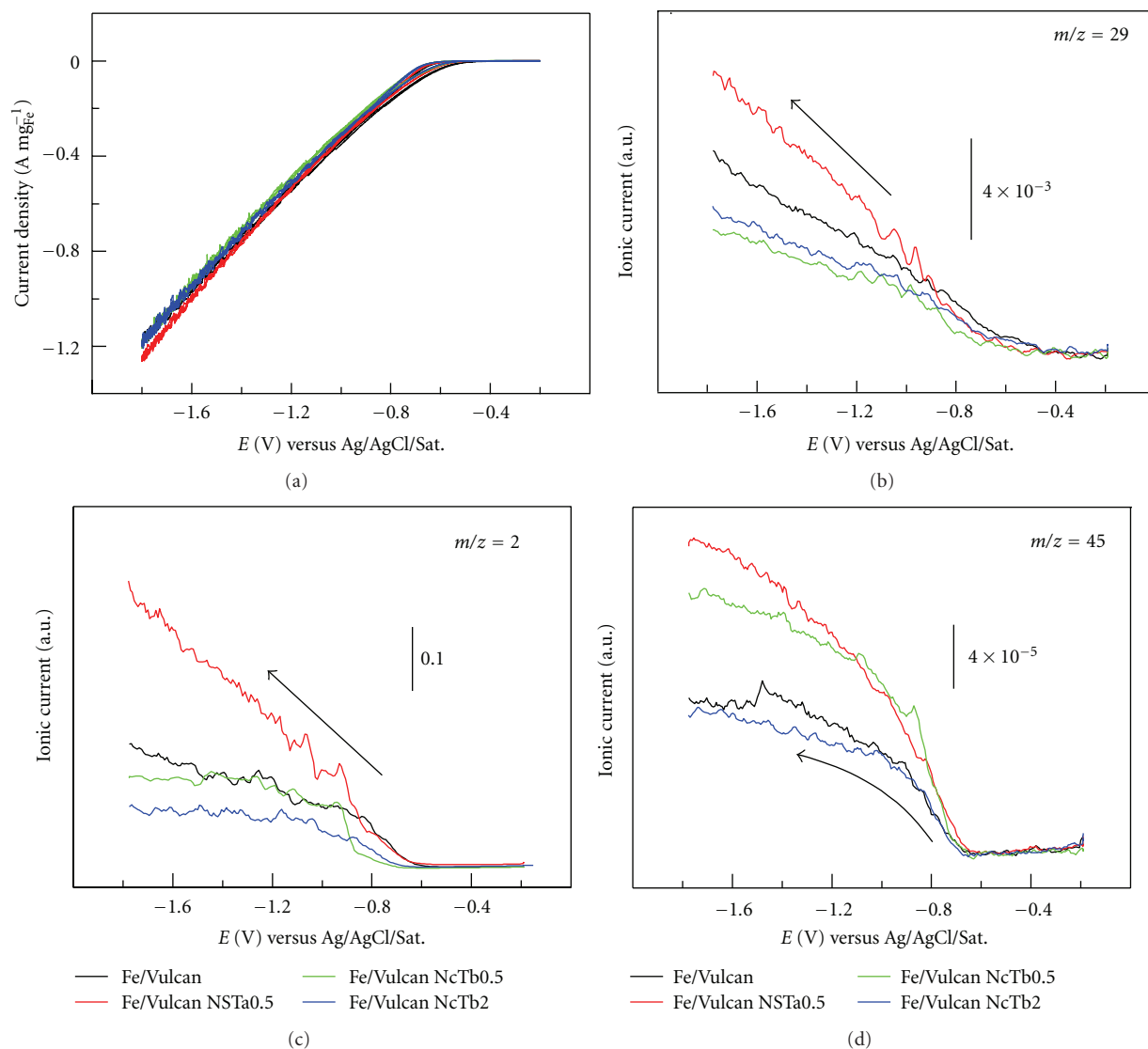


FIGURE 4: CVs and MSCVs for CO_2 -saturated solution in 0.5 M H_2SO_4 on Fe/C catalysts (sweep rate 10 mV s^{-1} , $E_i = -0.2 \text{ V}$ versus Ag/AgCl/Sat.).

a small but visible trend in its production, which diminishes in the subsequent way: Fe/Vulcan > Fe/Vulcan NSTa0.5 > Fe/Vulcan NcTb2. Fe/Vulcan NcTb0.5 catalyst presents a different behavior toward the mass signal 29 production, in which the onset potential is equal to Fe/Vulcan NcTb2 electrode and the ion current intensity increases linearly as the applied potential becomes more negative.

Summarizing, at the present conditions (CO_2 -free solution), nontreated catalyst (Fe/Vulcan) presents the highest and lowest catalytic activity towards hydrogen and mass signal 45 production, respectively. Treated catalysts develop similar behavior toward hydrogen evolution and the ionic current for the $m/z = 45$ depends strongly on the catalyst surface (see Table 2), that is, the mass signal 45 is enhanced on the catalysts that present oxygen groups on the surface. Additionally, mass signal 29 intensity modestly depends on the previous history of the carbon support.

Figure 4 displays the CVs and MSCVs ($m/z = 2, 29$, and 45) for all the Fe/C catalysts studied in the present work in acidic solution in the presence of dissolved carbon dioxide. Also, the $m/z = 16, 30$, and 32 were studied, but do not present an ionic current change during the cathodic scan. It is important to note that the intensity as well as the behavior of the mass signals 2, 29 and 45 are totally different to those observed in Figure 3 (in absence of dissolved CO_2). Interestingly, in presence of dissolved CO_2 , the hydrogen evolution (Figure 3(c)) decreases on Fe/Vulcan, Fe/Vulcan NcTb0.5 and Fe/Vulcan NcTb2, while it increases on Fe/Vulcan NSTa0.5. Moreover, the latter catalyst presents an onset potential shift to more positive potentials for hydrogen formation reaction, that is, water reduction is favored on Fe/Vulcan NSTa0.5 in CO_2 containing solution. Also, the the ratio $m/z = 29$ Figure 3(b) changes abruptly when CO_2 is present in the working solution. The ion

current intensity for this mass signal in a CO₂-containing solution is higher than in a CO₂-free one, and it drops off in the sequence: Fe/Vulcan NSTa0.5 > Fe/Vulcan > Fe/Vulcan NcTb2 ≈ Fe/Vulcan NcTa0.5, whereas the onset potential is quite similar for all the electrodes.

On the other hand, Figure 4(d) shows an important enhancement of the mass signal 45 at all the catalysts when CO₂ is present in the solution. These experimental facts unequivocally indicate that carbon dioxide is reduced to form hydrocarbonated compounds such as formic acid. The formation of acids, alcohols, or other molecules, which contain longer hydrocarbon chains, is not discarded but this characterization is not the principal purpose of the present work: the main reasons of the present study are to know if it is possible to electrochemically reduce CO₂ on iron catalysts and to establish if the carbon support influences on this particular reaction. Therefore, only the mass signals 2 and 45 are going to be followed along the present manuscript.

3.3.2. Current Transient (CT) and Mass Spectrometric Transient (MST). Potentiostatic pulse experiments were performed from a potential where nonfaradaic reactions occur ($E_i = -0.2\text{ V}$) to a final potential ($E_f = -1.8\text{ V}$) where the CO₂ reduction reaction is controlled by mass diffusion. Current transients for all the Fe/C catalysts used in the present work in absence (a) and presence (b) of dissolved CO₂ in sulphuric acid solution can be seen in Figure 5. It is observed similar faradaic current intensities than those obtained during the potentiodynamic experiments (Figures 3(a) and 4(a)), that is, Fe/Vulcan NcTb2 presents at both mediums (in presence and absence of dissolved CO₂) the lowest faradaic current, while the other catalysts develop similar faradaic currents. Consistent with the results presented above, molecular hydrogen production is significantly influenced by the presence of CO₂ (Figure 6). Fe/Vulcan and Fe/Vulcan NSTa0.5 electrodes present the highest catalytic activity toward H₂ formation in absence and presence of CO₂, respectively. Also, it is noticeable that the signal for $m/z = 2$ decreases abruptly on Fe/Vulcan, Fe/Vulcan NcTb0.5, and Fe/Vulcan NcTb2 catalysts, while the same reaction is enhanced on the Fe/Vulcan NSTa0.5 when CO₂ is present in solution.

Figure 7(a) shows the MSTs for the mass signal 45. Currents obtained are of the same order of magnitude than in the voltammetric experiments. However, a close inspection of the curves reveals that the $m/z = 45$ signal continuously increases on Fe/Vulcan catalyst along the time, while the other catalysts present a constant ionic current. The latter suggests that the support time degradation is more important at this material. In this sense, it is important to remind that Fe/Vulcan electrode presents small quantity of oxygenated species on the surface (see Table 2), that is, this catalyst suffers a dreadful condition at this potential. On the other hand, when CO₂ is present in solution (Figure 7(b)) the intensity of the mass signal 45 changes dramatically (about five fold times), as it was observed before the MSCV experiments (Section 3.3.1). In fact, the ionic current intensities for the mass signal 45 grow up on the studied

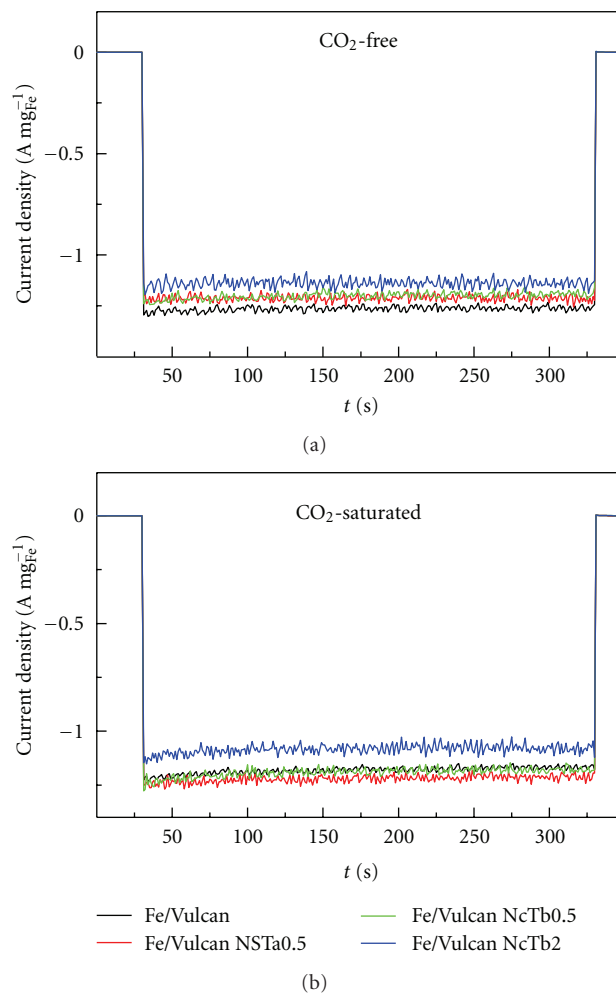
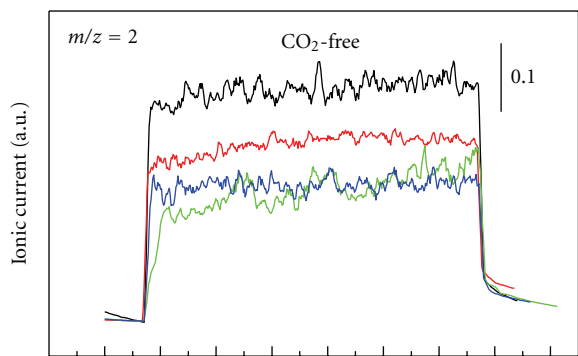


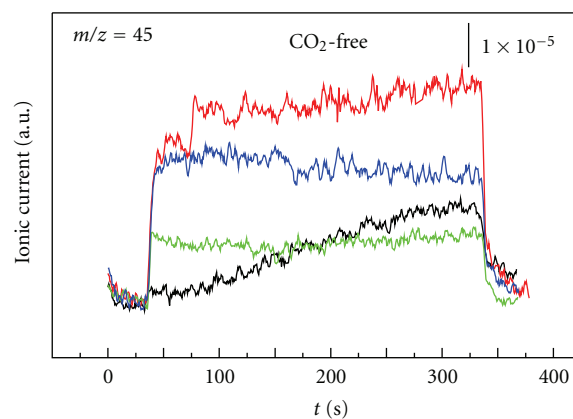
FIGURE 5: CTs for CO₂-free (a) and CO₂-saturated (b) solution in 0.5 M H₂SO₄ on Fe/C catalysts ($E_i = -0.2\text{ V}$, $E_f = -1.8$ versus Ag/AgCl/Sat.).

catalysts in the following way: Fe/Vulcan NcTb2 < Fe/Vulcan < Fe/Vulcan NcTb0.5 < Fe/Vulcan NSTa0.5.

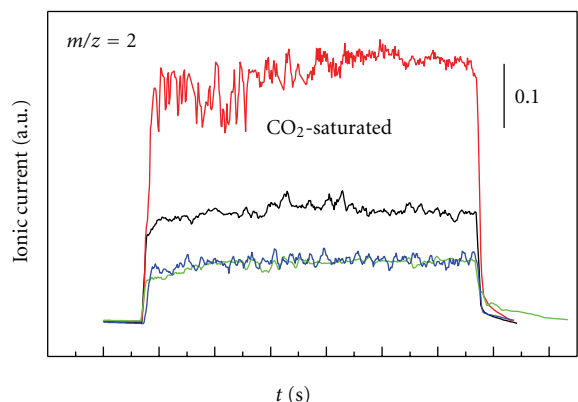
In order to acquire a realistic result of hydrocarbon production from carbon dioxide reduction, the mass signal 45 was subtracted from the ionic current signals obtained with dissolved CO₂ in solution (Figure 7(b)) and those acquired in a CO₂-free solution (Figure 7(a)) and represented in Figure 8. In this context, it is really important to know that this subtraction can be only done if all the parameters concerning to the mass spectrometer are constant [44], and because of this, our mass spectrometer setup was build up to make all this parameters accurate [39]. Therefore, Figure 8 shows a realistic catalytic activity toward carbon dioxide reduction. In fact, it can be observed that the typical features of a reaction controlled by mass diffusion, and even more important that the carbon dioxide reduction, or what is the same in this event, the hydrocarbon production depends strongly on the catalyst support and it increases as follows: Fe/Vulcan NcTb2 < Fe/Vulcan < Fe/Vulcan NSTa0.5 ≈ Fe/Vulcan NcTb0.5.



(a)

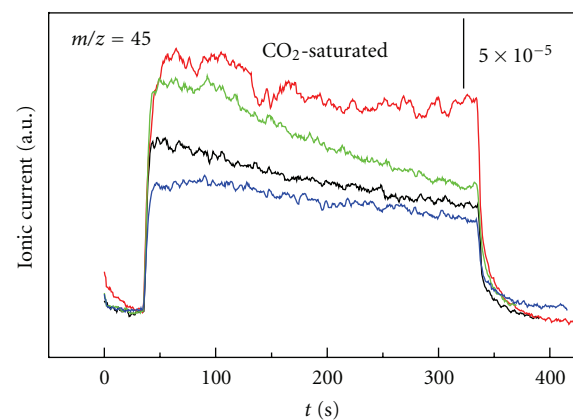


(a)



(b)

— Fe/Vulcan
— Fe/Vulcan NSTa0.5
— Fe/Vulcan NcTb0.5
— Fe/Vulcan NcTb2



(b)

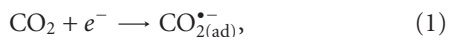
— Fe/Vulcan
— Fe/Vulcan NSTa0.5
— Fe/Vulcan NcTb0.5
— Fe/Vulcan NcTb2

FIGURE 6: MSTs for CO_2 -free (a) and CO_2 -saturated (b) solution in $0.5\text{ M H}_2\text{SO}_4$ on Fe/C catalysts ($E_i = -0.2\text{ V}$, $E_f = -1.8$ versus Ag/AgCl/Sat.).

FIGURE 7: MSTs for CO_2 -free (a) and CO_2 saturated (b) solution in $0.5\text{ M H}_2\text{SO}_4$ on Fe/C catalysts ($E_i = -0.2\text{ V}$, $E_f = -1.8$ versus Ag/AgCl/Sat.).

4. Discussion

Although the electrochemical reduction of carbon dioxide has been hugely studied, the reaction mechanism is not exactly known. Most of the reactions on different metal catalysts at diverse conditions, involving homogeneous and heterogeneous catalysis, were proposed by Sullivan [8] and assume a high availability of protons. In general, four principal pathways can be considered during the carbon dioxide reduction in acidic media [44]: (i) CO(g) formation via disproportionation; (ii) $\text{CO}_2^{\bullet-}$ radical formation; (iii) $\bullet\text{COOH}_{(\text{ad})}$ formation; (iv) the formation of adsorbed reduced- CO_2 species giving a range of reduced- CO_2 and products (CO , hydrocarbons and alcohols). The main proposed reactions in the CO_2 reduction mechanism are given as follows:



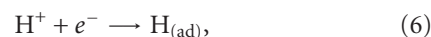
From $\text{CO}_{(\text{ad})}$ species, a series of products CH_2CO , CH_3CHO , $\text{C}_2\text{H}_5\text{OH}$, C_2H_4 , C_2H_6 , $\text{C}_3\text{H}_7\text{OH}$, and CH_3OH can be formed [44]. On the other hand, $\bullet\text{COOH}_{(\text{ad})}$ species can suffer a nucleophilic attack to form $\text{CO}_{(\text{ad})}$ or alternatively may be released as formic acid:



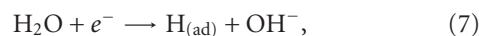
or via hydrated form:



Considering the same equations, a mechanism that represents our present study can be proposed. The following mechanism is quite similar to that described by Dubé and Brisard [45] for CO_2 electroreduction on polycrystalline Cu electrodes in acidic media. First, adsorbed hydrogen is formed during the cathodic sweep by the reaction



or by water dissociation:



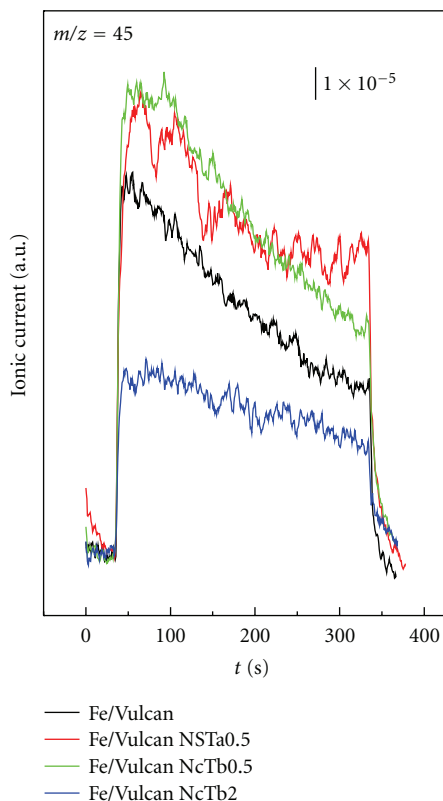
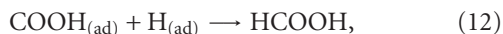


FIGURE 8: Corrected MSTs for CO_2 electroreduction in 0.5 M H_2SO_4 on Fe/C catalysts ($E_i = -0.2$ V, $E_f = -1.8$ versus Ag/AgCl/Sat.).

followed by hydrogen evolution:



Then, carbon dioxide bubbled through the solution may adsorb and react on the iron-based catalysts in acidic solution in the subsequent way:



The present mechanism is limited by the hydrogen (6) and carbon dioxide (9) adsorption reactions, which are necessary steps to form hydrogenated molecules. In fact, the availability of protons and the adsorbed hydrogen coverage on the surface have a strong influence on these reactions. Moreover, the metal surface must interact preferentially with a CO_2 species than with adsorbed hydrogen, otherwise,

hydrogen evolution reaction will be predominant at the electrode and carbon dioxide reduction reaction will be hindered.

Accordingly, two main pathways are possible.

(i) $\text{CO}_{(\text{ad})}$ formation (reaction (10)): the production of this species is favored when the metal surface is highly covered by adsorbed hydrogen and prefer to react with adsorbed carbon dioxide instead of reacting with each other. Therefore, the hydrogen evolution reaction will be apparently inhibited in this event. It seems that this path is governing on Fe/Vulcan NcTb2, Fe/Vulcan, Fe/Vulcan NcTb0.5 catalysts. In fact, it is clearly observed in the MSCVs and MSTs for $m/z = 2$ of all catalysts (with the exception of Fe/Vulcan NSTa0.5) in absence and presence of dissolved CO_2 (Figures 3, 4, and 6), in which the mass current signal associated to H_2 production decreases in presence of dissolved carbon dioxide. So, these iron catalysts have a preference to adsorb CO_2 instead of producing molecular hydrogen, and consequently, adsorbed hydrogen reacts with adsorbed carbon dioxide to produce hydrogenated species mainly through reaction (10). As it was described before, from adsorbed carbon monoxide it is possible to form products such as HCOH , CH_2CO , CH_3CHO , $\text{C}_2\text{H}_5\text{OH}$, C_2H_4 , C_2H_6 , $\text{C}_3\text{H}_7\text{OH}$ and CH_3OH [45, 46].

(ii) $\text{COOH}_{(\text{ad})}$ production (reaction (11)): this pathway gives mainly formic acid as a final product (reaction (12)). Reaction (11) is favoured on surfaces with preference to produce molecular hydrogen, and therefore, with a low H_2 coverage. In other words, adsorbed hydrogen species prefer to react with each other to form molecular hydrogen instead of reacting with adsorbed carbon dioxide. Therefore, hydrogen evolution reaction is usually favoured in parallel to this reaction. Nevertheless, adsorbed carbon monoxide formation (reaction (13)) cannot be discarded. Thus, if $\text{CO}_{(\text{ad})}$ is produced, the operative mechanism will be the same than that described above (reaction path i). In this context, Fe/Vulcan NSTa0.5 catalyst is the only one that does not follow the behavior observed for the other catalysts. In fact, this catalyst enhances the hydrogen evolution ($m/z = 2$) and mass signal 45 in presence of CO_2 . The latter suggests that Fe/Vulcan NSTa0.5 catalyst follows principally the reaction path (ii).

Furthermore, the native oxygenated species on the carbon support may follow the same reactions during the cathodic scan (at least in absence of dissolved CO_2 , see Figures 3 and 7(a)).

In this context, the mass signal 29 can be attributed to the first reaction path (i), while $m/z = 45$ can be associated with formic acid production (ii). Nevertheless, the last mass signal also could be linked to the reaction path (i), that is, it could be related to a fragmentation of a long hydrogenated species such as ethanol, which presents

27, 29, 31, and 45 ion current signals. In this sense, in a forthcoming work, will be discussed in detail the species produced during the carbon dioxide reduction on iron catalysts.

Additionally, it is observed that all the present surface reactions are strongly affected by the carbon support. This statement is observed in the MSCVs for $m/z = 2, 29,$ and 45 in Figures 3 and 4, and strongly confirmed by the MSTs for molecular hydrogen and formic acid production depicted in Figures 6 and 7, respectively. It seems that surface oxygen groups enhance the catalytic activity toward CO_2 reduction. However, Fe/Vulcan NcTb2 presents the lowest ion current intensities, suggesting that longer treatment times of carbon support in nitric acid destroy (at least partially) the support structure, and consequently, the catalytic activity towards CO_2 diminishes.

On the other hand, the surface chemistry of the carbon support could explain the different catalytic activity toward CO_2 reduction recorded on Fe/Vulcan NSTa0.5. Vulcan NSTa0.5 is the only support that suffered the oxidation treatment at ambient temperature in the presence of nitric and sulphuric acid. A temperature effect must be discarded since the material catalyst supported on untreated Vulcan follows the same behavior than the other catalysts. Therefore, the presence of sulphuric acid in the treatment that provides high quantity of oxygenated species on the surface seems to be the main responsible for the different behavior observed during the carbon dioxide reduction on Fe/Vulcan NSTa0.5 electrode.

5. Conclusions

Fe catalysts supported on Vulcan XC-72R were synthesized by the polyol method, using ethylenglycol as solvent and reducing agent. Before the metal deposition, surface chemistry of the Vulcan was modified by different oxidation treatments in order to study the influence of the surface chemistry of the support on the catalytic properties of the materials. During these treatments surface oxygen groups were created, being HNO_3 treatment at boiling temperature for 2 h the most effective in creating functional groups, while $\text{HNO}_3\text{-H}_2\text{SO}_4$ treatment at room temperature produces the highest CO/CO_2 ratio of functional groups in the surface. These treatments strongly affect the behavior of the iron-based catalysts toward the carbon dioxide reduction. In fact, two main reaction paths were identified during the carbon dioxide reduction, both influenced by the surface properties of the carbon support. Additionally, these treatments also modified the textural and morphological properties of Vulcan. A decrease of the surface area, as well as a partial destruction of its structure, was observed as the severity of oxidation treatments increased. Finally, Fe/Vulcan NSTa0.5 and Fe/Vulcan NcTb0.5 present the highest and lowest catalytic activity toward the hydrogen evolution reaction, though both catalysts develop the highest production of the mass signal 45 (formic acid and/or higher carbon-chain products) in presence of dissolved CO_2 .

Acknowledgments

The authors gratefully acknowledge financial support given by MICINN (MAT2008-06631-C03-01 and 02) and Gobierno de Aragón and Obra Social La Caixa (GA-LC-008/2009). S. Pérez-Rodríguez acknowledges Gobierno de Aragón for the DGA grant. G. García acknowledges to the JAE program (CSIC) for financial support.

References

- [1] S. Ichikawa, "Chemical conversion of carbon dioxide by catalytic hydrogenation and room temperature photoelectrocatalysis," *Energy Conversion and Management*, vol. 36, no. 6–9, pp. 613–616, 1995.
- [2] T. Inui, M. Anpo, K. Izui, S. Yanagida, and T. Yamaguchi, *Advances in Chemical Conversions for Mitigating Carbon Dioxide*, Elsevier Science, Amsterdam, The Netherlands, 1998.
- [3] M. M. Halmann, *Greenhouse Gas Carbon Dioxide Mitigation*, Lewis, Washington, DC, USA, 1999.
- [4] Ch. Song, A. Gaffney, and K. Fujimoto, *CO_2 Conversion and Utilization*, American Chemical Society, Washington, DC, USA, 2009.
- [5] F. R. Keene and B. P. Sullivan, "Mechanisms of the electrochemical reduction of carbon dioxide catalyzed by transition metal complexes," in *Electrochemical and Electrocatalytic Reactions of Carbon Dioxide*, B. P. Sullivan, K. Krist, and H. E. Guard, Eds., Elsevier, Amsterdam, The Netherlands, 1993.
- [6] M. Aulice Scibioh and V. R. Vijayaraghavan, "Electrocatalytic reduction of carbon dioxide : its relevance and importance," *Journal of Scientific and Industrial Research*, vol. 57, no. 3, pp. 111–123, 1998.
- [7] M. M. Halmann, *Chemical Fixation of Carbon Dioxide: Methods for Recycling CO_2 into Useful Products*, CRC Press, Boca Raton, Fla, USA, 1993.
- [8] B. P. Sullivan, *Electrochemical and Electrocatalytic Reduction of Carbon Dioxide*, Elsevier Press, Amsterdam, Netherlands, 1993.
- [9] T. Weimer, K. Schaber, M. Specht, and A. Bandi, "Methanol from atmospheric carbon dioxide: a liquid zero emission fuel for the future," *Energy Conversion and Management*, vol. 37, no. 6–8, pp. 1351–1356, 1996.
- [10] D. Mignard, M. Sahibzada, J. M. Duthie, and H. W. Whittington, "Methanol synthesis from flue-gas CO_2 and renewable electricity: a feasibility study," *International Journal of Hydrogen Energy*, vol. 28, no. 4, pp. 455–464, 2003.
- [11] M. Jitaru, "Electrochemical carbon dioxide reduction—Fundamental and applied topics (review)," *Journal of the University of Chemical Technology and Metallurgy*, vol. 42, no. 4, pp. 333–344, 2007.
- [12] M. Gattrell, N. Gupta, and A. Co, "A review of the aqueous electrochemical reduction of CO_2 to hydrocarbons at copper," *Journal of Electroanalytical Chemistry*, vol. 594, no. 1, pp. 1–19, 2006.
- [13] I. Taniguchi, "Electrochemical and photoelectrochemical reduction of carbon dioxide," in *Modern Aspects of Electrochemistry*, J. O'M. Bockris, R. E. White, and B. E. Conway, Eds., p. 327, Plenum, New York, NY, USA, 1989.
- [14] D. L. DuBois, "Electrochemical reactions of carbon dioxide," in *Encyclopaedia of Electrochemistry*, A. J. Bard and M. Stratmann, Eds., pp. 202–225, Wiley-VCH, Weinheim, Germany, 2006.

- [15] Y. Hori, H. Wakebe, T. Tsukamoto, and O. Koga, "Electrocatalytic process of CO selectivity in electrochemical reduction of CO₂ at metal electrodes in aqueous media," *Electrochimica Acta*, vol. 39, no. 11-12, pp. 1833-1839, 1994.
- [16] Y. Hori, "CO₂ reduction catalyzed by metal electrodes," in *Handbook of Fuel Cells—Fundamentals, Technology and Applications*, W. Vielstich, H. A. Gasteiger, and A. Lamm, Eds., vol. 2, pp. 720-733, John Wiley & Sons, New York, NY, USA, 2003.
- [17] M. Azuma, K. Hashimoto, M. Hiramoto, M. Watanabe, and T. Sakata, "Electrochemical reduction of carbon dioxide on various metal electrodes in low-temperature aqueous KHCO₃ media," *Journal of the Electrochemical Society*, vol. 137, no. 6, pp. 1772-1778, 1990.
- [18] K. Hara, A. Kudo, and T. Sakata, "Electrochemical reduction of carbon dioxide under high pressure on various electrodes in an aqueous electrolyte," *Journal of Electroanalytical Chemistry*, vol. 391, no. 1-2, pp. 141-147, 1995.
- [19] S. Nakagawa, A. Kudo, M. Azuma, and T. Sakata, "Effect of pressure on the electrochemical reduction of CO₂ on Group VIII metal electrodes," *Journal of Electroanalytical Chemistry*, vol. 308, no. 1-2, pp. 339-343, 1991.
- [20] K. Hara, A. Kudo, and T. Sakata, "Electrochemical reduction of high pressure carbon dioxide on Fe electrodes at large current density," *Journal of Electroanalytical Chemistry*, vol. 386, no. 1-2, pp. 257-260, 1995.
- [21] H. De Jesús-Cardona, C. Del Moral, and C. R. Cabrera, "Voltammetric study of CO₂ reduction at Cu electrodes under different KHCO₃ concentrations, temperatures and CO₂ pressures," *Journal of Electroanalytical Chemistry*, vol. 513, no. 1, pp. 45-51, 2001.
- [22] S. Kaneco, N. H. Hiei, Y. Xing et al., "High-efficiency electrochemical CO₂-to-methane reduction method using aqueous KHCO₃ media at less than 273 K," *Journal of Solid State Electrochemistry*, vol. 7, no. 3, pp. 152-156, 2003.
- [23] S. Kaneco, N. H. Hiei, Y. Xing et al., "Electrochemical conversion of carbon dioxide to methane in aqueous NaHCO₃ solution at less than 273 K," *Electrochimica Acta*, vol. 48, no. 1, pp. 51-55, 2002.
- [24] M. Azuma, K. Hashimoto, M. Hiramoto, M. Watanabe, and T. Sakata, "Carbon dioxide reduction at low temperature on various metal electrodes," *Journal of Electroanalytical Chemistry*, vol. 260, no. 2, pp. 441-445, 1989.
- [25] T. Saeki, K. Hashimoto, N. Kimura, K. Omata, and A. Fujishima, "Electrochemical reduction of CO₂ with high current density in a CO₂ + methanol medium at various metal electrodes," *Journal of Electroanalytical Chemistry*, vol. 404, no. 2, pp. 299-302, 1996.
- [26] T. Saeki, K. Hashimoto, N. Kimura, K. Omata, and A. Fujishima, "Electrochemical reduction of CO₂ with high current density in a CO₂ + methanol medium II. CO formation promoted by tetrabutylammonium cation," *Journal of Electroanalytical Chemistry*, vol. 390, no. 1-2, pp. 77-82, 1995.
- [27] K. Ohta, M. Kawamoto, T. Mizuno, and D. A. Lowy, "Electrochemical reduction of carbon dioxide in methanol at ambient temperature and pressure," *Journal of Applied Electrochemistry*, vol. 28, no. 7, pp. 717-724, 1998.
- [28] S. Ohya, S. Kaneco, H. Katsumata, T. Suzuki, and K. Ohta, "Electrochemical reduction of CO₂ in methanol with aid of CuO and Cu₂O," *Catalysis Today*, vol. 148, no. 3-4, pp. 329-334, 2009.
- [29] S. Kaneco, K. Iiba, H. Katsumata, T. Suzuki, and K. Ohta, "Electrochemical reduction of high pressure CO₂ at a Cu electrode in cold methanol," *Electrochimica Acta*, vol. 51, no. 23, pp. 4880-4885, 2006.
- [30] S. Kaneco, K. Iiba, K. Ohta, and T. Mizuno, "Electrochemical reduction of carbon dioxide on copper in methanol with various potassium supporting electrolytes at low temperature," *Journal of Solid State Electrochemistry*, vol. 3, no. 7-8, pp. 424-428, 1999.
- [31] T. Mizuno, A. Naitoh, and K. Ohta, "Electrochemical reduction of CO₂ in methanol at -30°C," *Journal of Electroanalytical Chemistry*, vol. 391, no. 1-2, pp. 199-201, 1995.
- [32] P. A. Christensen, A. Hamnett, A. V. G. Muir, and N. A. Freeman, "CO₂ reduction at platinum, gold and glassy carbon electrodes in acetonitrile. An in-situ FTIR study," *Journal of Electroanalytical Chemistry*, vol. 288, no. 1-2, pp. 197-215, 1990.
- [33] J. P. Hindermann, G. J. Hutchings, and A. Kiennemann, "Mechanistic aspects of the formation of hydrocarbons and alcohols from CO hydrogenation," *Catalysis Reviews*, vol. 35, no. 1, pp. 1-127, 1993.
- [34] K. Hara, A. Kudo, and T. Sakata, "Electrochemical CO₂ reduction on a glassy carbon electrode under high pressure," *Journal of Electroanalytical Chemistry*, vol. 421, no. 1-2, pp. 1-4, 1997.
- [35] C. W. B. Bezerra, L. Zhang, H. Liu et al., "A review of heat-treatment effects on activity and stability of PEM fuel cell catalysts for oxygen reduction reaction," *Journal of Power Sources*, vol. 173, no. 2, pp. 891-908, 2007.
- [36] Y. Shao, G. Yin, J. Zhang, and Y. Gao, "Comparative investigation of the resistance to electrochemical oxidation of carbon black and carbon nanotubes in aqueous sulfuric acid solution," *Electrochimica Acta*, vol. 51, no. 26, pp. 5853-5857, 2006.
- [37] C. Prado-Burguete, A. Linares-Solano, F. Rodríguez-Reinoso, and C. S. M. de Lecea, "The effect of oxygen surface groups of the support on platinum dispersion in Pt/carbon catalysts," *Journal of Catalysis*, vol. 115, no. 1, pp. 98-106, 1989.
- [38] M. J. Lázaro, L. Calvillo, V. Celorrio, J. I. Pardo, S. Perathoner, and R. Moliner, "Study and application of carbon black Vulcan XC-72R in polymeric electrolyte fuel cells," in *Carbon Black: Production, Properties and Uses*, I. J. Sanders and T. L. Peeten, Eds., 2011.
- [39] S. Pérez Rodríguez, M. Corengia, G. García, F. C. Zinola, M. J. Lázaro, and E. Pastor, "Gas diffusion electrodes for methanol electro-oxidation studied by a new DEMS configuration: Influence of the diffusion layer," accepted for publication in *International Journal of Hydrogen Energy*.
- [40] J. L. Figueiredo, M. F. R. Pereira, M. M. A. Freitas, and J. J. M. Órfão, "Modification of the surface chemistry of activated carbons," *Carbon*, vol. 37, no. 9, pp. 1379-1389, 1999.
- [41] D. Sebastián, I. Suelves, R. Moliner, and M. J. Lázaro, "The effect of the functionalization of carbon nanofibers on their electronic conductivity," *Carbon*, vol. 48, no. 15, pp. 4421-4431, 2010.
- [42] C. Prado-Burguete, A. Linares-Solano, F. Rodríguez-Reinoso, and C. S. M. de Lecea, "The effect of oxygen surface groups of the support on platinum dispersion in Pt/carbon catalysts," *Journal of Catalysis*, vol. 115, no. 1, pp. 98-106, 1989.
- [43] X. Liu, R. Tang, Q. He, X. Liao, and B. Shi, "Fe(III)-loaded collagen fiber as a heterogeneous catalyst for the photo-assisted decomposition of malachite green," *Journal of Hazardous Materials*, vol. 174, no. 1-3, pp. 687-693, 2010.
- [44] O. Wolter and J. Heitbaum, "Differential electrochemical mass spectroscopy (dems)- a new method for the study of electrode processes," *Physical Chemistry*, vol. 88, no. 1, pp. 2-6, 1984.

- [45] P. Dubé and G. M. Brisard, "Influence of adsorption processes on the CO₂ electroreduction: an electrochemical mass spectrometry study," *Journal of Electroanalytical Chemistry*, vol. 582, no. 1-2, pp. 230–240, 2005.
- [46] R. P. S. Chaplin and A. A. Wragg, "Effects of process conditions and electrode material on reaction pathways for carbon dioxide electroreduction with particular reference to formate formation," *Journal of Applied Electrochemistry*, vol. 33, no. 12, pp. 1107–1123, 2003.

Research Article

Investigation of the Performance of Au_{core}-Pd_{shell}/C as the Anode Catalyst of Direct Borohydride-Hydrogen Peroxide Fuel Cell

Hong Wang,¹ Ying Wang,² Xianyou Wang,¹ Peiying He,¹ Lanhua Yi,¹ Wei Yi,¹ and Xue Liu¹

¹Key Laboratory of Environmentally Friendly Chemistry and Applications of Ministry of Education, School of Chemistry, Xiangtan University, Hunan 411105, China

²School of Chemical Engineering and Pharmacy, Wuhan Institute of Technology, Hubei 430073, China

Correspondence should be addressed to Xianyou Wang, wxianyou@yahoo.com

Received 26 April 2011; Accepted 7 September 2011

Academic Editor: Carlos F. Zinola

Copyright © 2011 Hong Wang et al. This is an open access article distributed under the Creative Commons Attribution License, which permits unrestricted use, distribution, and reproduction in any medium, provided the original work is properly cited.

The carbon-supported bimetallic Au-Pd catalyst with core-shell structure is prepared by successive reduction method. The core-shell structure, surface morphology, and electrochemical performances of the catalysts are characterized by X-ray diffraction (XRD), transmission electron microscopy (TEM), ultraviolet-visible absorption spectrometry, linear sweep voltammetry, and chronopotentiometry. The results show that the Au-Pd/C catalyst with core-shell structure exhibits much higher catalytic activity for the direct oxidation of NaBH₄ than pure Au/C catalyst. A direct borohydride-hydrogen peroxide fuel cell, in which the Au-Pd/C with core-shell structure is used as the anode catalyst and the Au/C as the cathode catalyst, shows as high as 68.215 mW cm⁻² power density.

1. Introduction

Fuel cells constitute an attractive class of renewable and sustainable energy sources alternative to conventional energy sources such as petroleum that has finite reserves. Among all types of fuel cells, the direct borohydride-hydrogen peroxide fuel cell (DBHFC) has recently attracted increasing attentions because of some excellent features such as high open circuit potential, low operation temperature, and high power density [1–8]. The DBHFC is comprised of BH₄⁻ oxidation at the anode and H₂O₂ reduction at the cathode; thus, it can be used as a promising power source for space and underwater applications. Generally, the key of development of DBHFC is anode electrocatalyst Cao et al. [9] have prepared Au/Ni-foam electrode by spontaneous deposition of Au nanoparticles on nickel foam substrates and achieved an open-circuit voltage of about 1.07 V and a peak power density of 100 mW cm⁻² at 170 mA cm⁻² and 0.6 V at 60°C. Chatenet et al. [10] reported that electrooxidation of BH₄⁻ can exchange about 7.5 electrons on Au and Ag electrodes in contrast to about 4 electrons on Pt electrode. The high electron utilization efficiencies of Au and Ag towards BH₄⁻ electrooxidation are attributed to their low activity towards

BH₄⁻ hydrolysis. However, the catalyst, which causes the low activity towards BH₄⁻ hydrolysis, simultaneously has a low catalytic activity towards BH₄⁻ electrochemical oxidation reaction. Thus, it is very important for DBHFC application to develop high-activity electrocatalysts for the borohydride oxidation reaction (BOR).

In our previous works, high-activity catalysts such as carbon-supported hollow gold nanoparticles (HAu/C) [11, 12] and AuCo/C [13] have been studied. Usually, the core-shell structure is an effective morphology to enhance catalytic activity. The improvement of catalytic activity of core-shell bimetallic nanoparticles is attributed to the unique structure in electrocatalysis, which has gained much attention in recent years [14]. Besides, the activity of core-shell structure is related with the underlying interface between the core and shell metals due to the bimetallic mechanism [15]. It is reported that the core-shell nanoparticle catalysts such as Ni@Pd/MWCNTs [16] and Pt_{shell}-Au_{core}/C [17] have effectively enhanced the catalytic activity for the electrooxidation of methanol. Palladium is an appropriate choice as the shell of the catalyst since it has the similar catalytic activity as platinum, which is more expensive than the former. In this paper, carbon-supported bimetallic Au-Pd catalyst

with the core-shell structure was prepared by successive reduction method. The electrochemical performances for the borohydride oxidation reaction were examined by linear voltammetry, chronoamperometry, chronopotentiometry, and fuel-cell performance measurement.

2. Experimental

2.1. Preparation of Carbon-Supported Core-Shell Au-Pd Nanoparticles. The preparation of Au seed was reported elsewhere [18, 19]. Concisely, the citrate-stabilized Au nanoparticles were prepared by NaBH_4 reduction of 0.5 mM HAuCl_4 aqueous solution in the presence of trisodium citrate in 100 mL ice ultrapure (18.2 k Ω) water with vigorous stirring [20]. Stirring was continued for 12 h to decompose the unreacted NaBH_4 . Then 0.25 mL 0.1 M H_2PdCl_4 aqueous solution and freshly prepared 1.25 mL 0.1 M ascorbic acid aqueous solution were added dropwise to the Au hydrosol. The solution was continuously stirred for 2 h and then added 50 mg Vulcan XC-72R carbon slurry (metal loading was 20 wt. %). After stirring 5 h, the suspension was filtrated to recover solid product, which was fully washed with water and alcohol. The recovered solid product was dried in vacuum at 80°C overnight. Comparatively, carbon-supported monometallic Pd and Au samples with the same overall metal loading were prepared by similar procedures.

2.2. Characterization of Anode Catalysts. The samples for transmission electron microscopy (TEM) were prepared by putting one drop of the sample slurry on a copper grid followed by drying in a desiccator. Electron micrographs were taken with a FEI Tecnai G2 microscope at 200 kV. A diffractometer (D/MAX-3C) was employed using Cu K α radiation ($\lambda = 1.54056 \text{ \AA}$) and a graphite monochromator at 50 kV, 100 mA, to obtain XRD spectra of the samples. Continuous X-ray scans were carried out from 10° to 90° of 2θ . The UV-Vis spectra of the hydrosols were measured by a Lambda 25 spectrometer equipped with quartz cells.

2.3. Electrochemical Performance of Anode Catalysts. A conventional three-electrode cell was used to perform the electrochemical tests of the anode catalysts at 25°C with a CHI660A Electrochemistry Workstation. The Au-Pd/C was used as working electrode, an Ni foam mesh with $3 \times 5 \text{ cm}^2$ as counter electrode and an Ag/AgCl, KCl_{std} as the reference electrode. The electrolyte was 0.1 M $\text{NaBH}_4 + 3.0 \text{ M NaOH}$. The working electrode was prepared as follows: 5 mg of Au-Pd/C powder was dispersed by ultrasonic for 2 h in 0.5 mL blend solution of 0.125 mL 5 wt. % Nafion solution and 0.375 mL deionized water. Then 5 μL of slurry was pasted on the surface of the glassy carbon (GC) electrode (3 mm in diameter) which was polished to mirror by 0.5 μm alumina and sonicated 5 min prior to use. The dispersed catalyst on the GC surface was dried for 5 h at ambient temperature.

2.4. Fuel Cell Test. The performance of the direct $\text{NaBH}_4\text{-H}_2\text{O}_2$ fuel cell (DBHFC) was evaluated by a battery testing system at 25°C in standard atmospheric pressure. The schematic of direct $\text{NaBH}_4\text{-H}_2\text{O}_2$ fuel cell was shown in

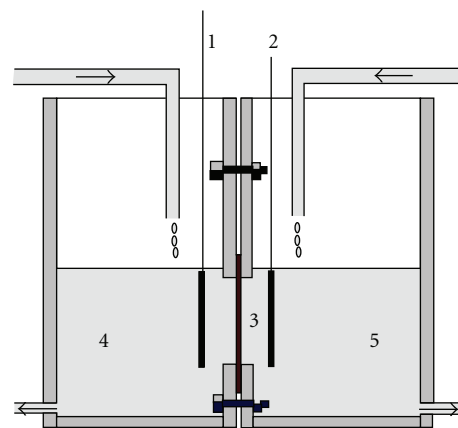


FIGURE 1: Simple schematic illustration of DBHFC (1) anode catalyst, (2) cathode catalyst, (3) the activated Nafion 117 membrane, (4) 1 M $\text{NaBH}_4 + 3 \text{ M NaOH}$, and (5) 2 M $\text{H}_2\text{O}_2 + 0.5 \text{ M H}_2\text{SO}_4$.

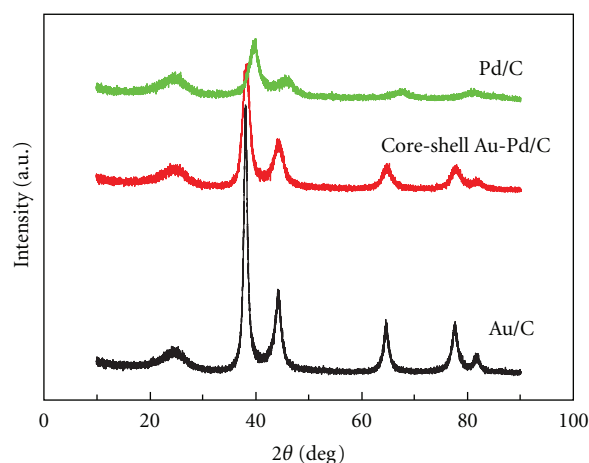


FIGURE 2: XRD patterns of Au/C, core-shell Au-Pd/C, and Pd/C.

Figure 1, and it consisted of Au/C cathode, core-shell Au-Pd/C anode, activated Nafion 117 membrane separator, anolyte composed of 1 M $\text{NaBH}_4 + 3 \text{ M NaOH}$, and catholyte composed of 2 M $\text{H}_2\text{O}_2 + 0.5 \text{ M H}_2\text{SO}_4$. The fresh anolyte and catholyte were continuously supplied and withdrawn from the cell at a rate of 0.7 mL min^{-1} during the testing process. The load was applied in steps of 5 mA within the range of 0–150 mA. Each step lasted 2 min, and the current was continuously applied from one value to the next without disconnecting the cell.

The catalyst ink was made by mixing isopropyl Nafion solution and carbon-supported catalyst and coated onto stainless steel gauze. Then it was dried in vacuum at 80°C for 12 h and pressed at 16 MPa for 1 min. Finally, the loading mass of catalysts was about 4.5 mg cm^{-2} .

3. Results and Discussion

3.1. Physical Characterization. Figure 2 showed the XRD patterns of Au/C, core-shell Au-Pd/C, and Pd/C. As shown in Figure 2, the rather wide diffraction peaks at $2\theta \approx 25^\circ$ in

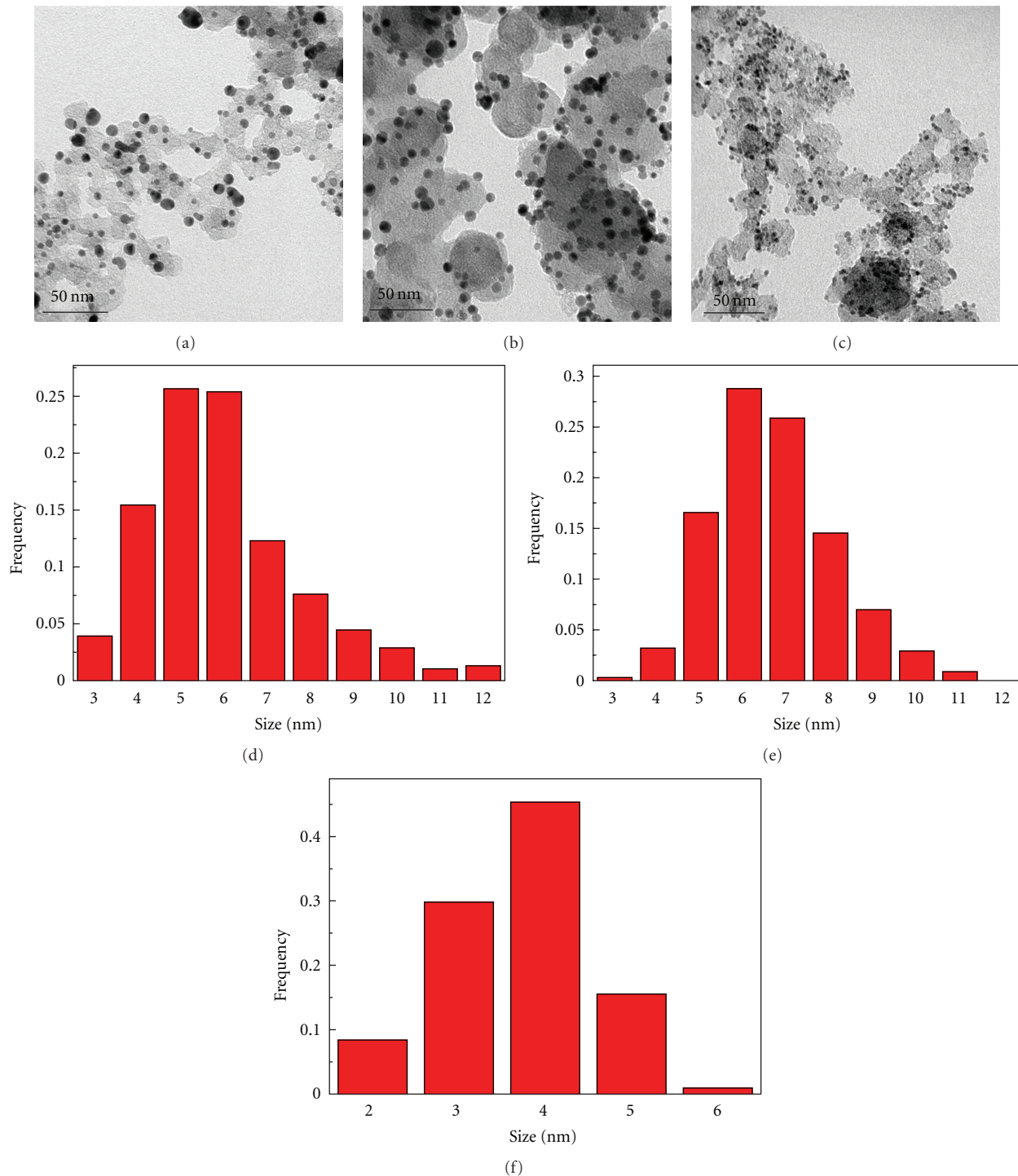


FIGURE 3: TEM images of Au/C (a), core-shell Au-Pd/C (b), and Pd/C (c) and their corresponding histograms on size distribution.

all three samples are attributed to Vulcan XC-72R carbon (002) crystal face. In Au and core-shell Au-Pd catalysts, there are other five main characteristic peaks, which could be attributed to the face-centered cubic (fcc) structure of crystalline Au (111), (200), (220), (311), and (222). These indicated the absence of both isolated large-size Pd particles and the bulk Au-Pd alloy phases in the core-shell Au-Pd/C catalyst. The morphologies and particle distributions of

the carbon-supported Au/C, core-shell Au-Pd/C, and Pd/C samples were showed in Figure 3. The corresponding histograms on size distribution of electrocatalysts were also simultaneously given in Figures 3(d), 3(e), and 3(f). It could be seen from Figure 3 that the spheroidal nanoparticles were homogeneously dispersed on the surface of the carbon supporter. The average diameter of Au, core-shell Au-Pd, and Pd particles in samples from counting more than 300

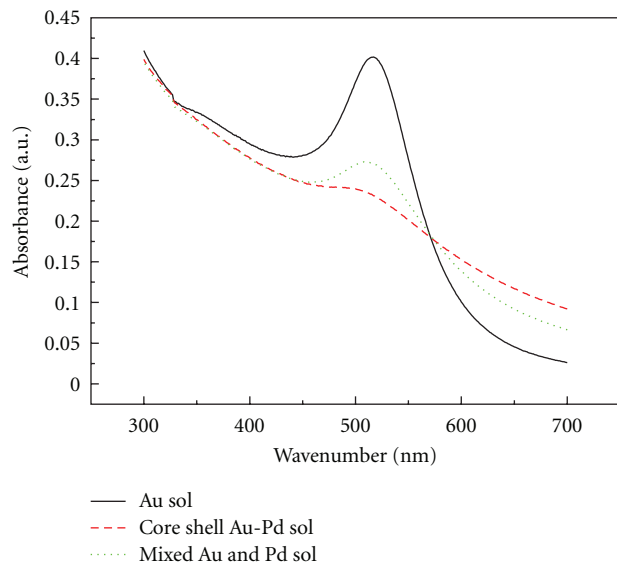


FIGURE 4: Absorption spectra of Au, core-shell Au-Pd, and mixed Au-Pd hydrosols before deposition on carbon.

particles were about 5.955 nm, 6.705 nm, and 3.613 nm, respectively. Usually, the size of the particle with core-shell structure, D , can be calculated by [21]

$$D = D_{\text{core}} \left(1 + \frac{V_{\text{Pd}}[\text{Pd}]}{V_{\text{Au}}[\text{Au}]} \right)^{1/3} \quad (1)$$

Here, D_{core} was the measured Au particles size; V_{Pd} and V_{Au} were the academic Pd and Au mole volume, respectively; $[\text{Pd}]$ and $[\text{Au}]$ were the overall concentrations of the two metals involved, respectively. It had been found from the above formula that the calculated size of core-shell Au-Pd particle was 6.719 nm, which is close to actually measured particle size (6.705 nm). Besides, the calculated Pd shell thickness was about 0.375 nm.

The absorption spectra of Au hydrosol, core-shell Au-Pd hydrosol, and mixed Au-Pd hydrosol were shown on Figure 4. The absorption peak positioned at 516 nm, which was ascribed to the surface plasmon resonance (SPR) of Au, could be clearly observed for Au hydrosol. For the mixed Au-Pd hydrosol, the Au plasmon absorption peak declined slightly because of the decrease of the Au hydrosol concentration. However, for the core-shell Au-Pd hydrosol, the remaining Au plasmon absorption peak indicated that the Pd shell was not too thick to overwhelm the SPR response of the Au nanoparticles [22].

3.2. Electrochemical Performance of Anode Catalysts. Figure 5 showed the linear sweep voltammogram (LSV) of different catalysts in 0.1 M $\text{NaBH}_4 + 3.0$ M NaOH solution at 25°C at a potential sweep rate of 20 mV s^{-1} in the potential range of -1.2 V to 0.6 V versus Ag/AgCl. The Au-Pd/C with core-shell structure and Pd/C exhibited more negative initial reaction potentials than Au/C due to the BH_4^- hydrolysis. The current densities of Au/C, core-shell Au-Pd/C, and Pd/C were 20.80 mA cm^{-2} , 24.35 mA cm^{-2} , and 27.89 mA cm^{-2}

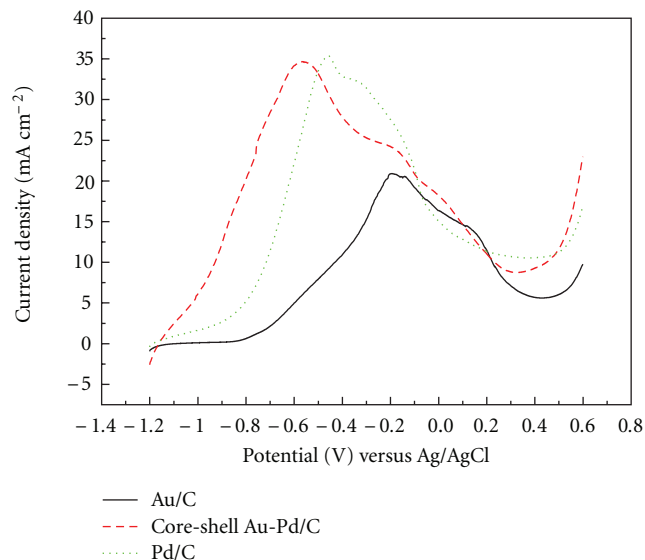


FIGURE 5: Linear sweep voltammogram of Au/C, core-shell Au-Pd/C, and Pd/C electrodes.

at -0.2 V versus Ag/AgCl, respectively. The peak current density of Au-Pd/C (34.65 mA cm^{-2}) was nearly close to Pd/C (35.44 mA cm^{-2}), which was about 1.7 times higher than that of Au/C (20.80 mA cm^{-2}). Besides, the area enclosed by LSV on core-shell Au-Pd/C electrode was apparently bigger than that on Au/C and Pd/C electrodes. Obviously, the above results indicated that the core-shell Au-Pd/C catalyst had much better catalytic activity than pure Au and Pd catalysts. Moreover, the core-shell Au-Pd/C (4.25 wt. % Pd loading) was more economical than Pd/C (20 wt. % Pd loading). The reasons why the core-shell Au-Pd/C enhanced the catalytic activity of the borohydride oxidation reaction could correlate with the long-range electromagnetic enhancement between the Au core and the Pd shell [23].

Chronopotentiometry was a usefully qualitative screening method for catalyst since it simulated the constant current operation of a fuel cell. Figure 6 showed the chronopotentiometry curves of BH_4^- oxidation on the Au/C, core-shell Au-Pd/C, and Pd/C at a current density of 8.5 mA cm^{-2} in a solution of 0.1 M $\text{NaBH}_4 + 3$ M NaOH, respectively. The open-circuit potentials (OCPs) were -0.953 V versus Ag/AgCl for Au/C, -1.203 V versus Ag/AgCl for core-shell Au-Pd/C, and -1.188 V versus Ag/AgCl for Pd/C. After 120 s, the operating potential for Au/C, core-shell Au-Pd/C, and Pd/C was -0.653 V, -0.920 V, and -0.800 V, respectively. Therefore, it can be expected that the core-shell Au-Pd/C catalyst had higher direct electrooxidation catalytic activity and power output than those of Au/C and Pd/C under the same experimental condition, which also suggested the possibility of potentially obtaining a higher power output.

In chronoamperometry experiments (Figure 7(a)), the potential was stepped from -1.2 to -0.2 V versus Ag/AgCl in 0.1 M $\text{NaBH}_4 + 3$ M NaOH solution. At the beginning of the experiment, the initial current densities of three carbon-supported catalysts corresponded mainly to double-layer charging. The core-shell Au-Pd/C and Pd/C showed

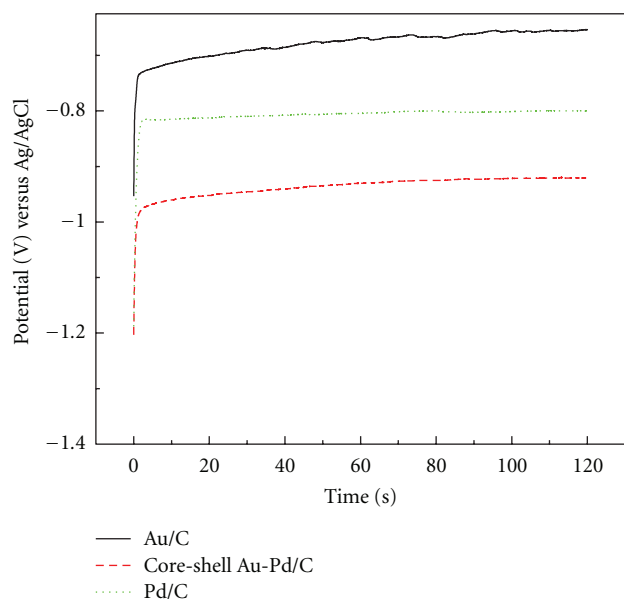
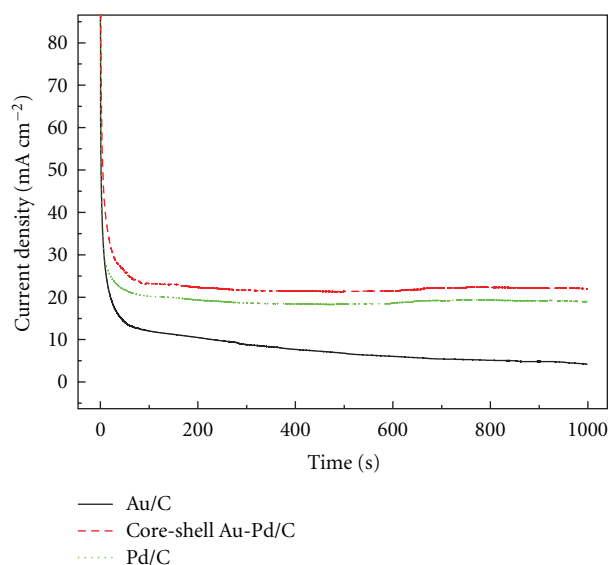


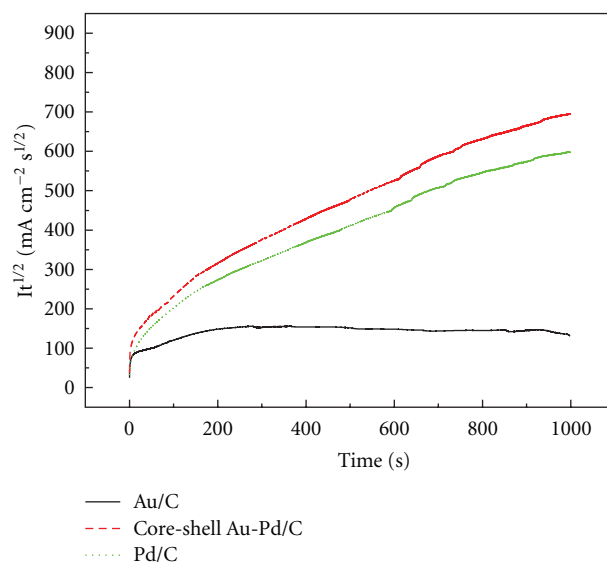
FIGURE 6: Chronopotentiometry curves of Au/C, core-shell Au-Pd/C and Pd/C electrodes.

a gradual current density decay with the increase of the time before a steady current density was reached. However, the current density slowly decayed on Au/C, which would be related to the formation of borohydride oxidation products [10]. The current in the steady-state region represented the current of the electrochemical reaction, so it could reflect partly the electrocatalytic activity of the electrodes. As being shown in Figure 7(a), the core-shell Au-Pd/C catalyst maintained a higher borohydride oxidation current density than those of the other two catalysts. In order to analyze well the electrocatalytic activity of BH_4^- on the different catalysts, the chronoamperometry results were summarized as a Cottrell plot in Figure 7(b). The approximate constancy of the $It^{1/2}$ versus t on Au/C in the steady process could be attributed to electrode deactivation. On the other hand, the increase of $It^{1/2}$ value with the increase of the time on core-shell Au-Pd/C and Pd/C indicated that neither the intracatalyst layer diffusion nor the external mass transfer of BH_4^- became rate limiting under the employed conditions [24]. And core-shell Au-Pd/C had larger $It^{1/2}$ value than Pd/C, which indicates the higher activity of oxidation of BH_4^- . Moreover, the increasing value suggested the surfaces of Au-Pd/C and Pd/C are not poisoned during the experiment process.

3.3. Fuel Cell Performance. The cell polarization and power density curves for DBHFC using 1 M $\text{NaBH}_4 + 3$ M NaOH solution as fuel and 2 M $\text{H}_2\text{O}_2 + 0.5$ M H_2SO_4 solution as oxidant were presented in Figure 8. In the experimental cell, the Au/C was used as the cathode catalyst and Au/C, core-shell Au-Pd/C, and Pd/C as the anode catalyst, respectively. The cell voltage had an initially abrupt reduction at the range of 0–10 mA cm^{-2} current density on Au/C, which showed a kinetic process of electrochemistry polarization. For the Pd/C and core-shell Au-Pd/C electrodes, the cell



(a)



(b)

FIGURE 7: (a) Chronoamperometry curves of BH_4^- oxidation on different anode catalysts and (b) Cottrell's plot generated from the chronoamperometry data.

voltage curves linearly decreased with the increase of current density, indicating a strong dependence of cell performance on the ohmic resistance (mainly ohmic polarization). In addition, the slope of the polarization curve on the core-shell Au-Pd/C catalyst electrode was lower than that on Pd/C. This phenomenon showed that the core-shell Au-Pd/C catalyst can decrease oxidation overpotential of BH_4^- and improve the performance of DBHFC. Furthermore, the core-shell Au-Pd/C exhibited a maximum power density of 68.215 mW cm^{-2} at a current density of 90.1 mA cm^{-2} and a cell voltage of 0.757 V at 25°C.

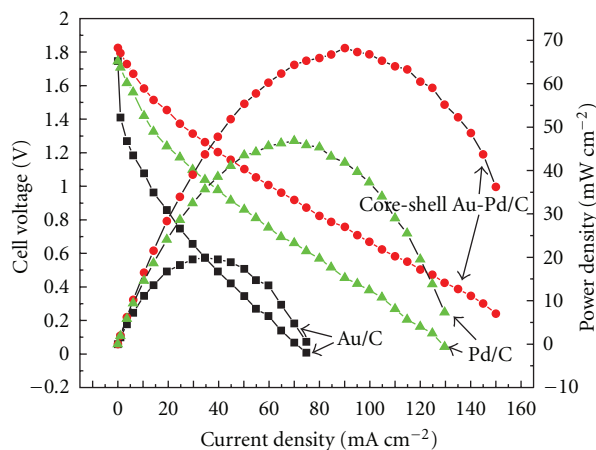


FIGURE 8: Cell polarization curves and power density curves of the DBHFC using various anode catalysts.

4. Conclusions

The carbon-supported bimetallic Au-Pd catalyst with the core-shell structure was successfully prepared by successive reduction method. The spheroidal Au-Pd nanoparticles were homogeneously dispersed on the surface of carbon supporter. Compared with carbon-supported monometallic Au and Pd catalysts, the core-shell Au-Pd catalyst had an enhanced electrocatalytic activity for the BH_4^- electrooxidation. The fuel cell using core-shell Au-Pd as anode catalyst presented a maximum power density of $68.215 \text{ mW cm}^{-2}$ and a cell voltage of 0.757 V in $1 \text{ M NaBH}_4 + 3 \text{ M NaOH}$ solution at 25°C . Therefore, the carbon-supported bimetallic Au-Pd catalyst with the core-shell structure would be a promising anode electrocatalyst for the application of DBHFC.

Acknowledgments

This work was financially supported by the National Natural Science Foundation of China (Grants no. 20871101 and 51072173), the Doctoral Fund of Ministry of Education of China (Grant no. 20094301110005), and the project supported by Science and Technology Department of Hunan Province (Grant no. 2010GK3181).

References

- [1] J. Ma, N. A. Choudhury, and Y. Sahai, "A comprehensive review of direct borohydride fuel cells," *Renewable and Sustainable Energy Reviews*, vol. 14, no. 1, pp. 183–199, 2010.
- [2] S. Y. Park, D. W. Lee, I. S. Park, Y. K. Hong, Y. M. Park, and K. Y. Lee, "The effective bimetallic component of Pd-Au/C for electrochemical oxidation of borohydrides," *Current Applied Physics*, vol. 10, no. 2, pp. S40–S43, 2010.
- [3] R. K. Raman, N. A. Choudhury, and A. K. Shukla, "A high output voltage direct borohydride fuel cell," *Electrochemical and Solid-State Letters*, vol. 7, no. 12, pp. A488–A491, 2004.
- [4] P. He, Y. Wang, X. Wang et al., "Investigation of carbon supported Au-Ni bimetallic nanoparticles as electrocatalyst for

direct borohydride fuel cell," *Journal of Power Sources*, vol. 196, no. 3, pp. 1042–1047, 2011.

- [5] G. H. Miley, N. Luo, J. Mather et al., "Direct $\text{NaBH}_4/\text{H}_2\text{O}_2$ fuel cells," *Journal of Power Sources*, vol. 165, no. 2, pp. 509–516, 2007.
- [6] C. P. de León, F. C. Walsh, A. Rose, J. B. Lakeman, D. J. Browning, and R. W. Reeve, "A direct borohydride-Acid peroxide fuel cell," *Journal of Power Sources*, vol. 164, no. 2, pp. 441–448, 2007.
- [7] L. Gu, N. Luo, and G. H. Miley, "Cathode electrocatalyst selection and deposition for a direct borohydride/hydrogen peroxide fuel cell," *Journal of Power Sources*, vol. 173, no. 1, pp. 77–85, 2007.
- [8] W. Haijun, W. Cheng, L. Zhixiang, and M. Zongqiang, "Influence of operation conditions on direct $\text{NaBH}_4/\text{H}_2\text{O}_2$ fuel cell performance," *International Journal of Hydrogen Energy*, vol. 35, no. 7, pp. 2648–2651, 2010.
- [9] D. Cao, Y. Gao, G. Wang, R. Miao, and Y. Liu, "A direct $\text{NaBH}_4-\text{H}_2\text{O}_2$ fuel cell using Ni foam supported Au nanoparticles as electrodes," *International Journal of Hydrogen Energy*, vol. 35, no. 2, pp. 807–813, 2010.
- [10] M. Chatenet, F. Micoud, I. Roche, and E. Chainet, "Kinetics of sodium borohydride direct oxidation and oxygen reduction in sodium hydroxide electrolyte. Part I. BH_4^- electro-oxidation on Au and Ag catalysts," *Electrochimica Acta*, vol. 51, no. 25, pp. 5459–5467, 2006.
- [11] J. Wei, X. Wang, Y. Wang, Q. Chen, F. Pei, and Y. Wang, "Investigation of carbon-supported Au hollow nanospheres as electrocatalyst for electrooxidation of sodium borohydride," *International Journal of Hydrogen Energy*, vol. 34, no. 8, pp. 3360–3366, 2009.
- [12] J. Wei, X. Wang, Y. Wang et al., "Carbon-supported Au hollow nanospheres as anode catalysts for direct borohydride-hydrogen peroxide fuel cells," *Energy and Fuels*, vol. 23, no. 8, pp. 4037–4041, 2009.
- [13] F. Pei, Y. Wang, X. Wang et al., "Performance of supported Au-Co alloy as the anode catalyst of direct borohydride-hydrogen peroxide fuel cell," *International Journal of Hydrogen Energy*, vol. 35, no. 15, pp. 8136–8142, 2010.
- [14] R. W. J. Scott, O. M. Wilson, S. K. Oh, E. A. Kenik, and R. M. Crooks, "Bimetallic palladium—Gold dendrimer-encapsulated catalysts," *Journal of the American Chemical Society*, vol. 126, no. 47, pp. 15583–15591, 2004.
- [15] D. R. Rolison, "Catalytic nanoarchitectures—the importance of nothing and the unimportance of periodicity," *Science*, vol. 299, no. 5613, pp. 1698–1701, 2003.
- [16] Y. Zhao, X. Yang, J. Tian, F. Wang, and L. Zhan, "Methanol electro-oxidation on Ni@Pd core-shell nanoparticles supported on multi-walled carbon nanotubes in alkaline media," *International Journal of Hydrogen Energy*, vol. 35, no. 8, pp. 3249–3257, 2010.
- [17] N. Kristian and X. Wang, "Pt_{shell}-Au_{core}/C electrocatalyst with a controlled shell thickness and improved Pt utilization for fuel cell reactions," *Electrochemistry Communications*, vol. 10, no. 1, pp. 12–15, 2008.
- [18] K. C. Grabar, K. J. Allison, B. E. Baker et al., "Two-dimensional arrays of colloidal gold particles: a flexible approach to macroscopic metal surfaces," *Langmuir*, vol. 12, no. 10, pp. 2353–2361, 1996.
- [19] N. R. Jana, L. Gearheart, and C. J. Murphy, "Wet chemical synthesis of high aspect ratio cylindrical gold nanorods," *Journal of Physical Chemistry B*, vol. 105, no. 19, pp. 4065–4067, 2001.

- [20] A. Gole and C. J. Murphy, "Seed-mediated synthesis of gold nanorods: role of the size and nature of the seed," *Chemistry of Materials*, vol. 16, no. 19, pp. 3633–3640, 2004.
- [21] A. Henglein, "Preparation and optical absorption spectra of $\text{Au}_{\text{core}}\text{Pt}_{\text{shell}}$ and $\text{Pt}_{\text{core}}\text{Au}_{\text{shell}}$ colloidal nanoparticles in aqueous solution," *Journal of Physical Chemistry B*, vol. 104, no. 10, pp. 2201–2203, 2000.
- [22] W. Zhou and J. Y. Lee, "Highly active core-shell Au@Pd catalyst for formic acid electrooxidation," *Electrochemistry Communications*, vol. 9, no. 7, pp. 1725–1729, 2007.
- [23] J. W. Hu, Y. Zhang, J. F. Li et al., "Synthesis of Au@Pd core-shell nanoparticles with controllable size and their application in surface-enhanced Raman spectroscopy," *Chemical Physics Letters*, vol. 408, no. 4–6, pp. 354–359, 2005.
- [24] M. H. Atwan, C. L. B. Macdonald, D. O. Northwood, and E. L. Gyenge, "Colloidal Au and Au-alloy catalysts for direct borohydride fuel cells: electrocatalysis and fuel cell performance," *Journal of Power Sources*, vol. 158, no. 1, pp. 36–44, 2006.

Research Article

Use of Dendrimers during the Synthesis of Pt-Ru Electrocatalysts for PEM Fuel Cells: Effects on the Physical and Electrochemical Properties

J. C. Calderón,¹ L. Calvillo,² M. J. Lázaro,² and E. Pastor¹

¹ *Departamento de Química-Física, Facultad de Química, Universidad de La Laguna, Avenida Astrofísico Francisco Sánchez s/n, 38071 La Laguna (Tenerife), Spain*

² *Instituto de Carboquímica (CSIC), Miguel Luesma Castán 4, 50018 Zaragoza, Spain*

Correspondence should be addressed to E. Pastor, epastor@ull.es

Received 3 May 2011; Accepted 28 July 2011

Academic Editor: Maria E. Martins

Copyright © 2011 J. C. Calderón et al. This is an open access article distributed under the Creative Commons Attribution License, which permits unrestricted use, distribution, and reproduction in any medium, provided the original work is properly cited.

In this work, Pt-Ru catalysts were synthesized by a novel methodology which includes the use as encapsulating molecules of dendrimers of different generation: zero (DN-0), one (DN-1), two (DN-2), and three (DN-3). Synthesized catalysts were heat-treated at 350°C, and the effects of this treatment was established from the physical (X-ray dispersive energy (XDE) and X-ray diffraction (XRD)) and electrochemical characterization (cyclic voltammetry and chronoamperometry). Results showed that the heat-treatment benefits the catalytic properties of synthesized materials in terms of CO and methanol electrochemical oxidation. The curves for CO stripping were more defined for heat-treated catalysts, and methanol oxidation current densities were higher for these materials. These changes are principally explained from the removal of organic residues remaining on the surface of the Pt-Ru nanoparticles after the synthesis procedure. After the activation of the catalysts by heating at 350°C, the real importance of the use of these encapsulating molecules and the effect of the generation of the dendrimer become visible. From these results, it can be concluded that synthesized catalysts are good catalytic anodes for direct methanol fuel cells (DMFCs).

1. Introduction

Direct methanol fuel cells (DMFCs) are a promising power source for automotive and portable power applications. This versatility is related to ease in fuel handling, simple system design, high efficiency, and low emissions [1, 2]. Nevertheless, the use of DMFCs is limited by the reaction kinetics for methanol electro-oxidation on platinum, which possesses a slow rate and involves steps like methanol adsorption with their respective dissociation, water adsorption also with its activation, and CO oxidation as intermediate of this reaction [3]. In fact, the presence of CO and HCOO⁻ intermediates is determinant in slow reaction kinetics due to the strong adsorption of these species on Pt, blocking the electroactive sites. As an alternative for solving this problem, Pt-Ru alloys have been suggested [4, 5] because of their higher activity for methanol electro-oxidation, stability, and ability of Ru for providing OH_{ads} species, which are able to weaken and accelerate CO adsorption and oxidation [3].

These reasons motivate the implementation of novel Pt-Ru nanoparticles synthesis procedures, with controlled metal loading, Pt:Ru atomic proportions, particle size, and homogeneous dispersion on a determined support. Typical wet impregnation and incipient wetness methods do not allow controlling these properties [6]. An alternative is the use of dendrimers, which are three-dimensional and tree-like functional macromolecules, where branches are the specific sites for nucleation process of metal precursors [7]. Branches conform the so-called generations of a dendrimer; the first-generation dendrimer is constituted by a determined number of monomers linked to a central core. Subsequent union between other monomers and the extreme of the first linked monomers generates a second generation and thus, next generations are formed until steric hindrance inhibits formation of further shells [7]. Because of these structural characteristics, they were successfully used as a template for metal nanoparticles formation, providing five principal advantages [8]: (1) the possibility of obtaining well-defined

size and shape nanoparticles due to their uniform structure [9], (2) avoid agglomeration of nanoparticles by stabilization into the dendrimer structure [10], (3) protection towards passivation and enabling to catalytic activity by means of steric hindrance which surround the nanoparticles [11], (4) the selectivity towards access of small substrates to the encapsulated catalytic nanoparticles, controlled by the dendrimer branches, and (5) terminal amino groups of the molecule could be modified for controlling the solubility of dendrimer-nanoparticle composite, providing the possibility of linkage to others polymers [12].

Synthesis of DENs (dendrimer encapsulated nanoparticles) is widely reported in the literature [13–19], and this process usually initiates with the formation of intradendrimer metal clusters, then chemically reduced with excess of NaBH_4 . Changes in solution colour and UV-visible absorbance bands are the evidences for this cluster formation [20] even giving some clue about their size [21, 22]. In the case of dendrimers with noncomplexing functional groups, such as hydroxyl groups, nanoparticle formation is carried out into the dendrimer [23, 24]. However, dendrimer template formation of nanoparticles can be realized also in the external branches [23, 25], as is the case of amine-terminated poly(amidoamine) dendrimers, which could promote the formation of nanoparticles surrounded by complexation of metal ions with dendrimeric surface amine groups [26]. The control of the pH of the dendrimeric solution could prevent the formation of metal complexes on the dendrimer periphery, by protonation of the surface primary amine groups, which also be available to nucleate metallic nanoparticles [27].

In this work, Pt-Ru catalysts supported on carbon nanofibers were synthesized, by reduction with sodium borohydride, making use of amino-terminal dendrimers, with zero, one, two, and three generation. Heat treatment at 350°C was used in order to remove the encapsulating dendrimers. Physical characterization was carried out by means of EDX, XRD, and TEM, while electrochemical activity towards CO and methanol electrochemical oxidation was studied by cyclic voltammetry and chronoamperometry, comparing the effect of heat treatment in terms of metal loading, Pt:Ru proportion, particle size, and catalytic activity.

2. Experimental

2.1. Synthesis of Catalysts. Carbon nanofibers synthesized by catalytic thermal decomposition of methane were used as carbon support. For their synthesis, an Ni:Cu:Al catalyst with a weight proportion 78:6:16 was employed. After the activation of this catalyst growth of CNFs was carried out passing a methane flux at 700°C for 10 h on the catalysts. Obtained carbon nanofibers were treated with an HNO_3 - H_2SO_4 1:1 (v/v) mixture for 0.5 h at room temperature. For the synthesis of catalysts, different generation PAMAM dendrimers (20% wt in methanol, Aldrich) were dissolved in ultrapure water adding the appropriate volume to achieve a $2.0\ \mu\text{M}$ concentration. Solutions were vigorously magnetic stirred during 30 min, and then, metal precursors solution (H_2PtCl_6 , 8% wt solution, Aldrich; and RuCl_3 99.999%,

Aldrich) was slowly added to the dendrimer one, maintaining the agitation during the addition and after for 3 days. Then, 20 mL of reducing agent solution (NaBH_4 , 26.4 mM in NaOH 7.0 M) were slowly added generating a dark colour because of the formation of Pt-Ru nanoparticles. After 24 h on the magnetic stirrer, carbon nanofibers were added to the reaction mixture in the presence of ultrasound agitation. The reaction mixture was maintained under stirring for 2 days, and after being filtered, it was washed with ultrapure water and dried at 60°C during 2 h. Nomenclature used for these catalysts is PtRu/CNF-DN-X, being X the generation of the dendrimer used during the synthesis. Finally, catalysts were heat treated at 350°C in a furnace for 30 min. In this case, the nomenclature was PtRu/CNF-DN-X TT, with X meaning as before.

2.2. EDX, XRD, and TEM Characterization. Determination of metal content and Pt-Ru atomic ratios for the synthesized materials were made by energy dispersive X-ray (EDX) analysis, using a scanning electron microscope (LEO Mod. 440) at 20 keV, with a Si detector and a Be window. X-ray diffraction (XRD) patterns were made by means of a universal diffractometer Panalytical X'Pert, operating with $\text{Cu-K}\alpha$ radiation, generated at 40 kV and 30 mA. Scan rate was $3^\circ\ \text{min}^{-1}$ with 2θ values between 10 and 100° . Scherrer's equation was used to calculate the metal crystallite size from XRD, using the dimensions of (220) peak around $2\theta = 70^\circ$.

2.3. Electrochemical Characterization. Electrochemical activity of Pt-Ru catalysts towards CO and methanol was evaluated by cyclic voltammetry and chronoamperometry. It was compared to that of the commercial PtRu/C catalyst from E-TEK. An electrochemical thermostated cell was used with a glassy carbon disk as working electrode, a glassy carbon bar as counter electrode and a reversible hydrogen electrode (RHE), placed inside a Luggin capillary as reference electrode. All potentials in the text are referred to the RHE electrode. A catalyst ink was prepared by mixing 2 mg of the catalyst, $15\ \mu\text{L}$ of Nafion (5 wt.%, Aldrich), and $500\ \mu\text{L}$ of ultrapure water. An aliquot of this dispersion was deposited onto the glassy carbon disk. 0.5 M H_2SO_4 (95–97%, Merck) and 2.0 M methanol (98%, Merck) solutions were used in these experiments. CO reactivity on the different catalysts was evaluated by bubbling it into the electrochemical cell, during 10 minutes, producing an adsorbed CO monolayer on the deposited catalyst. Then, nitrogen (MicroGen N_2 , GasLab) was bubbled during 10 minutes to remove CO from the solution. Finally, cyclic voltammetric and chronoamperometric curves were recorded using an Electrochemistry Instrument $\mu\text{AUTOLAB III}$ modular equipment.

3. Results and Discussion

3.1. Physical Characterization of the Catalysts. EDX analysis was used for determining the metal content and Pt:Ru atomic ratio, and the results are given in Table 1. All catalysts present similar metal content and Pt:Ru atomic ratio, approx. 20% wt. and 1:1, respectively. These values were comparable

TABLE 1: Composition and crystallite sizes for Pt-Ru catalysts.

Catalyst	Pt-Ru (EDX)	Metal loading (% wt.)	Crystallite size (nm)
PtRu/CNF-DN-0	58–42	12	3.3
PtRu/CNF-DN-0 TT	49–51	18	4.1
PtRu/CNF-DN-1	59–41	20	3.8
PtRu/CNF-DN-1 TT	52–48	17	3.6
PtRu/CNF-DN-2	44–56	20	3.0
PtRu/CNF-DN-2 TT	40–60	19	3.8
PtRu/CNF-DN-3	47–53	19	3.0
PtRu/CNF-DN-3 TT	41–59	21	2.9
PtRu/C E-TEK	45–55	20	4.4

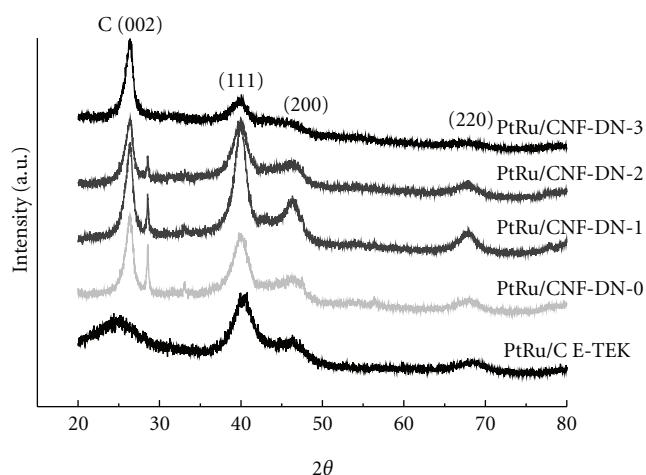


FIGURE 1: XRD diffractograms for the untreated Pt-Ru catalysts.

to those of the commercial Pt-Ru/C E-TEK catalyst and close to the nominal ones. After the heat treatment, metal loading and compositions remain similar assuming the experimental error, with the exception of the metal loading in the DN-0 material which increases from 12 to 18%. This result can be explained by an important loss of organics during the heat treatment, which seems to be much important with this dendrimer. Concerning the Pt:Ru atomic proportion, although the changes are small, a trend to increase the Ru content after heating is apparent for all catalysts, suggesting that the treatment can induce modifications in the catalysts nature, as an increase in the oxidation state of ruthenium forming ruthenium oxides [28] and, therefore, promoting changes in the original composition.

XRD patterns of the nonheat treated and heat-treated catalysts (Figures 1 and 2, resp.) display the characteristic peaks, (111), (200), and (220), of the face centred cubic (fcc) structure of Pt and also a diffraction peak around 24.5° for Pt-Ru/C E-TEK and 26.5° for PtRu/CNF. This peak corresponds to the (002) reflection of graphite basal planes and is attributed to the catalyst support. It is remarkable the appearance of new peaks at 35 and 55 2θ degrees in the heat-treated catalysts (Figure 2), indicating the formation of ruthenium oxides [29] and the graphitization of carbon

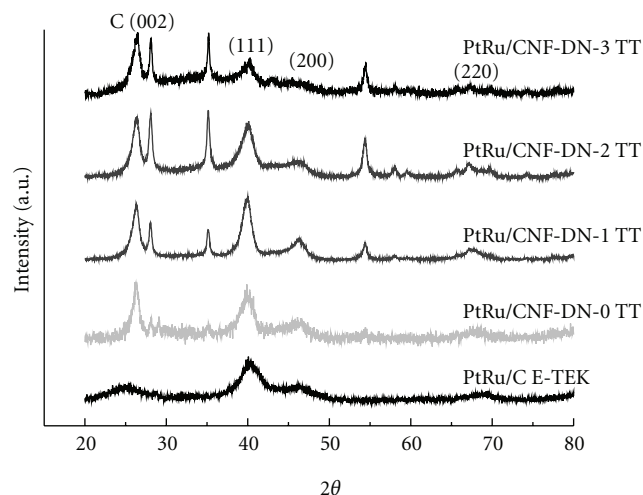


FIGURE 2: XRD diffractograms for the synthesized Pt-Ru catalysts submitted to heat treatment at 350°C.

support with the corresponding (004) face present at the hexagonal graphite structure [30], respectively. Moreover, metal average crystallite sizes were determined with the (220) reflection peak dimensions (Table 1). Debye-Scherrer equation was used for calculating the average crystallite size of catalysts, obtaining values between 2.9 and 4.1 nm, being PtRu/CNF-DN-3 TT the catalysts with the smallest crystallite size (2.9 nm). All values were smaller than that for the commercial catalyst, and the largest size was obtained for the PtRu/CNF-DN-0 TT material (4.4 nm). The latter result can be attributed to the low encapsulating effect of the zero generation dendrimer, considering that low generation dendrimers have an open and flat structure, losing their capacity to confine the nanoparticles [31]. This fact is verified with the small crystallite sizes obtained for synthesized catalysts using two and three generation dendrimers.

3.2. Electrochemical Characterization. Reactivity towards CO (Figures 3–5) and methanol (Figure 6) was evaluated by means of cyclic voltammetry, both for the commercial catalyst PtRu/C E-TEK and the synthesized catalysts. Current density values were normalized by the Pt loading of each electrode. CO stripping curves for heat-treated materials (Figure 5) develop a narrower oxidation peaks with a well-defined peak potential compared with the untreated catalysts (Figure 4), as well as its current densities were more similar than those of the untreated catalysts. Possibly, in the presence of dendrimers from the synthesis procedure at the surface of n , the untreated materials diminishes the reactivity towards CO because of a passivating effect on catalytic sites. According to this assumption, the CVs for the catalysts in the base electrolyte change drastically after heating, as can be seen in Figures 4 and 5, as a consequence of the elimination of the organic residues. Results in Figure 5 are in agreement with that reported in the literature for well-cleaned Pt-Ru alloys used as catalysts for CO electrochemical oxidation [32]. Then, it is proved that the treatment at 350°C produces PtRu nanoparticles activation, with appropriate

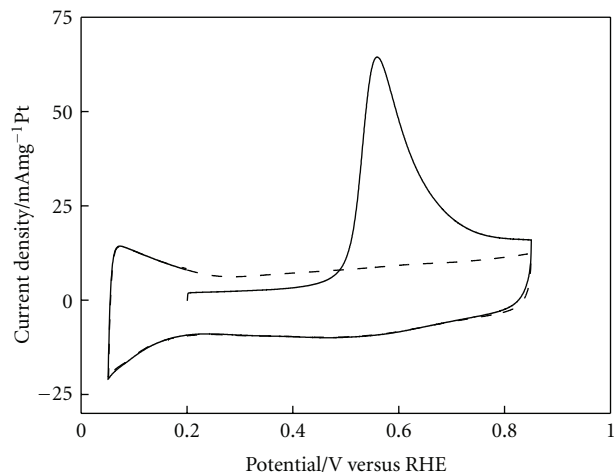


FIGURE 3: Cyclic voltammograms for CO oxidation at room temperature on commercial catalysts PtRu/C E-TEK. Full line: first scan. Dashed line: second scan. Scan rate: 20 mVs^{-1} . Supporting electrolyte: $0.5 \text{ M H}_2\text{SO}_4$. CO adsorption potential: 0.2 V versus RHE.

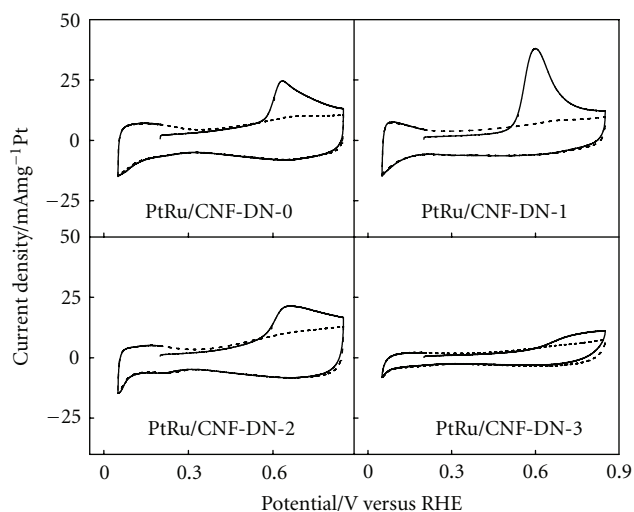


FIGURE 4: Cyclic voltammograms for CO oxidation at room temperature on untreated synthesized catalysts. Full line: first scan. Dashed line: second scan. Scan rate: 20 mVs^{-1} . Supporting electrolyte: $0.5 \text{ M H}_2\text{SO}_4$. CO adsorption potential: 0.2 V versus RHE.

surface activity towards CO electrooxidation, even better than the commercial PtRu/C E-TEK (which shows a broader curve shifted to more positive potentials, Figure 3).

Methanol electrochemical oxidation (Figure 6) presents significant differences between the untreated catalysts and those heat-treated catalysts. For the former (Figure 6(a)), commercial catalyst PtRu/C E-TEK shows a great activity with respect to the synthesized catalyst. Possibly, dendrimers kept in the material, passivating metal nanoparticles and inhibiting their catalytic activity towards methanol. However, the effect of dendrimer generation is clearly observed: the higher the generation of the dendrimer, lower

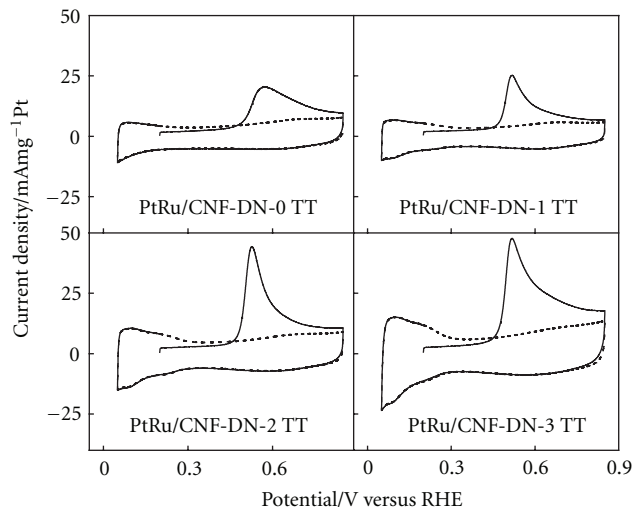


FIGURE 5: Cyclic voltammograms for CO oxidation at room temperature on the heat-treated synthesized catalysts. Full line: first scan. Dashed line: second scan. Scan rate: 20 mVs^{-1} . Supporting electrolyte: $0.5 \text{ M H}_2\text{SO}_4$. CO adsorption potential: 0.2 V versus RHE.

the the methanol oxidation current densities recorded. The explanation is conducted through the dendrimer size: PtRu/CNF-DN-0 displays the better performance probably because of the relatively small size of zero generation dendrimer molecules, which did not produce a strong surface passivation. Opposite, DN-3 is the biggest molecule and, consequently, generates the highest passivation effect.

Nevertheless, heat treatment strongly promotes the methanol electrochemical oxidation on those materials prepared with dendrimers corresponding to generation higher than zero (Figure 6(b)). In this case, the catalyst synthesized in the presence of DN-0 (PtRu/CNF-DN-0 TT) shows the lowest current densities, and the activities increase with the generation of the dendrimer: PtRu/CNF-DN-3 TT displays the highest methanol oxidation current densities, followed by PtRu/CNF-DN-2 TT, PtRu/C E-TEK, PtRu/CNF-DN-1 TT, and finally, PtRu/CNF-DN-0 TT. According to Table 1, the main difference between the PtRu/CNF-DN-3 TT and the other catalysts is the small particle size, and therefore, it seems to be the main parameter conditioning the current densities attained. This fact leads us to conclude the role played by dendrimer generation. Thus, it seems that the size of dendrimer is a crucial factor for obtaining adequate crystallite sizes. However, an effect associated to changes in the distribution of the crystallographic planes in the nanoparticle induced by the dimension of the dendrimer cannot be discarded.

In order to establish the steady state performance of catalysts for methanol electrooxidation, chronoamperometry was carried out. Figure 7 displays the potentiostatic current density curves as a function of time for the heat-treated Pt-Ru materials at 0.55 V , as a typical working potential in DMFCs. Current density values are in the same range obtained in Figure 6(b). The same trend established from the

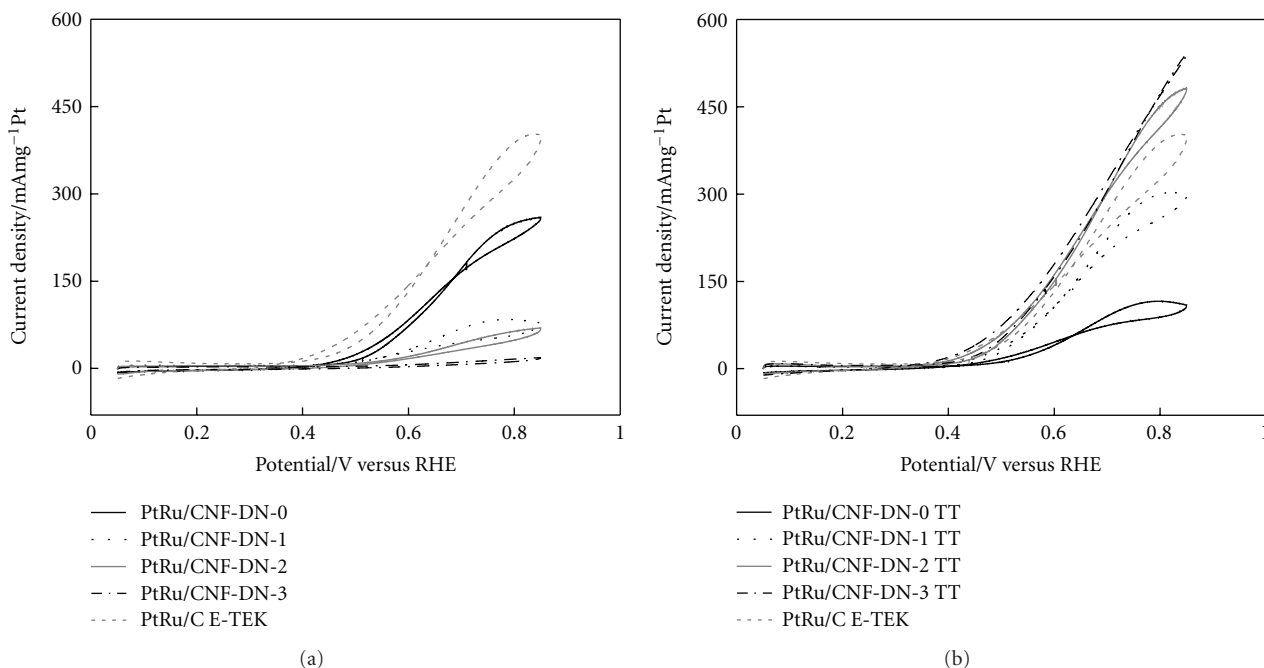


FIGURE 6: Cyclic voltammograms for methanol oxidation at room temperature on Pt-Ru synthesized catalysts. (a) Untreated catalysts (b) Heat-treated catalysts. Scan rate: 20 mVs $^{-1}$. Supporting electrolyte: 0.5 M H $_2$ SO $_4$. Methanol concentration: 2.0 M.

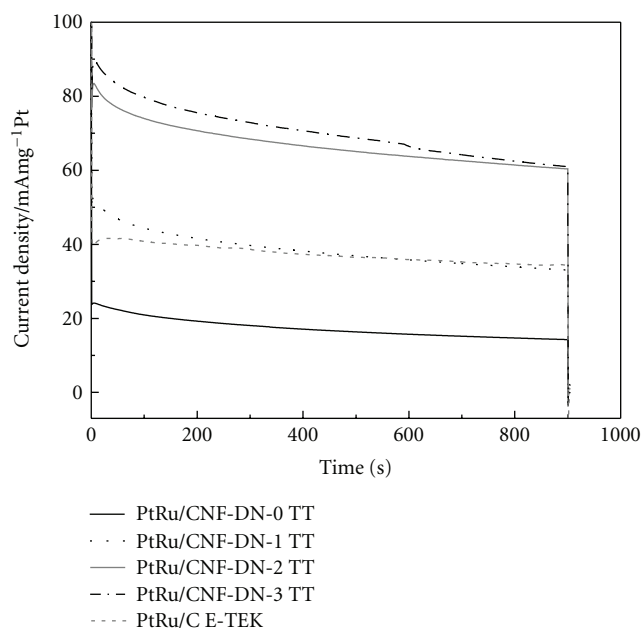


FIGURE 7: Current density versus time curves at room temperature for methanol oxidation on Pt-Ru synthesized catalysts. Supporting electrolyte: 0.5 M H $_2$ SO $_4$. Methanol concentration: 2.0 M. Applied potentials: 0.55 V.

CVs is also observed in Figure 7: again, PtRu/CNF-DN-3 TT and PtRu/CNF-DN-2 TT show the highest stationary current densities after 900 s at room temperature, whereas the lowest current densities correspond to PtRu/CNF-DN-0 TT.

These results confirm that dendrimer synthesis of Pt-Ru nanoparticles with an appropriate heat treatment allows to prepare catalysts with better performance than commercial ones.

4. Conclusions

Pt-Ru catalysts supported on carbon nanofibers have been synthesized using dendrimers of zero, one, two, and three generation. All prepared materials displayed a Pt : Ru ratio of 1 : 1 and metal loading close to 20%. These properties were near to those determined for the commercial catalyst PtRu/C E-TEK used for comparison. Crystallite size varies between 2.9 and 4.1 nm for the prepared materials (4.4 nm for the commercial one).

A heat treatment at 350°C was performed with all synthesized catalysts trying to activate the nanoparticles surface. Success of heat treatment was observed in the electrochemical experiments. Thus, CO stripping curves display well-defined peaks for heat-treated catalysts, whereas untreated materials describe broader curves with less-defined CO oxidation peak potentials. Moreover, the activity of PtRu/CNF-DN-3 TT and PtRu/CNF-DN-2 TT towards methanol electrooxidation was drastically increased after the procedure, as demonstrated in both cyclic voltammetric and chronoamperometric experiments. In fact, better performance than commercial PtRu/C E-TEK was obtained for these activated materials. Then, it is concluded that dendrimer synthesis followed by temperature activation can be used for the preparation of highly active anodes for direct methanol fuel cells.

Acknowledgments

This work was carried out with the help of Project MICINN (no. MAT2008-06631-C03-01 y -02) of the Spanish Ministry of Science and Technology. Juan Carlos Calderón is indebted to the Alβan Program for the predoctoral fellowship no. E07D403742CO.

References

- [1] H. Liu, C. Song, L. Zhang, J. Zhang, H. Wang, and D. P. Wilkinson, "A review of anode catalysis in the direct methanol fuel cell," *Journal of Power Sources*, vol. 155, no. 2, pp. 95–110, 2006.
- [2] A. H. C. Sirk, J. M. Hill, S. K. Y. Kung, and V. I. Birss, "Effect of redox state of PtRu electrocatalysts on methanol oxidation activity," *Journal of Physical Chemistry B*, vol. 108, no. 2, pp. 689–695, 2004.
- [3] M. Watanabe and S. Motoo, "Electrocatalysis by ad-atoms part II. Enhancement of the oxidation of methanol on platinum by ruthenium ad-atoms," *Journal of Electroanalytical Chemistry*, vol. 60, no. 3, pp. 267–273, 1975.
- [4] H. A. Gasteiger, N. Marković, P. N. Ross Jr., and E. J. Cairns, "Methanol electrooxidation on well-characterized platinum-ruthenium bulk alloys," *Journal of Physical Chemistry*, vol. 97, no. 46, pp. 12020–12029, 1993.
- [5] P. K. Shen and A. C. C. Tseung, "Anodic oxidation of methanol on Pt/WO₃ in acidic media," *Journal of the Electrochemical Society*, vol. 141, no. 11, pp. 3082–3089, 1994.
- [6] Y. Gu, G. Wu, X. F. Hu et al., "PAMAM-stabilized Pt-Ru nanoparticles for methanol electro-oxidation," *Journal of Power Sources*, vol. 195, no. 2, pp. 425–434, 2010.
- [7] J. M. J. Fréchet, "Functional polymers and dendrimers: reactivity, molecular architecture, and interfacial energy," *Science*, vol. 263, no. 5154, pp. 1710–1714, 1994.
- [8] R. M. Crooks, M. Zhao, L. Sun, V. Chechik, and L. K. Yeung, "Dendrimer-encapsulated metal nanoparticles: synthesis, characterization, and applications to catalysis," *Accounts of Chemical Research*, vol. 34, no. 3, pp. 181–190, 2001.
- [9] M. Zhao, L. Sun, and R. M. Crooks, "Preparation of Cu nanoclusters within dendrimer templates," *Journal of the American Chemical Society*, vol. 120, pp. 4877–4878, 1998.
- [10] M. Zhao and R. M. Crooks, "Homogeneous hydrogenation catalysis with monodisperse, dendrimer-encapsulated Pd and Pt nanoparticles," *Angewandte Chemie—International Edition*, vol. 38, no. 3, pp. 364–366, 1999.
- [11] V. Chechik, M. Zhao, and R. M. Crooks, "Self-assembled inverted micelles prepared from a dendrimer template: phase transfer of encapsulated guests," *Journal of the American Chemical Society*, vol. 121, no. 20, pp. 4910–4911, 1999.
- [12] H. Tokuhisa, M. Zhao, L. A. Baker et al., "Preparation and characterization of dendrimer monolayers and dendrimer—alkanethiol mixed monolayers adsorbed to gold," *Journal of the American Chemical Society*, vol. 120, no. 18, pp. 4492–4501, 1998.
- [13] H. Lang, R. A. May, B. L. Iversen, and B. D. Chandler, "Dendrimer-encapsulated nanoparticle precursors to supported platinum catalysts," *Journal of the American Chemical Society*, vol. 125, no. 48, pp. 14832–14836, 2003.
- [14] H. Lang, R. A. May, B. L. Iversen, and B. D. Chandler, in *Catalysis of Organic Reactions*, pp. 243–250, Taylor & Francis Group/CRC Press, Boca Raton, Fla, USA, 2005.
- [15] A. Singh and B. D. Chandler, "Low-temperature activation conditions for PAMAM dendrimer templated Pt nanoparticles," *Langmuir*, vol. 21, no. 23, pp. 10776–10782, 2005.
- [16] L. W. Beakley, S. E. Yost, R. Cheng, and B. D. Chandler, "Nanocomposite catalysts: dendrimer encapsulated nanoparticles immobilized in sol-gel silica," *Applied Catalysis A*, vol. 292, no. 1-2, pp. 124–129, 2005.
- [17] H. Lang, S. Maldonado, K. J. Stevenson, and B. D. Chandler, "Synthesis and characterization of dendrimer templated supported bimetallic Pt-Au nanoparticles," *Journal of the American Chemical Society*, vol. 126, no. 40, pp. 12949–12956, 2004.
- [18] H. Wu, Z. Liu, X. Wang, B. Zhao, J. Zhang, and C. Li, "Preparation of hollow capsule-stabilized gold nanoparticles through the encapsulation of the dendrimer," *Journal of Colloid and Interface Science*, vol. 302, no. 1, pp. 142–148, 2006.
- [19] F. N. Crespilho, F. Huguenin, V. Zucolotto, P. Olivi, F. C. Nart, and O. N. Oliveira Jr., "Dendrimers as nanoreactors to produce platinum nanoparticles embedded in layer-by-layer films for methanol-tolerant cathodes," *Electrochemistry Communications*, vol. 8, no. 2, pp. 348–352, 2006.
- [20] U. Kreibitz and M. Vollmer, *Optical Properties of Metal Clusters*, Springer, Berlin, Germany, 1995.
- [21] A. C. Curtis, D. G. Duff, P. P. Edwards et al., "A morphology-selective copper organosol," *Angewandte Chemie—International Edition*, vol. 27, pp. 1530–1533, 1988.
- [22] I. Lisiecki and M. P. Pileni, "Synthesis of copper metallic clusters using reverse micelles as microreactors," *Journal of the American Chemical Society*, vol. 115, no. 10, pp. 3887–3896, 1993.
- [23] Y. M. Chung and H. K. Rhee, "Synthesis and catalytic applications of dendrimer-templated bimetallic nanoparticles," *Catalysis Surveys from Asia*, vol. 8, no. 3, pp. 211–223, 2004.
- [24] R. W. J. Scott, A. K. Datye, and R. M. Crooks, "Bimetallic palladium-platinum dendrimer-encapsulated catalysts," *Journal of the American Chemical Society*, vol. 125, no. 13, pp. 3708–3709, 2003.
- [25] W. Zhang, L. Li, Y. Du, X. Wang, and P. Yang, "Gold/platinum bimetallic core/shell nanoparticles stabilized by a Fréchet-type dendrimer: preparation and catalytic hydrogenations of phenylaldehydes and nitrobenzenes," *Catalysis Letters*, vol. 127, no. 3-4, pp. 429–436, 2009.
- [26] Y. Niu, L. Sun, and R. M. Crooks, "Determination of the intrinsic proton binding constants for poly(amidoamine) dendrimers via potentiometric pH titration," *Macromolecules*, vol. 36, no. 15, pp. 5725–5731, 2003.
- [27] H. Ye, R. W. J. Scott, and R. M. Crooks, "Synthesis, characterization, and surface immobilization of platinum and palladium nanoparticles encapsulated within amine-terminated poly(amidoamine) dendrimers," *Langmuir*, vol. 20, no. 7, pp. 2915–2920, 2004.
- [28] X. Li, J. Liu, Q. Huang, W. Vogel, D. L. Akins, and H. Yang, "Effect of heat treatment on stability of gold particle modified carbon supported Pt-Ru anode catalysts for a direct methanol fuel cell," *Electrochimica Acta*, vol. 56, no. 1, pp. 278–284, 2010.
- [29] E. S. Steigerwalt, G. A. Deluga, D. E. Cliffl, and C. M. Lukehart, "A Pt-Ru/graphitic carbon nanofiber nanocomposite exhibiting high relative performance as a direct-methanol fuel cell anode catalyst," *Journal of Physical Chemistry B*, vol. 105, no. 34, pp. 8097–8101, 2001.
- [30] K. T. Jeng, C. C. Chien, N. Y. Hsu et al., "Performance of direct methanol fuel cell using carbon nanotube-supported Pt-Ru anode catalyst with controlled composition," *Journal of Power Sources*, vol. 160, no. 1, pp. 97–104, 2006.

- [31] L. Jin, S. P. Yang, Q. W. Tian, H. X. Wu, and Y. J. Cai, "Preparation and characterization of copper metal nanoparticles using dendrimers as protectively colloids," *Materials Chemistry and Physics*, vol. 112, no. 3, pp. 977–983, 2008.
- [32] H. A. Gasteiger, N. Marković, P. N. Ross Jr., and E. J. Cairns, "CO electrooxidation on well-characterized Pt-Ru alloys," *Journal of Physical Chemistry*, vol. 98, no. 2, pp. 617–625, 1994.

Research Article

Investigation of IrO₂/Pt Electrocatalysts in Unitized Regenerative Fuel Cells

V. Baglio,¹ C. D'Urso,¹ A. Di Blasi,¹ R. Ornelas,² L. G. Arriaga,³ V. Antonucci,¹ and A. S. Arico¹

¹ CNR-Istituto di Tecnologie Avanzate per l'Energia "Nicola Giordano" (ITAE), Via Salita S. Lucia sopra Contesse 5, 98126 Messina, Italy

² Tozzi Apparecchiature Elettriche S.p.A., Via Zuccherificio, 10-48010 Mezzano, Italy

³ Centro de Investigación y Desarrollo Tecnológico en Electroquímica S.C., 76700 Querétaro Sanfandila, QRO, Mexico

Correspondence should be addressed to V. Baglio, baglio@itae.cnr.it

Received 4 April 2011; Revised 16 May 2011; Accepted 8 June 2011

Academic Editor: Elena Pastor Tejera

Copyright © 2011 V. Baglio et al. This is an open access article distributed under the Creative Commons Attribution License, which permits unrestricted use, distribution, and reproduction in any medium, provided the original work is properly cited.

IrO₂/Pt catalysts (at different concentrations) were synthesized by incipient wetness technique and characterized by XRD, XRF, and SEM. Water electrolysis/fuel cell performances were evaluated in a 5 cm² single cell under Unitized Regenerative Fuel Cell (URFC) configuration. The IrO₂/Pt composition of 14/86 showed the highest performance for water electrolysis and the lowest one as fuel cell. It is derived that for fuel cell operation an excess of Pt favours the oxygen reduction process whereas IrO₂ promotes oxygen evolution. From the present results, it appears that the diffusion characteristics and the reaction rate in fuel cell mode are significantly lower than in the electrolyser mode. This requires the enhancement of the gas diffusion properties of the electrodes and the catalytic properties for cathode operation in fuel cells.

1. Introduction

A Unitized Regenerative Fuel Cell (URFC) is an energy storage system useful to be connected to renewable sources such as solar energy or wind energy [1]. Such a system consists of a water electrolyser and a fuel cell combined in one stack, allowing a significant cost and volume reduction compared to the two devices separated. During electrolysis mode, water is electrolyzed to hydrogen and oxygen which are used to produce electrical energy in the subsequent fuel cell mode. Compared with conventional secondary batteries, the URFC has the advantage of long-term energy storage, being free of self-discharge, and higher energy density [2, 3]. Instead, compared with the conventional Regenerative Fuel Cell (RFC), which usually consists of separate fuel cell and electrolyser, the URFC is a simpler and more compact system because it uses only one electrochemical cell [4, 5]. Nevertheless, the design of an electrode to be used in an electrolyser is inherently different than that of a fuel cell electrode [6]. For example, for the oxygen electrode in a polymer electrolyte fuel cell, the Gas Diffusion Layer (GDL) is usually a highly hydrophobized carbon paper or carbon

cloth. However, they cannot be used as the GDL of a URFC for the following two reasons: (i) the carbon material tends to corrode at high potential on the oxygen electrode side during the water electrolysis operation and (ii) GDLs have to achieve an appropriate balance between the hydrophobic and hydrophilic properties for both the fuel cell and water electrolysis operation [7]. While the electrode for water electrolyser is generally designed to be flooded or partially flooded, the fuel cell must repel water. From these considerations it arises clearly that the URFC is not the simple linear combination of electrodes used in fuel cells with those used in electrolysis cells. For instance, the hydrogen electrode must not only contribute to the hydrogen evolution reaction but also must do it in the opposite direction. Nevertheless, the most critical point is the oxygen electrode, which displays the greater difficulties for its design [8]. To date, bifunctional electrocatalysts for oxygen redox reaction of URFCs include Pt-Ir [9], Pt-Ru-Ir [10], Pt-IrO₂ [11–15], and Pt-IrO₂-RuO₂ [16, 17], among which IrO₂ and RuO₂ are mainly prepared by using Adams fusion method [18]. Most of the above described bifunctional oxygen electrode catalysts are obtained by mixing an efficient electrocatalyst for oxygen

reduction (Pt black) and an efficient electrocatalyst for oxygen evolution (Ir or IrO₂ or IrO₂-RuO₂), which may result in poor combination between Pt black and Ir or IrO₂ or IrO₂-RuO₂ and thus lower bifunctional performance of oxygen electrode electrocatalysts. In this work, our approach was the use of an impregnation method to support IrO₂ onto Pt surface in order to reduce the amount of metal oxide maintaining good performance in electrolysis mode. Moreover, a hydrophobized Ti grid was used [19, 20] as diffusion layer, instead of the carbon-based GDL commonly used in fuel cells, at the oxygen electrode compartment in order to have a stable support [21, 22] and suitable reactants distribution/products removal.

2. Experimental

2.1. Preparation of IrO₂/Pt Electrocatalysts. The preparation of IrO₂/Pt was carried out by incipient wetness technique, which consists in the impregnation of commercial IrO₂ (Spectrum) onto a commercial Pt black (Johnson Matthey). The electrocatalysts were prepared at three different concentrations (weight ratios of 7/93, 11/89, and 14/86). Such compositions were precisely determined by X-ray fluorescence (XRF) analyses.

2.2. Physicochemical Characterization. The powders were characterized by X-Ray Diffraction (XRD), X-Ray Fluorescence (XRF), and Scanning Electron Microscopy (SEM). X-ray diffraction powder (XRD) patterns for these catalysts were obtained on a Philips X'Pert X-ray diffractometer using Cu K α -source operating at 40 kV and 30 mA. The peak profiles of the (2 2 0) reflection in the face-centered-cubic (fcc) structure were obtained by using the Marquardt algorithm, and it was used to calculate the crystallite size by the Debye-Scherrer equation due to the fact that there are not convolution of other peaks, as it may occur with the (1 1 1), (2 0 0), and (3 1 1) reflections. Instrumental broadening was determined by using a standard platinum sample. Catalysts were placed on a silicon substrate for XRD analysis. The diffraction patterns were fitted to JCPDS (Joint Committee on Powder Diffraction Standards) and crystal size distribution calculated using LBA (line broadening analysis). XRF analysis of the catalysts was carried out by a Bruker AXS S4 Explorer spectrometer operating at a power of 1 kW and equipped with a Rh X-ray source, a LiF crystal analyzer, and a 0.12° divergence collimator. SEM analysis of the catalysts was carried out by an FEI XL-30 Field Emission Electron Gun instrument. SEM images showed both secondary and backscattering electrons.

2.3. Electrodes and MEA Preparation. A commercial 30% Pt/Vulcan XC-72 (E-TEK-PEMEAS, Boston, USA) was used as the catalyst for the H₂ evolution reaction (electrolyser) and for H₂ reduction process (fuel cell). The electrode was prepared by directly mixing in an ultrasonic bath a suspension of Nafion ionomer in water with the Pt/C catalyst powder (catalyst/dry ionomer = 2/1 wt.); the obtained paste was spread on carbon cloth backings (GDL ELAT from E-TEK).

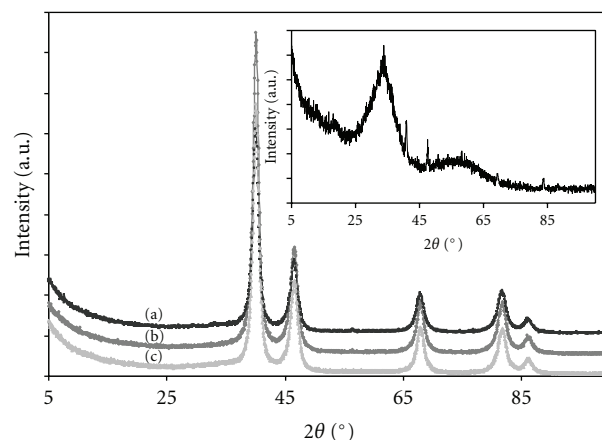


FIGURE 1: XRD patterns of (a) 14/86, (b) 11/89, (c) 7/93 IrO₂/Pt catalysts, and (inset) commercial IrO₂.

For membrane-electrode assembly (MEA) fabrication, the oxygen electrode was prepared by hot-spray technique, depositing the IrO₂/Pt catalyst directly onto Nafion 117 membrane (Ion Power). A slurry composed of 67 wt.% catalyst and 33 wt.% Nafion solution (5 wt.% Ion Power) in deionised water and anhydrous ethylic alcohol (Carlo Erba) was prepared by mixing under ultrasounds. This slurry was deposited onto one face of the membrane by using a spray technique. The catalyst loading was about 6 mg·cm⁻² for IrO₂/Pt and 1 mg·cm⁻² for 30% Pt/Vulcan XC-72 (E-TEK). Nafion 117 was used as the solid polymer electrolyte. Complete MEAs were formed directly in the cell housing by tightening at 9 N·m using a dynamometric wrench. A hydrophobised Ti grid (Franco Corradi, Italy) backing layer was used at the oxygen compartment [23, 24].

2.4. Electrochemical Characterization. We have evaluated water electrolysis/fuel cell performance using a single-cell test fixture with a geometric area of 5 cm². During fuel cell operation, the cell temperature was controlled at 80°C and a back pressure of 2 atm, for H₂ and O₂ reactant gases, was applied. Both gases were fully humidified. During water electrolysis operation, the cell was controlled at 80°C under atmospheric pressure and the water tank temperature was 85°C. The polarization curves were recorded by using an Autolab PGSTAT 302 Potentiostat/Galvanostat (Metrohm).

3. Results and Discussion

XRD analyses were carried out on the prepared catalysts (Figure 1) and compared to commercial IrO₂ (Figure 1, inset). The XRD pattern of IrO₂ shows a prevailing amorphous structure and some crystalline peaks associated to metallic Ir (Figure 1, inset), whereas the bifunctional catalysts showed the face-centered-cubic (fcc) structure typical of Pt due to the large amount of this metal compared to IrO₂ (which is, in any case, in an amorphous phase). Three different compositions were prepared and identified by XRF analysis (Table 1).

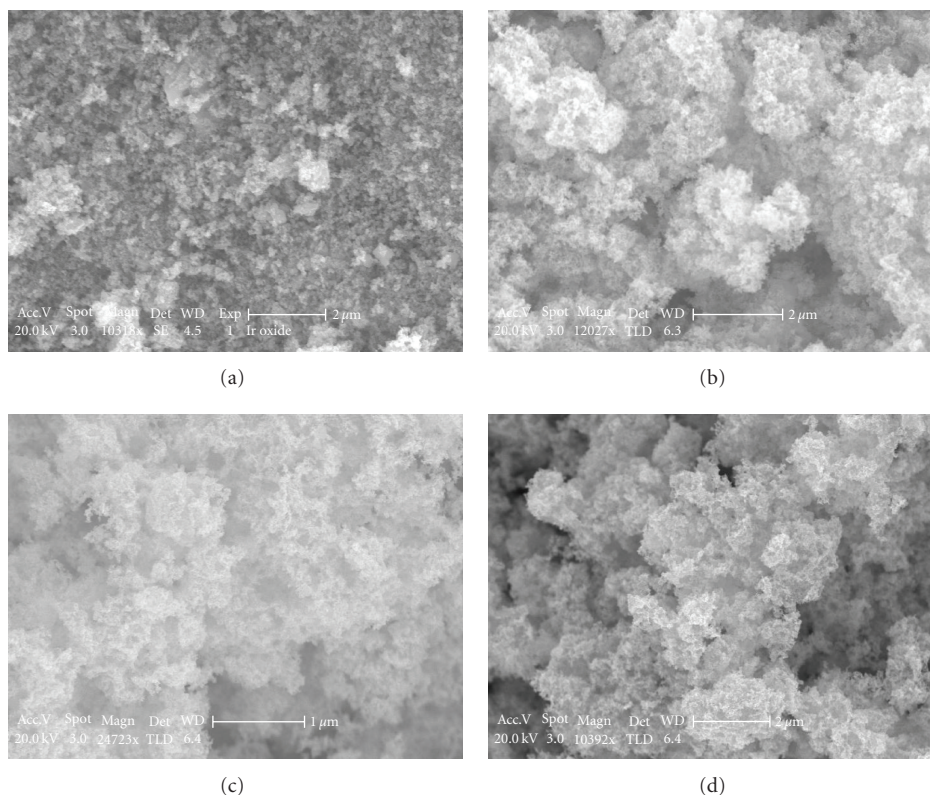


FIGURE 2: Scanning electronic micrographs of (a) amorphous IrO_2 , (b) 7/93, (c) 11/89, and (d) 14/86 IrO_2/Pt catalysts.

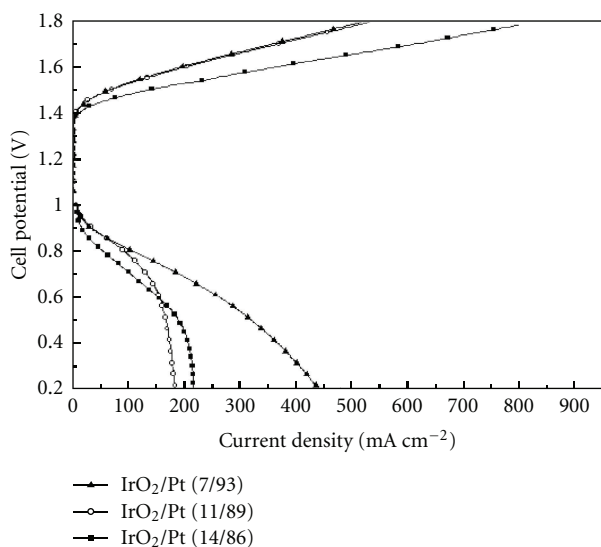


FIGURE 3: Cell potential versus current density curves for MEAs based on IrO_2/Pt catalysts at different compositions (7/93, 11/89, and 14/86) under URFC conditions.

The crystallite size of Pt in the bifunctional catalysts was estimated from the broadening of (220) reflections by the Scherrer equation. The values were about 6.5 ± 0.2 nm for all samples (Table 1).

TABLE 1: Composition and crystallite size of the catalysts.

Catalyst	Crystallite Size nm	Pt (wt. %)	IrO_2 (wt. %)
(a)	6.5	93	7
(b)	6.5	89	11
(c)	6.7	86	14

Figure 2 shows scanning electron micrographs of IrO_2/Pt at different compositions (7/93, 11/89, 14/86) and bare IrO_2 . Amorphous IrO_2 (Figure 2(a)) showed agglomerates of about 50–100 nm. The BET surface area for this IrO_2 catalyst is quite low, about $23 \text{ m}^2 \text{ g}^{-1}$ with the occurrence of micropores as confirmed by the porosity measurements reported in [25] whereas an adequate porous structure was observed for IrO_2/Pt bimetallic catalysts. All bimetallic catalysts show similar structure due to the fact that they are composed of the same materials with a larger presence of Pt [26].

The cell potential versus current density (calculated using the geometrical area of 5 cm^2) curves for MEAs based on the three compositions of IrO_2/Pt (7/93, 11/89, 14/86) under URFC conditions are shown in Figure 3. The IrO_2/Pt composition of 14/86 has the highest performance for water electrolysis and the lowest performance as fuel cell. It is derived that for fuel cell operation an excess of Pt favours the oxygen reduction process whereas IrO_2 promotes oxygen evolution. In fact, the results achieved in this work in electrolysis mode are similar to those obtained by using a pure

IrO₂ in a PEM electrolyser [22, 23]. This is probably due to the good dispersion of this metal oxide onto the Pt support. Thus, the utilization of IrO₂ is maximized. However, the presence of a larger amount of IrO₂ produces better results in the electrolysis process. Thus, it appears necessary to optimize the relative content of the two materials in order to have suitable performance in both processes.

On the contrary, in fuel cell mode, the performance is lower than that recorded in a conventional PEM fuel cell equipped with Pt catalysts in particular in the ohmic and diffusion regions [27–29]. This is probably due to the presence of the hydrophobized Ti-grid as gas diffusion layer/current collector. In fact, fuel cell tests are performed after the electrolysis process, and the fuel cell cathode could be completely flooded after operation as electrolyser, although a hydrophobized Ti-grid is used. Accordingly, oxygen is hindered by the presence of water inside the cathode compartment, and this diffusion drawback determines the loss of potential observed in Figure 3. For what concerns the amount of Pt in the bimetallic catalysts, it is observed that a higher amount produces lower potential losses as observed in the activation region (low current density) of the polarization curve. Accordingly, the performance at 0.65–0.7 V (region of interest from a point of view of the efficiency [29]) is higher for the IrO₂/Pt catalysts with increasing amounts of Pt (7/93 > 11/89 > 14/86). By using IrO₂/Pt (14/86) catalyst the performance decreased also in the activation region indicating that IrO₂ covered Pt sites reducing in this way the catalytic activity of the bimetallic catalyst for the oxygen reduction reaction. Since this formulation showed a better behaviour for the electrolysis process, it appears necessary to increase further the catalytic properties of this sample to be used as bifunctional catalyst.

4. Conclusions

IrO₂/Pt catalysts (at different concentrations) were synthesized and characterized in Unitized Regenerative Fuel Cell (URFC) configuration. These oxide-metal mixtures were prepared by incipient wetness technique and characterized by XRD, XRF, SEM, and electrochemical measurements under water electrolysis/fuel cell conditions. For fuel cell operation an excess of Pt favours the oxygen reduction process whereas IrO₂ promotes oxygen evolution. From the present results, it appears that the diffusion characteristics and the reaction rate in fuel cell mode are significantly lower than in the electrolyser mode. This requires the enhancement of the gas diffusion properties of the electrodes and the catalytic properties for cathode operation in fuel cells.

References

- [1] W. Smith, "The role of fuel cells in energy storage," *Journal of Power Sources*, vol. 86, no. 1, pp. 74–83, 2000.
- [2] A. Verma and S. Basu, "Feasibility study of a simple unitized regenerative fuel cell," *Journal of Power Sources*, vol. 135, no. 1–2, pp. 62–65, 2004.
- [3] S. A. Grigoriev, P. Millet, V. I. Poremsky, and V. N. Fateev, "Development and preliminary testing of a unitized regenerative fuel cell based on PEM technology," *International Journal of Hydrogen Energy*, vol. 36, no. 6, pp. 4164–4168, 2011.
- [4] F. Mitlitsky, B. Myers, and A. H. Weisberg, "Regenerative fuel cell systems," *Energy and Fuels*, vol. 12, no. 1, pp. 56–71, 1998.
- [5] S. S. Dhabra, K. Sopian, M. A. Alghoul, and M. Y. Sulaiman, "Review of the membrane and bipolar plates materials for conventional and unitized regenerative fuel cells," *Renewable and Sustainable Energy Reviews*, vol. 13, no. 6–7, pp. 1663–1668, 2009.
- [6] J. Pettersson, B. Ramsey, and D. Harrison, "A review of the latest developments in electrodes for unitized regenerative polymer electrolyte fuel cells," *Journal of Power Sources*, vol. 157, no. 1, pp. 28–34, 2006.
- [7] T. Ioroi, T. Oku, K. Yasuda, N. Kumagai, and Y. Miyazaki, "Influence of PTFE coating on gas diffusion backing for unitized regenerative polymer electrolyte fuel cells," *Journal of Power Sources*, vol. 124, no. 2, pp. 385–389, 2003.
- [8] G. Chen, H. Zhang, H. Ma, and H. Zhong, "Effect of fabrication methods of bifunctional catalyst layers on unitized regenerative fuel cell performance," *Electrochimica Acta*, vol. 54, no. 23, pp. 5454–5462, 2009.
- [9] S.-D. Yim, G.-G. Park, Y.-J. Sohn et al., "Optimization of PtIr electrocatalyst for PEM URFC," *International Journal of Hydrogen Energy*, vol. 30, no. 12, pp. 1345–1350, 2005.
- [10] G. Y. Chen, D. A. Delafuente, S. Sarangapani, and T. E. Mallouk, "Combinatorial discovery of bifunctional oxygen reduction-Water oxidation electrocatalysts for regenerative fuel cells," *Catalysis Today*, vol. 67, no. 4, pp. 341–355, 2001.
- [11] L. L. Swette, A. B. LaConti, and S. A. McCarty, "Proton-exchange membrane regenerative fuel cells," *Journal of Power Sources*, vol. 47, no. 3, pp. 343–351, 1994.
- [12] L. L. Swette, N. D. Kackley, and A. B. LaConti, "Regenerative fuel cells," in *Proceedings of the 27th Intersociety Energy Conversion Engineering Conference*, vol. 1, pp. 1101–1106, August 1992.
- [13] H. Liu, B. L. Yi, M. Hou, J. F. Wu, Z. J. Hou, and H. M. Zhang, "Composite electrode for unitized regenerative proton exchange membrane fuel cell with improved cycle life," *Electrochemical and Solid-State Letters*, vol. 7, no. 3, pp. A56–A59, 2004.
- [14] T. Ioroi, N. Kitazawa, K. Yasuda, Y. Yamamoto, and H. Takenaka, "Iridium oxide/platinum electrocatalysts for unitized regenerative polymer electrolyte fuel cells," *Journal of the Electrochemical Society*, vol. 147, no. 6, pp. 2018–2022, 2000.
- [15] W. Yao, J. Yang, J. Wang, and Y. Nuli, "Chemical deposition of platinum nanoparticles on iridium oxide for oxygen electrode of unitized regenerative fuel cell," *Electrochemistry Communications*, vol. 9, no. 5, pp. 1029–1034, 2007.
- [16] A. Cisar, O. Murphy, and E. Clarke, US Patent 0068544, 2003.
- [17] Y. Zhang, C. Wang, N. Wan, and Z. Mao, "Deposited RuO₂-IrO₂/Pt electrocatalyst for the regenerative fuel cell," *International Journal of Hydrogen Energy*, vol. 32, no. 3, pp. 400–404, 2007.
- [18] R. Adams and R. L. Shriner, "Platinum oxide as a catalyst in the reduction of organic compounds. III. Preparation and properties of the oxide of platinum obtained by the fusion of chloroplatinic acid with sodium nitrate," *Journal of the American Chemical Society*, vol. 45, no. 9, pp. 2171–2179, 1923.
- [19] V. Baglio, A. Di Blasi, T. Denaro et al., "Synthesis, characterization and evaluation of IrO₂-RuO₂ electrocatalytic powders for oxygen evolution reaction," *Journal of New Materials for Electrochemical Systems*, vol. 11, no. 2, pp. 105–108, 2008.

- [20] A. Di Blasi, C. D'Urso, V. Baglio et al., "Preparation and evaluation of RuO₂-IrO₂, IrO₂-Pt and IrO₂-Ta₂O₅ catalysts for the oxygen evolution reaction in an SPE electrolyzer," *Journal of Applied Electrochemistry*, vol. 39, no. 2, pp. 191–196, 2009.
- [21] S. Song, H. Zhang, X. Ma, Z.-G. Shao, Y. Zhang, and B. Yi, "Bifunctional oxygen electrode with corrosion-resistive gas diffusion layer for unitized regenerative fuel cell," *Electrochemistry Communications*, vol. 8, no. 3, pp. 399–405, 2006.
- [22] S. Siracusano, V. Baglio, C. D'Urso, V. Antonucci, and A. S. Aricò, "Preparation and characterization of titanium suboxides as conductive supports of IrO₂ electrocatalysts for application in SPE electrolyzers," *Electrochimica Acta*, vol. 54, no. 26, pp. 6292–6299, 2009.
- [23] V. Antonucci, A. Di Blasi, V. Baglio et al., "High temperature operation of a composite membrane-based solid polymer electrolyte water electrolyser," *Electrochimica Acta*, vol. 53, no. 24, pp. 7350–7356, 2008.
- [24] V. Baglio, R. Ornelas, F. Matteucci et al., "Solid polymer electrolyte water electrolyser based on Nafion-TiO₂ composite membrane for high temperature operation," *Fuel Cells*, vol. 9, no. 3, pp. 247–252, 2009.
- [25] J. C. Cruz, V. Baglio, S. Siracusano et al., "Nanosized IrO₂ electrocatalysts for oxygen evolution reaction in an SPE electrolyzer," *Journal of Nanoparticle Research*, vol. 13, no. 4, pp. 1639–1646, 2011.
- [26] www.chemicals.matthey.com/.
- [27] C. Tori, M. Baleztena, C. Peralta et al., "Advances in the development of a hydrogen/oxygen PEM fuel cell stack," *International Journal of Hydrogen Energy*, vol. 33, no. 13, pp. 3588–3591, 2008.
- [28] J. A. Ruiz and C. F. Zinola, "On the mathematical modelling of diffusion-migration mass transport of protons," *International Journal of Chemical Reactor Engineering*, vol. 8, article A39, 2010.
- [29] A. S. Aricò, A. Stassi, E. Modica et al., "Performance and degradation of high temperature polymer electrolyte fuel cell catalysts," *Journal of Power Sources*, vol. 178, no. 2, pp. 525–536, 2008.

Research Article

Electrocatalytic Reduction of Hydrogen Peroxide on Palladium-Gold Codeposits on Glassy Carbon: Applications to the Design of Interference-Free Glucose Biosensor

Elena Horozova,¹ Totka Dodevska,² Nina Dimcheva,¹ and Ruska Mussarlieva¹

¹ Department of Physical Chemistry, Plovdiv University, 24 Tsar Assen Street, 4000 Plovdiv, Bulgaria

² Department of Inorganic and Physical Chemistry, University of Food Technology, 26 Maritsa Boulevard, 4002 Plovdiv, Bulgaria

Correspondence should be addressed to Nina Dimcheva, ninadd@uni-plovdiv.bg

Received 29 March 2011; Accepted 17 May 2011

Academic Editor: Newton Pimenta Neves Jr.

Copyright © 2011 Elena Horozova et al. This is an open access article distributed under the Creative Commons Attribution License, which permits unrestricted use, distribution, and reproduction in any medium, provided the original work is properly cited.

Following our previous studies on the catalytic activity electrochemically codeposited on graphite Pd-Pt electrocatalysts for hydrogen peroxide electroreduction, a series of glassy carbon electrodes were modified with Pd or (Pd+Au) deposits aiming at the development of even more efficient electrocatalysts for the same process. The resulting electrodes were found to be very effective at low applied potentials (−100 and −50 mV versus Ag/AgCl, 1 M KCl). The surface topography of the electrode modified with Pd+Au mixed in proportions 90% : 10%, exhibiting optimal combination of sensitivity and linear dynamic range towards hydrogen peroxide electrochemical reduction, was studied with SEM and AFM. The applicability of the same electrode as transducer in an amperometric biosensor for glucose assay was demonstrated. At an applied potential of −50 mV, the following were determined: detection limit ($S/N = 3$) of 6×10^{-6} M glucose, electrode sensitivity of $0.15 \mu\text{A } \mu\text{M}^{-1}$, and strict linearity up to concentration of 3×10^{-4} M.

1. Introduction

The ever-increasing interest towards electrochemical sensors has been driven by the numerous advantages they offer over the other analytical techniques, such as

- (i) the simplicity of operating with electrical signals (current, potential, conductivity, or impedance);
- (ii) compact and versatile instrumentation capable of supporting several different electrochemical techniques (steady state or dynamic) in a single device;
- (iii) a possibility to finely tune the electrochemical detection and to customize it so that the tedious sample pretreatment stage could be avoided;
- (iv) broad opportunities for miniaturization to afford portable devices, needing very small amounts of a sample (e.g., only several microlitres) to be analyzed;
- (v) a possibility to perform an automated on-line monitoring, that is, a determination to be carried out

directly in the system where the process/product of interest occurred.

Moreover, the selectivity of the analysis might be drastically improved through coupling sensor with a biological component for molecular recognition (enzymes, cells, or tissues), thus providing the opportunity to selectively determine the analyte in complex liquid matrices. These are the main prerequisites for their wide practical application in important spheres, such as medicine [1, 2], food industry [3], and ecology [4].

A broad spectrum of oxidative enzymes (e.g., glucose oxidase, xanthine oxidase, etc.) is known to produce hydrogen peroxide as a by-product of the target reaction they catalyse in presence of molecular oxygen. Therefore, a large group of amperometric biosensors functions on the principle of measuring the current variation upon the addition of the enzyme substrate which is due to the electrochemical transformation (oxidation or reduction) of

the generated H_2O_2 . The biosensors based on registering the current from the electrochemical oxidation of the formed hydrogen peroxide suffer from poor selectivity, mostly due to the high operational potentials, at which the compounds normally attending biological liquids (organic acids, neurotransmitters, and drugs) are co-oxidised, thus leading to overestimated analyte levels. Alternatively, reducing electrochemically H_2O_2 at low working potentials (usually around 0 V versus Ag/AgCl) [5], where interfering substances are electrochemically inert, allows for a much more selective assay of the analyte. In respect to studies on the surface modified with micro- and nanostructures carbonaceous electrodes as efficient electrocatalysts of hydrogen peroxide, both oxidation and reduction [6–13] are currently on high demand.

Various types of carbonaceous materials have been investigated most often as modified electrodes for determining H_2O_2 : graphite [6, 14], glassy carbon [7, 8, 10, 15–19], carbon-paste electrodes [20, 21], carbon nanotubes [22–24], and so forth. With these electrodes, the selectivity of the electrochemical response to hydrogen peroxide is improved by using different catalytically active modification components: transition metals and their oxides [15, 21], platinum metals, dispersed on their own or mixed with other platinum metals [7, 25], and with nanostructured composite films [8, 26]. Studies aimed at the electroanalytical detection of H_2O_2 with micro- and nanostructured carbon films containing metal particles (2–5 nm), such as Pt, Ni, Cu, and Ir [26], have become common in recent years.

In electrochemical sensor technologies, special attention is paid to carbon nanotubes (CNTs) as a promising electrode material. CNTs have demonstrated to possess a unique combination of excellent structural, mechanical, and electrochemical characteristics [22]. CNT-based electrodes, promoted with metal nanoparticles, are distinguished with their high catalytic activity and have been successfully used for detecting H_2O_2 [23, 24]. The modification was performed through the adsorption of nanoparticles from colloidal solutions or through electrodeposition from a solution of the salt of the respective metal. The second approach is often preferred due to the possibility of strict and accurate control allowing for the high reproducibility of the modification procedure. Contemporary studies proved the electrodeposition as an attractive and cheap method for building-up nanosized metal structures, which does not require expensive equipment [27, 28]. By varying the conditions of modification (applied potential, composition of the electrolyte, deposition time, nature of the carrier, etc.), micro- and nanostructured composite metal deposits with high electrocatalytic activity can be obtained.

Our research has shown that highly porous graphite materials, modified through potentiostatic deposition of Pt, Pd, and mixtures of (Pd+Pt) and (Pd+Au) in varied proportions, prove to be effective electrocatalysts for the reduction of hydrogen peroxide at low working potentials [9, 10]. In addition, modified graphites were characterised with a simple modification protocol, high operational stability over a wide pH-range, and high operational stability with

retaining catalytic activity for over 1 year that motivated us to use them as electrochemical transducers in the design of amperometric biosensors based on the electroreduction of hydrogen peroxide. This study continues our research in the above-mentioned direction, with glassy carbon being the solid support to be modified with microquantities of pure Pd and a mixture (Pd+Au) deposited electrochemically on it. The choice of the carbon material, glassy carbon, is motivated by its high mechanical and chemical stability in aggressive media, and above all by its fullerene-related structure [29], that is, properties that distinguish it from graphite. In addition, substituting one of the components of the catalytically active phase, Pt with gold would potentially affect the catalytic activity towards the target reaction (H_2O_2 electroreduction), and the new data would provide us with a better understanding of the factors affecting the catalytic process as a whole. Based on the above, the present study deals with the development of an efficient and selective electrocatalyst for the reduction of H_2O_2 through modification of glassy carbon with microdeposits of Pd and a mixture of (Pd+Au). Their applicability as transducers in amperometric biosensors, based on hydrogen peroxide producing oxidoreductases, is also demonstrated.

2. Experimental

2.1. Materials. Glucose oxidase (GOx) (E.C. 1.1.3.4) from *Aspergillus niger* (Fluka Biochemica), with homogeneous activity of 198 U mg^{-1} (1 U corresponds to the amount of the enzyme which oxidizes $1 \mu\text{mol}$ glucose per min at pH 7.0 and 25°C); D-glucose monohydrate (Valerus, Sofia, Bulgaria). Hydrogen peroxide and chemicals used for preparing buffer solutions, $\text{Na}_2\text{HPO}_4 \times 12\text{H}_2\text{O}$, citric acid, KOH, and H_3PO_4 , were purchased from Fluka. All solutions were prepared with double-distilled water. The β -D-glucose solution ($5 \times 10^{-3} \text{ M}$ in phosphate-citrate buffer, pH 7.0) was allowed to mutarotate for 24 h before use.

2.2. Preparation of the Electrodes. Glassy carbon (GC) lamellae with a geometric surface $S_{\text{geom}} = 1.35 \text{ cm}^2$ were used. The catalytically active components were deposited in potentiostatic regime ($E_{\text{deposit}} = +0.05 \text{ V}$ versus reversible hydrogen electrode) via a brief electrolysis ($t_{\text{deposit}} = 10 \text{ s}$) from the following electrolytes: 2% solution of PdCl_2 in 0.1 M HCl, alone or mixed with 2% solution of HAuCl_4 in 0.1 M HCl in the following volume to volume ratios: 90% : 10%, 70% : 30%, or 50% : 50%. The respective molar proportions of Pd to Au in the electrodeposition baths have been determined to be 17 : 1; 9 : 2; 2 : 1. The surface coverage was estimated to be *ca.* $18 \mu\text{g cm}^{-2}$. The prepared electrodes were allowed to age for 3–5 weeks until the stabilization of the surface occurs. By the end of ageing period, the chronoamperometric data showed a decrease of the active electrode surface with 15%.

The electrodes will be further denoted in the text as electrodes types A, B, C, and D as follows:

- (i) glassy carbon modified with individual Pd (electrode type A);

- (ii) glassy carbon modified with Pd+Au mixed in a ratio of 90% : 10% (w/w, electrode type B);
- (iii) glassy carbon modified with Pd+Au mixed in a ratio of 70% : 30% (w/w, electrode type C);
- (iv) glassy carbon modified with Pd+Au mixed in a ratio of 50% : 50% (w/w, electrode type D).

2.3. Apparatus and Measurements. All electrochemical measurements were performed in a three-electrode cell with separated compartments (working volume 10–15 mL). An Ag/AgCl, 1 M KCl electrode was used as a reference electrode, and platinum wire as a counter electrode. The electrochemical setup also involved a bipotentiostat, type BiPAD (TACUSSEL, Villeurbanne, France); a generator, type EG-20 (Elpan, Lubawa, Poland); a digital voltmeter, type 1AB105 (ZPU, Pravets, Bulgaria). The solutions were softly bubbled with argon during the measurements, in order to decrease the background current, but not to completely deaerate the solutions. For the experiments with the enzyme electrodes, the access of oxygen to the electrolyte was assured by keeping the cell open. The operational characteristics of the series-modified electrodes were examined by the polarization curves' method in potentiostatic regime (phosphate-citrate buffer, pH 7.0). For maintaining constant temperature a thermostat UH (VEB MLW Prüfgeräte-Werk, Medingen, Germany) was used. The pH of the buffer solutions was adjusted with a pH-meter OP-208 (Radelkis, Budapest, Hungary).

3. Results and Discussion

3.1. Electrocatalytic Reduction of Hydrogen Peroxide. The steady-state polarization curves on glassy carbon electrodes, modified with deposits of Pd only (type A electrode) and with the mixtures of (Pd+Au) (types B, C, and D electrodes) in presence of hydrogen peroxide recorded over the potential range from –250 to +250 mV (versus Ag/AgCl) at 25°C, are shown in Figure 1.

Cathode currents in presence of H₂O₂ resulting from its electrochemical reduction were observed over the studied range of potentials for all four modified glassy carbon electrodes. In the case of a pure glassy carbon electrode and glassy carbon modified with deposits of Au only, no such currents were noted (not shown). Regions of almost limiting current values (plateau) around and below 0 V are observable on the polarization curves for electrodes of types A, B, C, and D, which indicates that each of the modified electrodes might be potentially useful in the electroanalytical assay of hydrogen peroxide. The plateau region was found to be dependent on the nature of the catalytically active modifier (deposits of Pd only, or of palladium-gold mixtures in varied proportions). Limiting current values over the potential range from –100 to +50 mV characterise two of the glassy carbon electrodes: the one modified with Pd only (type A, closed circles) and the type B electrode (open squares). Just as wide is the plateau for the type C electrode (open triangles), though in the potential region from –50 to +100 mV. The type D electrode plateau (asterix), spanning the range

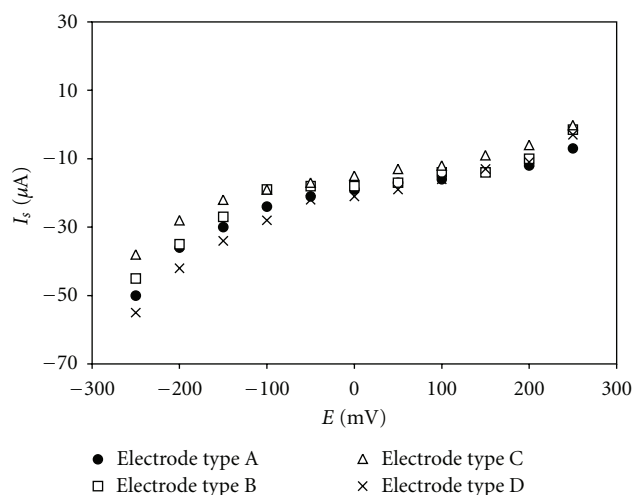


FIGURE 1: Steady-state current as a function of the applied potential at modified glassy carbon electrodes in 0.1 M H₂O₂ present; phosphate-citrate buffer, pH 7.0; reference electrode Ag/AgCl (1 M KCl); temperature 25°C.

from –50 to +50 mV, is the narrowest. Figure 1 shows that besides the width of the plateau, the activity of the glassy carbon electrodes in hydrogen peroxide electroreduction also depends on the composition of the catalytically active phase. The activity of the electrodes estimated as the values of the electrode response towards hydrogen peroxide in the plateau region decreases in the order

$$\text{type D} \sim \text{type B} > \text{type A} > \text{type C.} \quad (1)$$

With all types of glassy carbon, the dependence of the electrode signal (cathode current) on the H₂O₂ concentration at three potentials from the plateau region –0, –50, and –100 mV (versus Ag/AgCl) was studied in a phosphate-citrate buffer, pH 7.0, at room temperature. The electrode response was found to increase linearly with the substrate concentration at the three chosen potentials, with sensitivities (dI/dC, determined from the linear part of calibration graphs, $n = 3$) depending on both the applied potential and the type of the modifying catalytically active component (Figure 2).

For modified glassy carbon of types B, C, and D, the sensitivity increases as the working potential shifts to the negative direction. As a general rule, the electrode sensitivity at potentials –50 and –100 mV was found to be between 1.2 and twice as high as the sensitivity registered at 0 V (Table 1). For glassy carbon modified with Pd only (type A), there were no differences observed in the values of the electrode signal over the same potential range. The linear dynamic range of the electrode signal (in μM) also differs for all electrodes as dependent on the applied potential and on the type of the modifying component. For the type A electrode; however, the linearity of the signal, as well as the sensitivity, increases as the potential shifts negatively. For the other three electrodes—of types B, C, and D, there is no correlation between the linearity of the response and the shifts of the potential in the cathode direction. There is no dependence

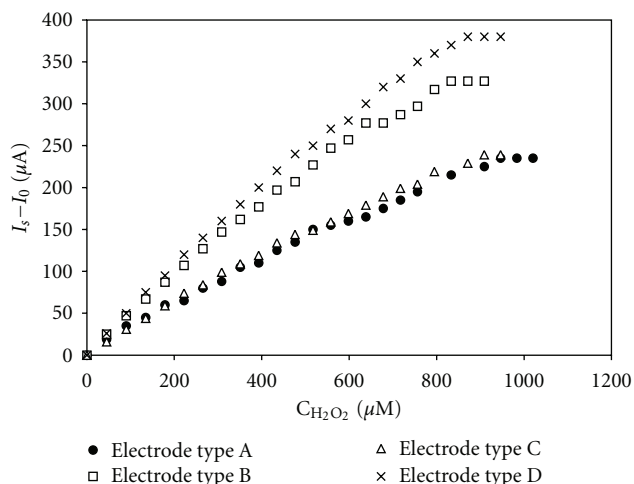


FIGURE 2: Background subtracted steady-state response of the electrode type B (Pd to Au in atomic ratio 90% : 10% on glassy carbon) as a function of hydrogen peroxide concentration at an applied potential of -100 mV (Ag/AgCl, 1 M KCl); phosphate-citrate buffer, pH 7.0; temperature 25°C .

between the linearity of the signal and the percentage of Pd and Au in the microdeposits of the modifying mixture, either.

The dependencies of current on H_2O_2 concentration over the chosen potential region (0 , -50 and -100 mV) were examined under strictly isothermal conditions at ambient temperatures of 25 and 35°C (chosen in view of the anticipated application of the examined electrodes as biosensor transducers). Experimental data show that this 10-degree increase of the temperature affects in a very different way the rate of peroxide electroreduction on the modified GCs (current). While for the first two types of glassy carbon (A- and B-type electrodes), lower currents and hence poorer electrode sensitivities were observed at the higher temperature, for the C- and D-type GC with increasing temperature, higher currents and electrode sensitivities were noticed. These experimental results suggest that in the studied process hydrogen peroxide is consumed simultaneously by two alternative reaction pathways, *namely*, (i) heterogeneous-catalytic decomposition and (ii) electrocatalytic reduction. Most probably, with the first two types of electrode materials (A- and B-type GC), the purely heterogeneous-catalytic decomposition of hydrogen peroxide successfully competes with the electroreduction reaction, thus lowering the effective concentration of peroxide. This might be due to the availability of numerous different catalytically active sites formed on the surface of the A- and B-type of modified glassy carbon. With the second two electrode materials (C- and D-type), however, there is no such a strong impact of the heterogeneous catalytic pathway on the overall process, and therefore the effect of temperature on the rate of the H_2O_2 electroreduction can be quantified by calculating the effective activation energy according to the equation

$$\ln \frac{I_{T_2}}{I_{T_1}} = \frac{E_a}{R} \left(\frac{1}{T_1} - \frac{1}{T_2} \right). \quad (2)$$

The activation energy of the electrochemical reduction of hydrogen peroxide on the C type GC was found to be virtually the same over the studied range of potentials: $E_a = 31.6 \pm 1.9 \text{ kJ mol}^{-1}$. Similarly, the activation energy of H_2O_2 electroreduction on the D type electrode has been found to be independent of the working potential over the chosen potential region; however, the temperature effect on the reaction rate was much lesser, and the activation energy was calculated to be $11.2 \pm 1.9 \text{ kJ mol}^{-1}$. The low effective activation energy values as well as their independence of the working potential suggest that the electrocatalytic process in both cases is limited by diffusion.

From the basic operational characteristics of glassy carbon electrodes (Table 1), it is evident that the glassy carbon electrodes with the highest sensitivity (dI/dC) are the ones of types B and D at working potentials of -50 and -100 mV. At a potential of -50 mV, the type B electrode is characterized by a longer linear dynamic range of the calibration graph (up to $980 \mu\text{M}$) as compared to the type D electrode (up to $760 \mu\text{M}$).

The surface topography of electrode type B was studied by means of scanning electron microscopy (SEM) and atomic force microscopy (AFM). SEM photograph (Figure 3(a)) shows that the catalytically active phase (atomic ratio of Pd to Au 90% : 10%) is deposited on the glassy carbon support in the form of well-defined oval formations with a size of 100 to 500 nm, while the AFM image (Figure 3(b)) gives a much detailed information about the substructure of the deposits; they consist of fine grains with nearly spherical shape and approximate diameter of 10 – 20 nm.

Ensuring a high selectivity of the analysis is a factor of key importance when designing amperometric biosensors. In this connection, the response of the type B electrode was studied in the presence of electrochemically active substances, which usually attend biological fluids. At potentials of -50 and -100 mV, no electrode response was registered in the presence of uric acid, ascorbic acid, glutathione, and paracetamol, in concentrations of up to $700 \mu\text{M}$, which largely exceed the possible physiological levels. In addition, for the type B electrode, the lowest background currents at potentials of -50 and -100 mV were registered as well. The discussed advantages of the modified glassy carbon electrode of type B were the main prerequisites in choosing it as a transducer in designing an amperometric glucose biosensor.

3.2. Glucose Oxidase Enzyme Electrode. The high activity and selectivity, the sufficiently long dynamic range of the response, the low background currents, and the great number of catalytically active centres of glassy carbon modified with microquantities of (Pd to Au 90% : 10%) were the main prerequisites for its use as a basic biosensor transducer. On it, by immobilizing GOx in accordance with a previously reported procedure [10], a new glucose oxidase enzyme electrode was developed. The possibility to determine quantitatively glucose at potentials of -100 and -50 mV in a phosphate-citrate buffer pH 7.0, at temperatures of 25°C and 35°C (Table 2), was examined.

The presented data shows that a rise of the temperature with 5°C results in an increased current response which is

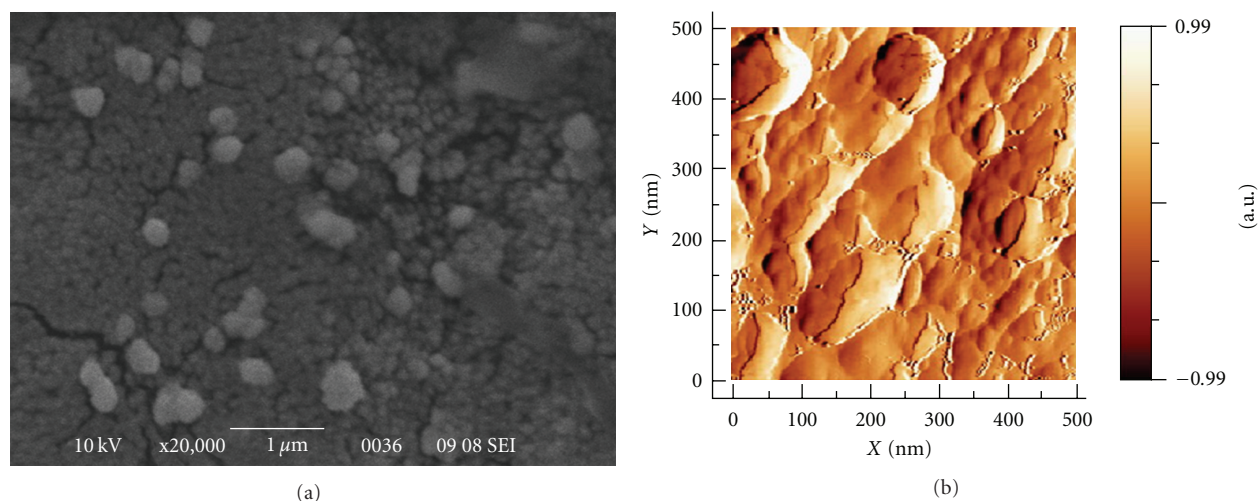


FIGURE 3: SEM (a) and AFM (b) of electrode type B (microdeposits on glassy carbon from the modifying solution of Pd to Au mixed in atomic ratio 90% : 10%).

TABLE 1: Electrode sensitivities (determined from the linear portions of the calibration graphs at temperatures 25 and 30 degree, correlation coefficients ranging between 0.98 and 0.99) and linear dynamic ranges of GC electrodes modified with microquantities of (Pd+Au) mixtures during hydrogen peroxide electrochemical reduction; temperatures 25 and 35°C; phosphate-citrate buffer pH 7.0; reference electrode Ag/AgCl (1 M KCl).

E (mV)	T (°C)	Sensitivity ($\mu A \mu M^{-1}$) electrode type				Linearity (μM)* electrode type			
		A	B	C	D	A	B	C	D
-100	25	0.27	0.42	0.28	0.47	900	800	870	830
	35	0.27	0.45	0.40	0.55				
-50	25	0.26	0.35	0.19	0.36	800	980	1020	760
	35	0.19	0.31	0.30	0.51				
0	25	0.25	0.31	0.14	0.30	680	900	830	800
	35	0.12	0.23	0.21	0.35				

* Linearity ranges for all 4 types of GC electrodes were determined at 25°C.

more extensive at $E = -100$ mV. As the temperature increases and the potential shifts into positive direction, the linear dynamic range shortens, and the electrode sensitivity (dI/dC) increases (Table 2). At $E = -100$ mV, the linear part of the calibration graph is shortened more than twice when the temperature is increased by 5°C. Furthermore, higher background currents were registered at this potential. At a temperature of 25°C, the electrode sensitivity at $E = -50$ mV is 2.2 times as high as that at $E = -100$ mV, and at 30°C, 1.3 times as high. The detection limits of glucose at $E = -50$ mV were found to be $9 \mu M$, and at 30°C were found to be $6 \mu M$ (estimated at signal/noise ratio of 3 : 1).

Therefore, the working potential of $E = -50$ mV was selected as optimal for determining glucose quantitatively. The experimental data on the selected working potential and temperatures 25 and 30°C were presented in Eadie-Hofstee coordinates I_s versus (I_s/C) in accordance with the equation $I_s = I_s^{\max} - K_m \cdot I_s/C$, where the steady-state electrode response (I_s) for a certain concentration of the substrate is represented as a function of the electrode sensitivity at this given concentration (I_s/C) (the ratio of the current

TABLE 2: Operational parameters of glucose oxidase enzyme electrode at temperatures 25 and 30°C; applied potentials -100 and -50 mV (Ag/AgCl, 1 M KCl); background electrolyte: phosphate-citrate buffer pH 7.0.

E (mV)	T (°C)	Sensitivity ($\mu A \mu M^{-1}$)	r^2	Linearity (μM)	K_M^{app} (μM)
-100	25	0.05	0.96 ₈	800	—
	30	0.11	0.96 ₈	380	680
-50	25	0.10	0.98 ₂	450	710
	30	0.15	0.98 ₅	300	405

to the respective concentration of the substrate) (Figure 4). From the calibration graph, (Figure 4(a), left side) it is obvious that the linear dynamic range of the glucose oxidase enzyme electrode spans over the concentration range up to ca. $300 \mu M$. From the presentation of these experimental data in Eadie-Hofstee coordinates (Figure 4(a), right side) it can be deduced that at low substrate concentrations (up to $\sim 300 \mu M$), the sensitivity of the electrode remains

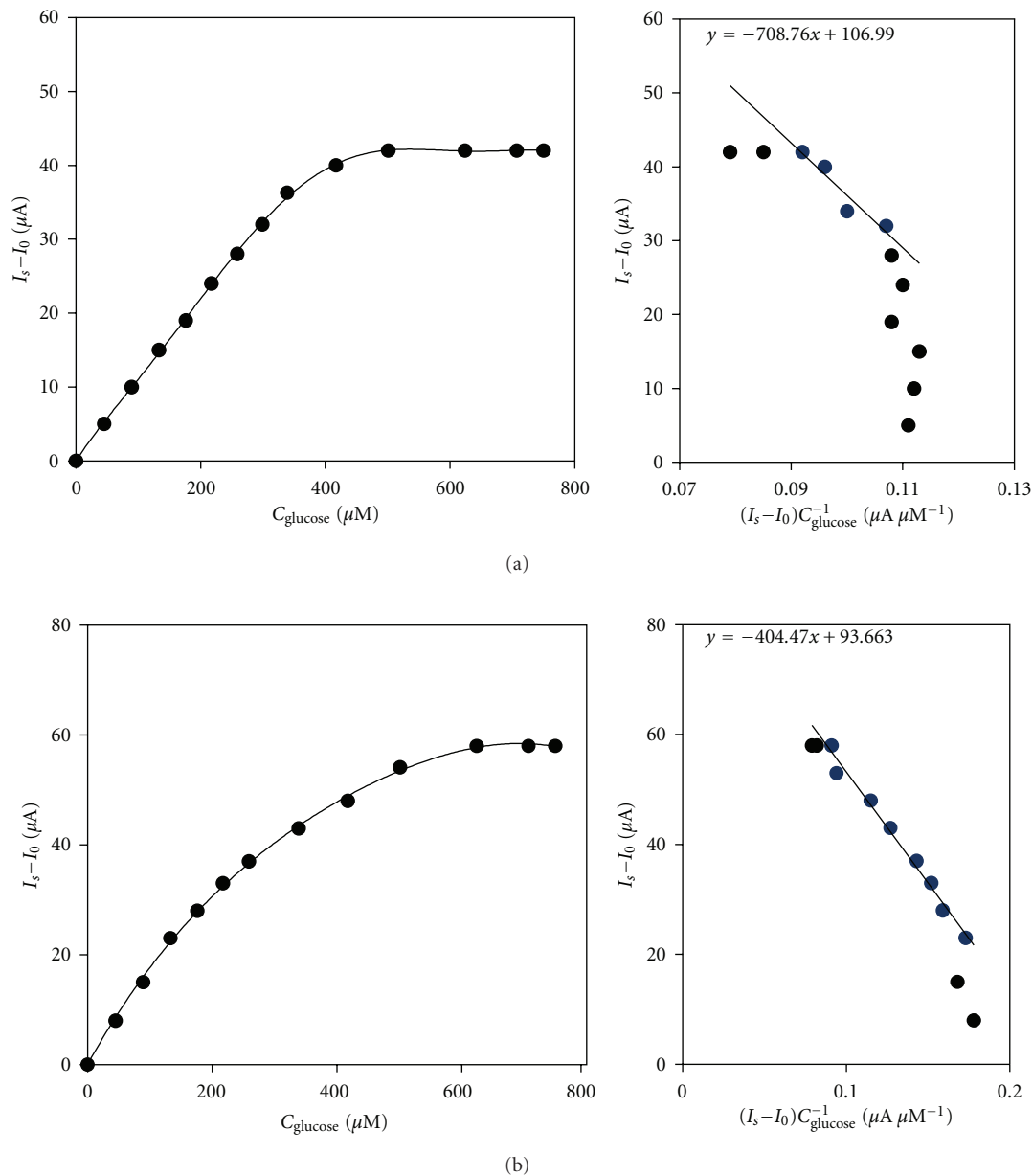


FIGURE 4: Calibration graphs (left sides) and Eadie-Hofstee plots (background subtracted steady-state current as a function of electrode sensitivity, right sides) registered at an applied potential of -50 mV (Ag/AgCl, 1 M KCl); phosphate-citrate buffer, pH 7.0; temperatures: (a) 25°C, (b) 30°C.

practically constant, which is typical for diffusion restrictions over the processes in the bioelectrochemical system. The inclined area between $300 \mu\text{M}$ and $455 \mu\text{M}$ indicates the presence of enzyme-kinetic control, while the horizontal area of the graph refers to high substrate concentrations exceeding $455 \mu\text{M}$ and can be assigned to the effect of saturation of the enzyme with substrate molecules. It is due to the fact that it was impossible for the enzyme to react with all the glucose molecules that reach it. The value of the apparent Michaelis constant $K_M^{\text{app}} = 710 \mu\text{M}$ was determined from the slope of the inclined region. Analogous analysis related to the working mode of the electrode performed at a temperature of 30°C

(Figure 4(b)) suggests that the same three working regimes of the electrode, diffusion, kinetic, and substrate limited, are present.

The diffusion area at this higher temperature, however, is considerably shorter (up to $130 \mu\text{M}$) compared to that at 25°C, while there is an increase in the section in which the electrochemical process takes place under kinetic control (from 130 to $635 \mu\text{M}$). The value of the apparent Michaelis constant $K_M^{\text{app}} = 405 \mu\text{M}$ was found to be 1.8 times as low as the one determined at 25°C. In Table 3, the operational characteristics of the examined electrode were compared to the ones of the glucose oxidase enzyme electrode, determined

TABLE 3: Operational parameters of glucose oxidase enzyme electrodes; applied potential -50 mV (Ag/AgCl (1 M KCl)); background electrolyte: phosphate-citrate buffer pH 7.0.

Electrode type	T ($^{\circ}\text{C}$)	Sensitivity ($\mu\text{A } \mu\text{M}^{-1}$)	r^2	Linearity (μM)	K_M^{app} (μM)
type A_{GOx}	20	0.04	0.97 ₇	550	>1600
	25	0.10	0.98 ₂	450	710
type B_{GOx}	20	0.08	0.96 ₆	240	470
	25	0.13	0.97 ₄	180	310

through immobilization of GOx on porous graphite (GMZ), modified from a solution containing Pd and Au mixed in a ratio of 70% : 30% [10].

The glucose oxidase enzyme electrodes will be referred to as follows:

- (i) the GOx-immobilised electrode based on modified GC (this work)— A_{GOx} type;
- (ii) the GOx-immobilised electrode based on modified GMZ-graphite [10]— B_{GOx} type.

From the data presented in Table 3, it is evident that at both working temperatures the sensitivity of the type B_{GOx} electrode is as high as 1.7 times (at 20°C) and as high as 1.3 times (at 25°C) compared to the sensitivity of the type A_{GOx} electrode. The lower sensitivity of the type A_{GOx} electrode is accompanied by linear dynamic range of the response that is 2.5 times as long, as well as with higher values of the apparent Michaelis constant K_M^{app} . The differences in the operational parameters of the glucose oxidase enzyme electrodes shown above can be due to both the different proportions of Pd and Au microquantities in the modifying mixture, and to the different basic carbon matrix graphite and glassy carbon. These lead to a difference in the structure of the electrodeposited active phase [9] which eventually affects the conformation of GOx during its immobilization (which means it affects its activity).

4. Conclusions

Efficient electrocatalysts for the reduction of hydrogen peroxide at low potentials, around and below 0 V (versus Ag/AgCl), have been obtained by modifying glassy carbon matrices with microquantities of Pd and mixtures (Pd+Au), in different proportions of the catalytically active components. The basic kinetic (E_a) and operation parameters (electrode sensitivity, linear dynamic range, and detection limits) of the electrodes in the target reaction have been resolved. A selective biosensor for amperometric determination of glucose based on electrocatalytic peroxide electrode of the B-type (Pd to Au mixed in atomic ratio 90% : 10% deposits on glassy carbon) has been developed.

The following conditions have been established as optimal for determining glucose quantitatively:

- (i) working potential of -50 mV,
- (ii) a temperature of $25\text{--}30^{\circ}\text{C}$.

Under the above conditions, a detection limit of 6×10^{-6} M, electrode sensitivity of $0.15 \mu\text{A } \mu\text{M}^{-1}$, and linear dynamic range of the response up to $300 \mu\text{M}$ have been determined.

Acknowledgments

The authors acknowledge the support from the Bulgarian National Science Fund (Grant no. DVU-02/38).

References

- [1] M. A. Rahman, M. S. Won, and Y. B. Shim, "Xanthine sensors based on anodic and cathodic detection of enzymatically generated hydrogen peroxide," *Electroanalysis*, vol. 19, no. 6, pp. 631–637, 2007.
- [2] X. C. Tan, Y. X. Tian, P. X. Cai, and X. Y. Zou, "Glucose biosensor based on glucose oxidase immobilized in sol-gel chitosan/silica hybrid composite film on Prussian blue modified glass carbon electrode," *Analytical and Bioanalytical Chemistry*, vol. 381, no. 2, pp. 500–507, 2005.
- [3] H. Nakatani, L. Santos, C. Pelegrine et al., "Biosensor based on xanthine oxidase for monitoring hypoxanthine in fish meat," *American Journal of Biochemistry and Biotechnology*, vol. 1, pp. 85–89, 2005.
- [4] A. Arvinte, L. Rotariu, and C. Bala, "Development of a pesticides biosensor using carbon-based electrode systems," in *Chemicals as Intentional and Accidental Global Environmental Threats*, L. Simeonov and E. Chirila, Eds., pp. 337–343, Springer, The Netherlands, 2006.
- [5] N. Dimcheva, E. Horozova, and Z. Jordanova, "A glucose oxidase immobilized electrode based on modified graphite," *Zeitschrift fur Naturforschung*, vol. 57, no. 7-8, pp. 705–711, 2002.
- [6] P. J. Kulesza, R. Marassi, K. Karnicka et al., "Electrocatalysis and bioelectrocatalysis and nanostructured composite films," *Reviews on Advanced Materials Science*, vol. 15, no. 3, pp. 225–233, 2007.
- [7] L. Sun, D. Cao, and G. Wang, "Pd-Ru/C as the electrocatalyst for hydrogen peroxide reduction," *Journal of Applied Electrochemistry*, vol. 38, no. 10, pp. 1415–1419, 2008.
- [8] Z. Taha and J. Wang, "Electrocatalysis and flow detection at a glassy carbon electrode modified with a thin film of oxymanganese species," *Electroanalysis*, vol. 3, pp. 215–219, 1991.
- [9] E. Horozova, T. Dodevska, and N. Dimcheva, "Modified graphites: application to the development of enzyme-based amperometric biosensors," *Bioelectrochemistry*, vol. 74, no. 2, pp. 260–264, 2009.
- [10] T. Dodevska, E. Horozova, and N. Dimcheva, "Electrocatalytic reduction of hydrogen peroxide on modified graphite electrodes: application to the development of glucose biosensors," *Analytical and Bioanalytical Chemistry*, vol. 386, no. 5, pp. 1413–1418, 2006.
- [11] C. M. Welch, C. E. Banks, A. O. Simm, and R. G. Compton, "Silver nanoparticle assemblies supported on glassy-carbon electrodes for the electro-analytical detection of hydrogen peroxide," *Analytical and Bioanalytical Chemistry*, vol. 382, no. 1, pp. 12–21, 2005.
- [12] E. Horozova, Z. Jordanova, and A. Angelacheva, "The effect of the nature of the electrode material on the oxidation rates of

- hydrogen peroxide, ascorbic acid, uric acid and glutathione," *Bulletin of Electrochemistry*, vol. 13, no. 7, pp. 321–326, 1997.
- [13] R. L. R. P. Fagury, K. O. Lupetti, and O. Fatibello-Filho, "Flexible potentiometric minisensor based on manganese dioxide-composite for the determination of hydrogen peroxide in bleach and pharmaceutical products," *Analytical Letters*, vol. 38, no. 12, pp. 1857–1867, 2005.
- [14] A. S. Kumar and S. Sornambikai, "Selective amperometric sensing of hydrogen peroxide with nafionlcopper particulates chemically modified electrode," *Indian Journal of Chemistry Section A*, vol. 48, no. 7, pp. 940–945, 2009.
- [15] H. Ryoo, Y. Kim, J. Lee, W. Shin, N. Myung, and H. G. Hong, "Immobilization of horseradish peroxidase to electrochemically deposited gold-nanoparticles on glassy carbon electrode for determination of H_2O_2 ," *Bulletin of the Korean Chemical Society*, vol. 27, no. 5, pp. 672–678, 2006.
- [16] L. Duan, Q. Xu, F. Xie, and S. Wang, "Hydrogen peroxide biosensor based on the bioelectrocatalysis of myoglobin incorporated in multi-walled carbon nanotubes/chitosan composite film," *International Journal of Electrochemical Science*, vol. 3, pp. 118–124, 2008.
- [17] A. Ernst, O. Makowski, B. Kowalewska, K. Miecznikowski, and P. J. Kulesza, "Hybrid bioelectrocatalyst for hydrogen peroxide reduction: immobilization of enzyme within organic-inorganic film of structured Prussian Blue and PEDOT," *Bioelectrochemistry*, vol. 71, no. 1, pp. 23–28, 2007.
- [18] S. Varma and C. K. Mitra, "Bioelectrochemical studies on catalase modified glassy carbon paste electrodes," *Electrochemistry Communications*, vol. 4, no. 2, pp. 151–157, 2002.
- [19] V. M. Ivama and S. H. P. Serrano, "Rhodium-prussian blue modified carbon paste electrode (Rh-PBMCPE) for amperometric detection of hydrogen peroxide," *Journal of the Brazilian Chemical Society*, vol. 14, no. 4, pp. 551–555, 2003.
- [20] K. Schachl, H. Alemu, K. Kalecher, J. Jeřkova, I. Švancara, and K. Vytras, "Amperometric determination of hydrogen peroxide with a manganese dioxide-modified carbon paste electrode using flow injection analysis," *Analyst*, vol. 122, pp. 985–989, 1997.
- [21] S. Arjsiriwat, M. Tanticharoen, K. Kirtikara, K. Aoki, and M. Somasundrum, "Metal-dispersed conducting polymer-coated electrode used for oxidase-based biosensors," *Electrochemistry Communications*, vol. 2, no. 6, pp. 441–444, 2000.
- [22] K. Balasubramanian and M. Burghard, "Biosensors based on carbon nanotubes," *Analytical and Bioanalytical Chemistry*, vol. 385, no. 3, pp. 452–468, 2006.
- [23] P. Yang, W. Wei, C. Tao, B. Xie, and X. Chen, "Nano-silver/multi-walled carbon nanotube composite films for hydrogen peroxide electroanalysis," *Microchimica Acta*, vol. 162, no. 1-2, pp. 51–56, 2008.
- [24] M. Yang, Y. Yang, Y. Liu, G. Shen, and R. Yu, "Platinum nanoparticles-doped sol-gel/carbon nanotubes composite electrochemical sensors and biosensors," *Biosensors and Bioelectronics*, vol. 21, no. 7, pp. 1125–1131, 2006.
- [25] R. Garjonyte and A. Malinauskas, "Amperometric sensor for hydrogen peroxide, based on Cu_2O or CuO modified carbon paste electrodes," *Fresenius' Journal of Analytical Chemistry*, vol. 360, no. 1, pp. 122–123, 1998.
- [26] O. Niwa, "Electroanalytical chemistry with carbon film electrodes and micro and nano-structured carbon film-based electrodes," *Bulletin of the Chemical Society of Japan*, vol. 78, no. 4, pp. 555–571, 2005.
- [27] T. Oyama, T. Okajima, and T. Ohsaka, "Electrodeposition of gold at glassy carbon electrodes in room-temperature ionic liquids," *Journal of the Electrochemical Society*, vol. 154, no. 6, pp. D322–D327, 2007.
- [28] E. Alvarez and R. Salinas, "Electrochemically deposited Pd nanocrystals on vitreous carbon," in *Proceedings of the 2nd Mercosur Congress on Process Systems Engineering*, Rio de Janeiro, Brasil, 2005.
- [29] P. J. F. Harris, "Fullerene-related structure of commercial glassy carbons," *Philosophical Magazine*, vol. 84, no. 29, pp. 3159–3167, 2004.

Research Article

The Electrochemical Development of Pt(111)Stepped Surfaces and Its Influence on Methanol Electrooxidation

E. Teliz,¹ V. Díaz,² R. Faccio,³ A. W. Mombrú,³ and C. F. Zinola²

¹ Núcleo Ingeniería Electroquímica, Facultad de Ingeniería, Instituto de Ingeniería Química-Laboratorio de Electroquímica Fundamental, Facultad de Ciencias, Instituto de Química Biológica, Rodó 1843, Udelar, Montevideo 11400, Uruguay

² Núcleo Ingeniería Electroquímica, Facultad de Ingeniería, Instituto de Ingeniería Química-Laboratorio de

Electroquímica Fundamental, Facultad de Ciencias, Instituto de Química Biológica, Rodó 1843, Udelar, Montevideo 11400, Uruguay

³ Laboratorio de cristalografía, estado sólido y materiales (Cryssmat-Lab), DETEMA, Centro NanoMat, Polo Tecnológico de Pando, Facultad de Química, Gral. Flores 2224, Udelar, Montevideo 11000, Uruguay

Correspondence should be addressed to V. Díaz, verodiaz@fing.edu.uy

Received 1 April 2011; Accepted 6 May 2011

Academic Editor: Maria E. Martins

Copyright © 2011 E. Teliz et al. This is an open access article distributed under the Creative Commons Attribution License, which permits unrestricted use, distribution, and reproduction in any medium, provided the original work is properly cited.

The progress in the preparation of new electrode surfaces by electrochemical treatments exhibiting high faradaic efficiencies towards industrial electrocatalytic processes has gained more attention in today's scientific community. Most of the papers report new catalysts dispersed on different substrates, but some fundamental studies required for electrochemical and physical characterizations are sometimes forgotten. In this paper, we make a full staging of two electrochemical treatments that can be conducted to enhance the electrocatalytic activity of platinum surfaces, such as, electrofacetting through square wave potential programs and constant cathodic polarizations in the net hydrogen evolution region. The cathodic treatment applied at -2 V clearly develops (111) stepped planes similarly to the electrofacetting performed after applying the square wave program between 1.40 V and 0.70 V at 2.5 kHz. The X-ray diffraction patterns of both surfaces as well as on other electrofaceted platinum electrodes are obtained for comparison purposes. Moreover, the electrocatalytic activity towards methanol electrooxidation also exhibits equivalent coulombic efficiencies and 200% higher than on polycrystalline platinum as demonstrated by linear sweep voltammetry and potentiostatic current decays.

1. Introduction

A solid surface is a physical region that confines the crystal growth and the emergence of new physical properties different to those of the bulk. In the case of a solid/(liquid or gas) interface, the heterogeneous catalyst can lead to significant changes depending on the presence or the absence of an electric field. Moreover, a single-crystal (sc) solid/liquid interface is of special interest since it restricts the freedom degrees of surface mobility. Thus, surface atoms can take positions different from those expected depending on the characteristics of the applied electrode potential. This surface phenomenon is called reconstruction and is usually studied in physics with the help of ultrahigh vacuum (UHV) techniques [1]. However, this process strongly depends on the nature of the metal. Thus, platinum type metals are considered one of the most important catalysts as anodes

and cathodes in polymer electrolyte fuel cells. This is mainly due to the large values of exchange current densities of the electrochemical reactions and the surface stability in the case of electrodisolution and/or electrodeposition [2, 3]. Surface reconstruction at platinum/solution interface is usually the result of an electronic redistribution occurring as a consequence of either ion adsorption or oxygen-containing species formation, finally leading to surface facets. In the case of polycrystalline (pc) surfaces, the formation of facets of a fixed crystal orientation is of particular interest for industrial applications such as electrosynthesis, fuel cell technology, and electrolysis [4, 5] due to the large stability even at potentials as high as 1.6 V.

The surface structure of a sc can be checked by a number of selected techniques such as scanning tunneling microscopy (STM) and atomic force microscopy (AFM) [6]; however, in the case of electrofaceted surfaces the atomic

resolution is difficult to achieve due to the large number of defects. Moreover, other techniques are currently used to obtain the fingerprint of the electrode surface such as cyclic voltammetry (CV), which offers current versus potential data for sc and also for pc surfaces. CVs give important information about the adsorption/desorption states, phase formation of transitions, and so forth at the electrode surface as a function of potential. From the CV of platinum recorded between the potentials of solvent stability, one can distinguish the potential regions corresponding to the double-layer charging, hydroxide/oxide layer formation/reduction, and hydrogen adsorption/desorption [7].

In the case of noble metal interfaces, some CV current peaks can be assigned to defined X-ray diffraction (XRD) patterns [8, 9]. It was commonly accepted that a voltammetric peak is directly connected to a single X-ray excitation. However, it has been found that current intensities can also change between subsequent cycles because of surface restructuring induced by the electrode potential cycling [10, 11]. In the case of platinum, the effects of such cycles have been interpreted [12] as the progressive development of (110) or higher atomic stepped equivalent facets because of platinum oxide phase formation and reduction.

The morphology and structure of a catalyst surface has a strong weight on its electrochemical reactivity [3]. Thermo- or potential-induced surface reconstruction has been observed on clean metal surfaces with different crystallographies depending on type of atmosphere where the process is developed. If the rearrangement of surface atoms goes much further than atomic spacing, macroscopic changes, which are called surface reshaping, could happen to the surface morphology [13]. In particular, when pc metals are treated by periodic perturbing potentials, they are susceptible to remarkable changes in surface roughness and in the distribution of crystallographic faces, which is denoted as preferred crystallographic orientations via electrochemical faceting, [6, 8]. Tian et al. [14] reported the synthesis of platinum nanocrystals using repetitive square wave routines, and the obtained nanocrystals display high-index facets with a 400% more reactive activity than existing commercial platinum catalysts. Thus, surface restructuring in electrochemistry produces changes in the kinetics or even in the mechanism of various processes because of their strong sensitivity towards the metal surface structure [12, 15]. It has to be said that pc surfaces also exhibit surface restructuring, and in the case of the application of periodic potentials, they lead to the electroformation of microfacets [12]. It is well known that the application of fast potential periodic programs on platinum, rhodium, iridium, gold, or palladium produces permanent morphological changes with defined orientations, which depend on the potential limits and frequency of the routine by a microfacetting process [16–18]. The electrochemical responses of these stepped surfaces are similar to those of stepped crystalline surfaces [19, 20].

It has been shown in a previous paper [21] that besides the main forces that drive the surface restructuring and microfacetting (oxygen and hydrogen electroadsorption) the frequency of the square wave potential itself leads to a

single propagation mode. This is the one responsible of the crystal lattice surface rearrangement, with new equilibrium positions that can be calculated with the potential periodic perturbations as parameters.

The voltammetry for the oxidation of methanol on sc platinum shows a clear hysteresis between the positive and negative going scans due to the accumulation of the poisoning intermediate at low potentials and its oxidation above 0.7 V versus RHE [22]. Additionally, the reaction is also very sensitive to the surface structure. The Pt(111) electrode has the lowest catalytic activity and the smallest hysteresis in a single voltammetric scan whereas Pt(100) electrode displays a much higher catalytic activity and a fast poisoning reaction. On the other hand, Pt(110) electrode depends on the pretreatment of the surface [23].

Besides the studies with the three basal planes, methanol electrooxidation was also performed on stepped platinum surfaces in order to clarify how exactly the step density influences this reaction. Shin and Korzenicwski [24] suggested that an increase of the step density catalyzes methanol decomposition whereas Tripković and Popvić [25] showed that the increase in the step density leads to a decrease in the surface activity towards methanol electrooxidation, both authors using Pt[$n(111) \times (100)$]. Housmans and Koper [26] studied methanol oxidation on Pt[$n(111) \times (110)$] stepped surfaces, and reported an increase in the activity with the step density, suggesting that the presence of steps with a (110) orientation catalyzes methanol decomposition, carbon monoxide oxidation, and also the direct methanol oxidation. These kinds of studies are relevant not only from a fundamental point of view, but also for technical purposes, that is, once the proper crystallographic orientation is found, the technical electrode can be designed. Surfaces nanoparticles should be deposited in the carbon supported with the corresponding crystallographic orientation that resulted with the best electrocatalytic performance.

2. Experimental

Electrochemical runs were performed using a three-electrode compartment cell with a pc platinum wire of 0.5 mm diameter as a working electrode (99.999% purity, from Goodfellow Cambridge). A large area smooth platinum counter electrode and a reversible hydrogen reference electrode with a Luggin-Haber capillary tip completed the electrochemical system. Potential values in the text are given on the hydrogen reference electrode (RHE) scale. We employed 1 M sulphuric acid (96–98% analytical reactive from Baker) as supporting electrolyte, which was prepared using ultrapure water from Millipore-MilliQ plus (18.2 M Ω cm of resistivity). We performed the electrochemical experiments using a PGZ 301 Voltalab potentiostat-galvanostat with the Voltmaster 4 software.

To obtain the electrofaceted platinum surfaces (PtF), the electrodes were subjected to different potential techniques. However, the most attractive of all was the repetitive square wave potential scanning (RSWPS) in the symmetric form to avoid large surface roughness. To optimize the square wave potential parameters, we changed the lower E_d and

upper E_u potentials together with the applied frequency, f , only in the symmetric mode during a certain time t . In all cases, the process was followed by registering the CV profile of the interface between 0.05 and 1.45 V at 0.10 Vs^{-1} , always comparing with the nonperturbed electrode. The preferential oriented surface (faceted surface) with symmetries equivalent to (111) and (100) are obtained by widely changing the parameters shown above. The electrochemical experiments comprised the following stages: (i) electrode pretreatment involving repetitive triangular potential cycling at 0.1 Vs^{-1} between 0.05 and 1.50 V until a stabilized voltammogram was attained; (ii) the pretreated electrode was subsequently subjected to an *RSWPS* between E_d and E_u at f , during a certain time t or a cathodic treatment at $E = -2 \text{ V}$ during 30 min; (iii) the CV of the treated electrode was recorded again under the same conditions indicated in (i); (iv) XRD of the treated electrode were then obtained systematically.

We used the following criteria to estimate the development of preferred crystallographic orientation [6, 16]. The main voltammetric peak at low potentials of weakly bound hydrogen electrosorption at the platinum/acid interface (h_1), originally assigned to the H-adatom-Pt(111) site interaction, corresponds to H-electrosorption on disturbed Pt(111) surfaces with a larger number of Pt(110) sites whereas the main voltammetric peak at higher potentials (h_2 ; strongly bound H-adatoms) represents the H-adatom-Pt(100) site interaction. Accordingly, the height ratio between these two peaks, h_2/h_1 , can be taken arbitrarily to follow the degree of preferred crystallographic orientation achieved throughout the treatment described in (ii). Thus, for the untreated platinum surfaces electrode, the average h_2/h_1 ratio was ca. 0.84.

The most representative and relevant results involved a repetitive 5 KHz wave between $E_u = 1.50 \text{ V}$ and $E_d = 0 \text{ V}$ for faceted Pt(100) surfaces and the application of a 2.5 KHz between $E_u = 1.40 \text{ V}$ and $E_d = 0.70 \text{ V}$ for faceted Pt(111) surfaces. The current transients were recorded during the process and a potentiostatic holding at 0.05 V for 10 min was applied to eliminate dissolved molecular hydrogen under continuous nitrogen bubbling. Immediately after and under a continuous potential control, the CVs were run from 0.05 to 0.70 V at 0.10 Vs^{-1} . All runs were achieved at $20 \pm 2^\circ \text{C}$, under free oxygen conditions using nitrogen (99.998% purity) from Linde-Gas.

In order to study the electrocatalytic performance of the new surfaces produced by the electrofaceted and cathodic pretreatments two methodologies were carried out in oxygen-free 0.1 M methanol + 1 M sulphuric media, namely, linear sweep voltammetry and potentiostatic chronoamperometric curves. Linear sweep voltammetry was conducted on each surface starting from 0.10 V and scanning towards positive values at 0.010 Vs^{-1} . Chronoamperometric curves were performed until 10 minutes at 0.60 V and 0.70 V for the nonperturbed and the treated surfaces. The charge density values under the chronoamperometric plots were calculated until that time only for comparison purposes.

X-ray powder diffraction data were collected using a Rigaku ULTIMA IV, 285 mm radius, Powder Diffractometer

operating in Bragg-Brentano geometry. $\text{CuK}\alpha$ radiation ($\lambda = 1.5418 \text{ \AA}$) monochromatized with a diffracted beam bent germanium crystal was used to collect data over the 39 to 90 degree 2θ range in steps of 0.02° and 0.01° deg using a scintillation detector. Peak positions were extracted from the diffractograms using the program POWDERX [27]. Multiple datasets were collected for each sample in order to obtain representative values.

3. Results

3.1. Electrochemical Characterization. Figure 1(a) depicts the electrochemical profile of platinum after annealing. For these surfaces the current intensities ratio between h_2 and h_1 is 0.84. This is the original surface, which is taken as the blank of all the applied pretreatments. Figure 1(b) shows in this case a clear trend to develop the (111) terraces with a ratio $h_2/h_1 = 0.52$. The *RSWPS* treatment under the conditions described in Figure 1(c) produces remarkable changes in the voltammetric response of the treated surfaces as well as in the corresponding surface morphologies comparing to the blank. Likewise, the relative distribution of voltammetric peaks is modified, that is, the Pt F100 develops the $h_2/h_1 = 1.80$ ratio. On the other hand, the cyclic voltammetric profile as a result of the cathodic treatment is shown in Figure 1(d). The relative distribution of peaks is between the blank and the profile of Pt F(111), that is the h_2/h_1 ratio is 0.75. Due to the appearance of more electrochemical contributions, the voltammetric contours are slightly wider. It is likely that a stepped surface arises with global (111) planes between that we consider the blank and the Pt F111.

3.2. Structural Characterization by X-Ray Powder Diffraction (XRPD). All the samples shown above in Figure 2 exhibit peak positions strictly corresponding to Pt^0 , which indicates no further oxidation at the catalyst occurring after applying the *RSWPS*. It is important to mention that all the samples present good stability, since they were also measured after periods of one month and presented no difference in the diffractograms.

When comparing the diffractograms of the treated samples, important changes can be seen in the relative intensity of the Bragg's peaks. This fact reflects the preferential orientation obtained by the *RSWPS* and the stepped planes developed after the CT, see Table 1 for details.

In the first case, the starting sample corresponds to the pc platinum wire with the intensity of (220) and (311) reflections considerable higher than the others. Since it is difficult to establish a direct comparison between the occurrences of lattice planes with the corresponding reflection intensities, we defined a "weighted intensities" using relative currents. The weights are cleared in terms of the intensities of the bulk platinum reflections. For example, platinum bulk has $I(111) = 100$ and $I(200) = 53$. They have equal occurrence in pc samples, so the direct ratio between unnormalized intensities leads to $I(111)/I(200) = 0.53$. If we define the weighted ratio as $I_w(111)/I_w(200) = I(111)/I(200) * (I_{\text{bulk}}(200)/I_{\text{bulk}}(111)) = 1$, the number

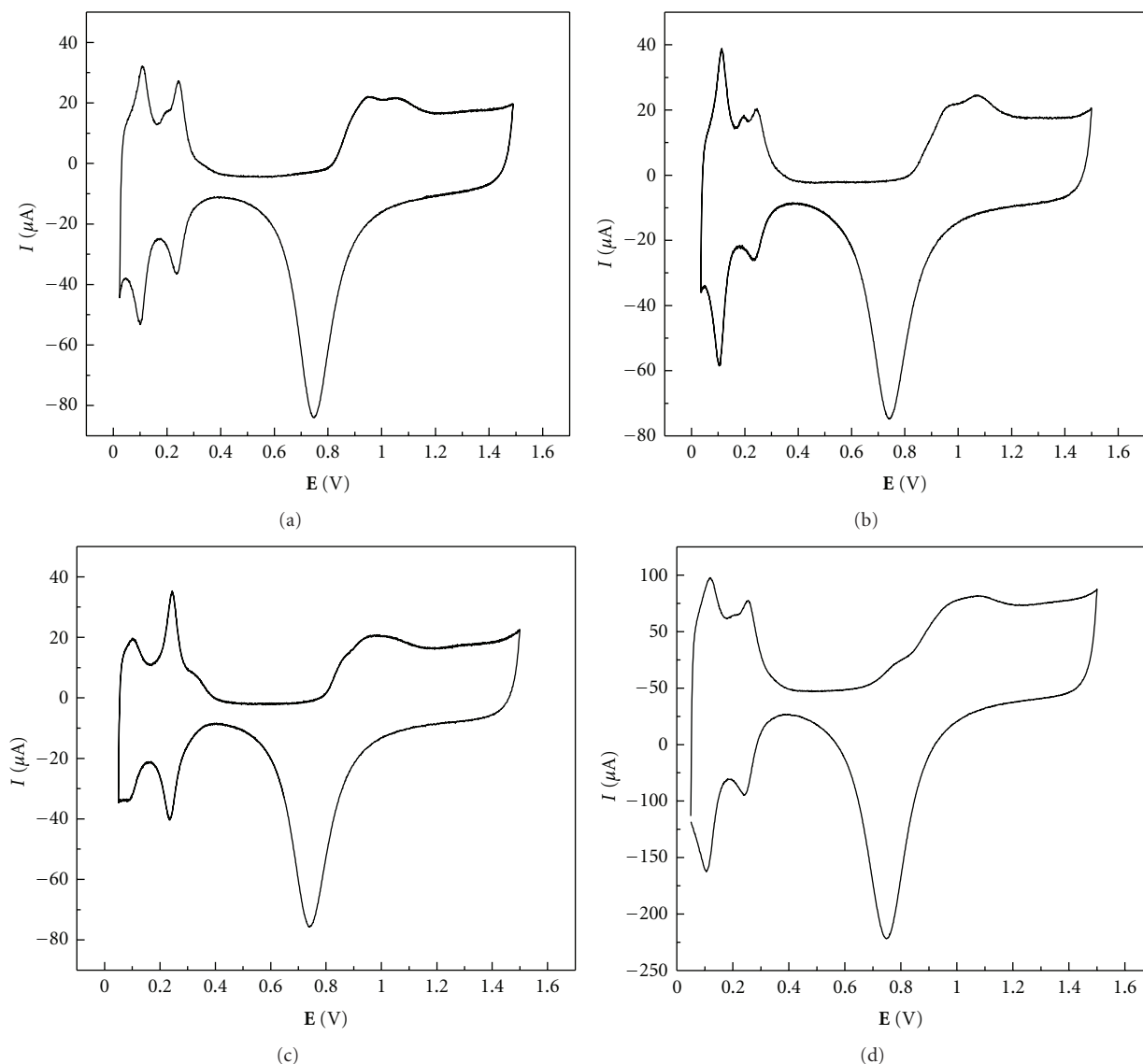


FIGURE 1: Cyclic voltammetry in 1 M sulphuric acid between 0.05 V and 1.50 V run at 0.10 V s^{-1} for (a) Pt pc annealing $h_2/h_1 = 0.84$; (b) Pt F(111) after a RSWPS $E_d = 0.70 \text{ V}$, $E_u = 1.40 \text{ V}$, $f = 2.5 \text{ kHz}$, $t = 10 \text{ minutes}$, $h_2/h_1 = 0.52$; (c) Pt F(100) after an RSWPS $E_d = 0.00 \text{ V}$, $E_u = 1.50 \text{ V}$, $f = 5.0 \text{ kHz}$, $t = 10 \text{ minutes}$, $h_2/h_1 = 1.80$; (d) CT Pt after $E = -2 \text{ V}$, $t = 30 \text{ minutes}$. $h_2/h_1 = 0.75$.

give us a direct estimation of the proportion between lattice planes.

Table 2 presents the weighted ratio for all the studied samples. According with this data pc platinum has an important contribution from (100) reflection in comparison with (111), that is, $I_w(100)/I_w(111) = 3.34$. This behavior is similar to the sample with CT, followed by the sample with faceting treatment to (100) direction (F100). The same trend is observed for (311) reflection in the three cases. The main difference between pc and CT platinum is in the (220) reflection, which is considerably high for the first sample. The XRPD is not grazing incidence experiments, so the conclusions cannot be only attributed to surface phenomena, but they can be attributed to both surface and bulk material. In this sense, the pc orient planes (220) and (311) and (200) can be easily interpreted in terms of (111) and (100) surface stepping like $(111) \times (111) \rightarrow (220)$ and $(111) \times (100) \rightarrow$

(311). This feature is slightly modified after the CT, since the intensity of the (220) reflection is reduced by a factor of ca. 3.8. This fact is interpreted as a reduction in the $(111) \times (111)$ stepping, when a restitution of the (111) reflection occurs characterized by the weighted ratio $I_w(111)/I_w(222) = 1.09$. According to this, the CT favors the (111) and (100) stepping as presented in Figure 2 and Table 2.

Regarding the Pt F100 sample, the faceting process does not establish a clear change in the proportion of the (200) lattice planes, since the weighted ratio shows the lowest value after comparing Pt F100 with pc platinum and CT platinum. Another feature is the intensity of the (220) reflection, which shows an intermediate contribution with an intensity positioned between those of pc and CT platinum.

Finally, the Pt F111 sample is the one with greatest differences, with a nearly net contribution arises from the (111) lattice planes referred with the (222) lattice planes.

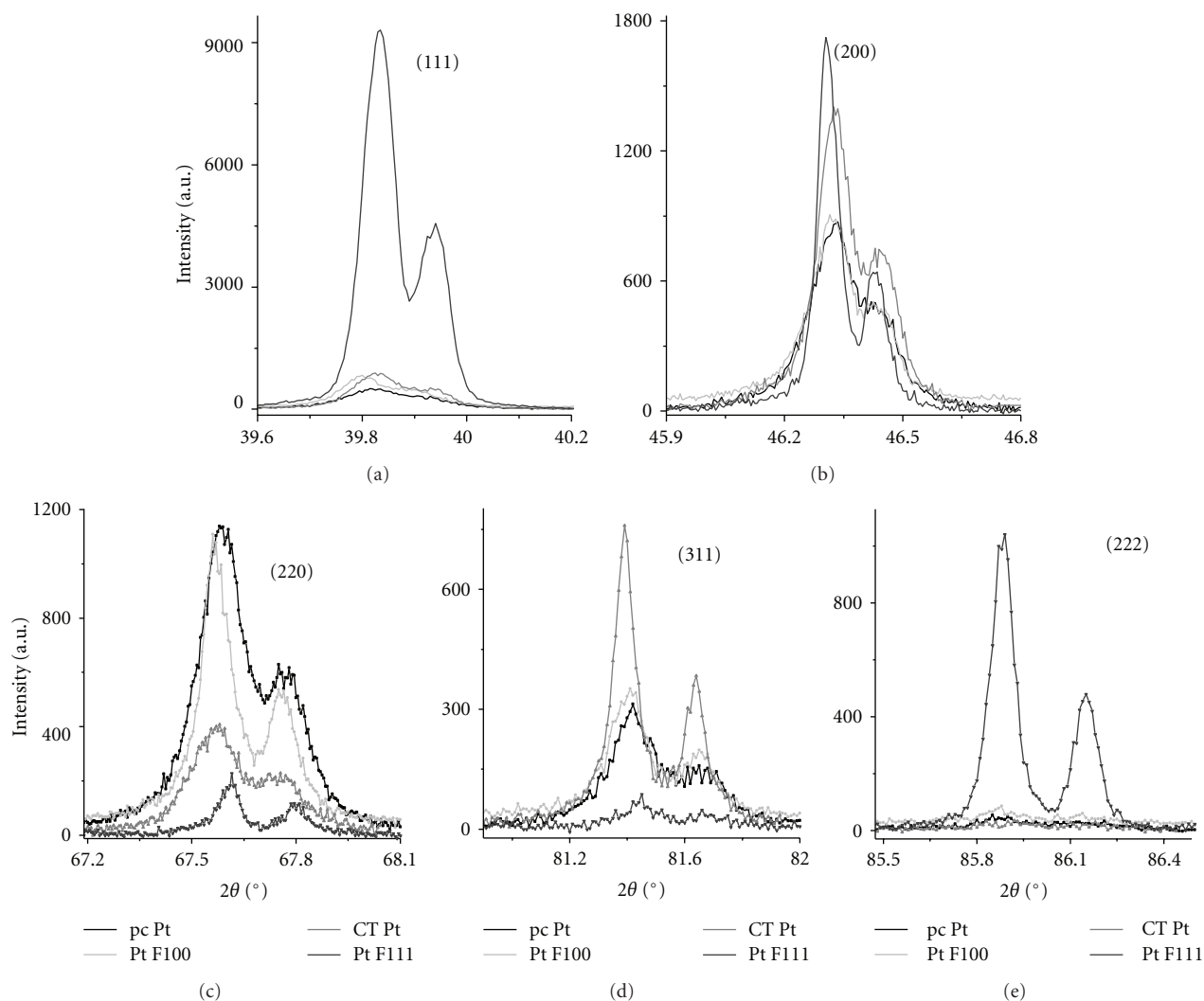


FIGURE 2: *Ex situ* X-ray powder diffraction pattern peaks (111), (200), (220), (311), and (222) for pc Pt (black lines), Pt F100 (light grey lines), CT Pt (grey lines), and Pt F111 (dark grey lines).

TABLE 1: Integrated intensities for pc Pt, CT Pt, Pt F100, and Pt F111 electrodes. The intensities are expressed as intensity $\times \Delta(2\theta)$ = counts \times degree.

Reflection	Pt bulk	pc	CT	F100	F111
(111)	100	108	155	129	1118
(200)	53	190	257	167	191
(220)	31	321	118	208	36
(311)	33	101	151	94	23
(222)	12	23	17	18	178

Note: in the case of Pt bulk, reflection (111) is referred as the intensity 100%.

Additionally, the contribution of (220) and (311) reflections is considerably lower than on the other samples. This is a confirmation that the faceting process is a process after which there is a strong decrease in the proportion of surface stepping, as observed in pc and CT platinum.

3.3. Electrocatalytic Activity Towards Methanol Oxidation.

TABLE 2: Weighted ratio for the reflections in pc Pt, CT Pt, Pt F100, and Pt F111 electrodes.

	Pt bulk	pc	CT	F100	F111
$I_w(200)/I_w(111)$	1.00	3.34	3.12	2.44	0.32
$I_w(311)/I_w(111)$	1.00	2.84	2.94	2.21	0.06
$I_w(220)/I_w(111)$	1.00	9.61	2.46	5.19	0.10
$I_w(111)/I_w(222)$	1.00	0.57	1.09	0.87	0.75

Note: we consider reflection (200) as a representative of reflection (100).

3.3.1. Linear Sweep Voltammetry in Methanol Acid Media. The first positive-going potential scan starting from 0.10 V up to 1.20 V for methanol electrooxidation on annealing Pt pc and electrofaceted platinum surfaces in 0.1 M methanol + 1 M sulfuric acid media are shown in Figure 3. A maximum current density is observed at ca. 0.85 V, above which the rate of methanol oxidation decreases due to platinum oxide formation (which also deactivates the surface). After the

TABLE 3: Integrated charge densities found under the current transients for methanol electrooxidation after 10 min. in oxygen-free 0.1 M methanol + 1 M sulphuric media on the studied platinum surfaces.

	Charge density ($\text{mC}\cdot\text{cm}^{-2}$)	
	0.60 V	0.70 V
Pt F100	<3	99.6
Pt F111	61.5	180.6
CT Pt	6.9	197.4
pc Pt	<3	97.7

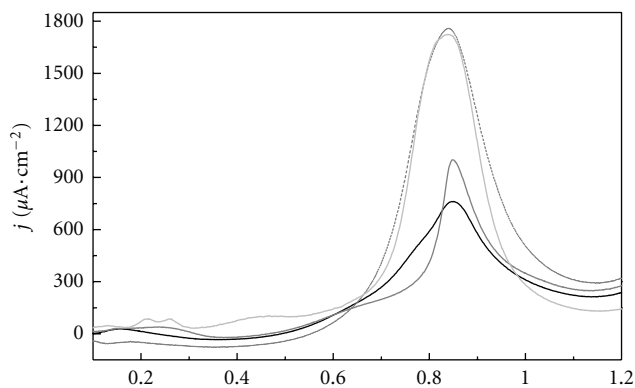


FIGURE 3: First positive-going potential scan for methanol oxidation run at 0.10 V s^{-1} between 0.10 and 1.20 V in oxygen-free 0.1 M methanol + 1 M sulphuric media on Pt F(111) (dotted gray lines); CT Pt (gray lines); Pt F(100) (dark gray lines) and annealed Pt (black lines).

pretreated procedure was applied in acid solution, the peak current density for Pt F111 depicts the greatest value, very similar to CT Pt. These values were more than 200% greater than that obtained on the untreated electrode. The electrocatalytic activity of pretreated surfaces was enhanced even after several cycles; contrary to the expected results on carbon monoxide poisoning induced on platinum surfaces.

3.3.2. Chronoamperometric Plots in Methanol Acid Media. Chronoamperometric curves were run for methanol oxidation on all platinum surfaces under two different constant potentials 0.60 V (not shown) and 0.70 V (Figure 4). All surfaces usually illustrate a typical diffusion-controlled current decay, but at 0.70 V, pc surfaces exhibit a first current increase at very short times. This fact is the result of a competitive process between adsorbed carbon monoxide and methanol oxidations with opposite contributions in the parallel oxidation mechanism, that is, the competition between the series and direct methanol oxidations. The pc platinum surface seems to be poisoned by a greater extent of carbon monoxide adsorbates. This effect is not observed at potentials lower than 0.70 V. The charge density at a fixed potential found under the current transients evidenced the real electrocatalytic activity of the surface. Table 3 represents the integration of the charge until 10 min (as comparison) for treated and untreated electrodes as a function of the

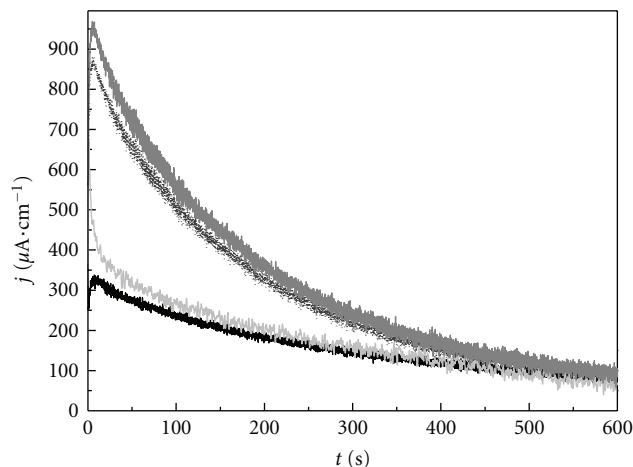


FIGURE 4: Chronoamperometric plots for methanol oxidation in oxygen-free 0.1 M methanol + 1 M sulphuric media at 700 mV on: pc Pt (black lines), Pt F100 (light grey lines), CT Pt (grey lines), and Pt F111 (dark grey lines).

potential. At 0.60 V, methanol oxidation did show a current contribution on the cathodic treated surface as well as on the Pt F111, not distinguished on the others surfaces. However, for 0.70 V, the charge densities found on the CT and Pt F111 surfaces are always higher than those of untreated platinum and other electrofaceted surfaces.

4. Discussion

The electrode composition plays an important role in the course of an electrocatalytic reaction, especially in the poison species removal. However, the surface morphology of technical electrodes is also important since it controls other factors associated with the formation and conversion of adsorbates. The relationship between the particle shape and the surface structure is of real importance in Electrocatalysis since its optimization is one of the best ways to enhance the selectivity and efficiency in the search of an adequate surface distribution for coadsorbate reactions.

Platinum crystallizes as a face centered cubic system with a cell parameter of 3.92 \AA . This system presents three base planes normal to the (111), (110), and (100) vectors in its three-dimensional crystal lattice. In fact the (110) plane is really $(110) = (111) \times (111)$, and not a true basal plane, so it is the first clue of an intrinsic atomic reconstruction. These three main vectors are the origin of the lowest Miller indices surfaces with a single type of symmetry. When the Miller indices increase, also does the complexity of the surface. For simplicity, these high Miller indices surfaces are considered as a combination of the different base planes in different proportions yielding terraces, monoatomic step and also *kinks*. The stepped surfaces present atomic terraces with a define orientation corresponding to a single base plane, separated by monoatomic steps of a certain symmetry. Lang et al. [28] proposed that the stepped surfaces have to be named taking the Miller indices of each terrace and step, with also the number of atomic files at the terrace. The

nomenclature for a stepped surface is $\mathbf{M}(s)[n(hkl) \times (h'k'l')]$ being \mathbf{M} the chemical symbol of the metal, n the number of atomic files at the terrace, the letter s between parenthesis indicates that it is a stepped surface and (hkl) and $(h'k'l')$ the Miller indices of the base planes that define the terraces and steps, respectively.

Methanol electrooxidation on platinum stepped or disordered surfaces is driven by two important factors; the total surface charge and the presence of water adjacent molecules in the aqueous phase. At the Pt(111) single crystal surface, the methanol molecule is located at a reactive position due to the formation of hydrogen bonds with a preadsorb water molecule [29]. It has been observed that the hydrogen bond strength of the methanol-water interaction at the (211) surfaces is larger than on (111), leading to a more exothermic adsorption for methanol [30]. However, the importance of the presence of preadsorbed water is demonstrated from the fact of the lower total exothermic condition for the cascade dehydrogenation (0.7 eV) at the Pt(111)/water interphase than at the Pt(111)/vacuum interphase [31, 32]. This fact is explained by the stabilization of the hydrogen bond in the complex and the weakened of the water/platinum interaction. Thus, adsorbed water molecules on platinum in acid media vibrates from 3500 to 3000–3100 cm^{-1} , but in the presence of adsorbate neighbours changes to a new vibration range due to the asymmetric stretching of the O-H bond at 3658 cm^{-1} [33]. Using *in situ* ATR-SEIRAS techniques it is demonstrated that water coexists with adsorbed carbon monoxide derived from methanol partial oxidation. Water is consumed during oxidation according to the adsorbed water and on-top carbon monoxide intensities. This is a strong confirmation that both water and carbon monoxide molecules coexists at the surface and that each species directly react from the surface promoting the further oxidation of other methanol molecules [34].

On the other hand, the change in the structure of the interfacial water structure caused by methanol adsorption is responsible of the difference between the experimental potential of zero charge (*pzc*) determined for the Pt(111-) CO interaction, 1.10 V, and the *pzc* estimated for the Pt(111-) water, 0.23 V [35]. Using these values it is possible to calculate mean angle between the water dipolar moment and the platinum surface. At room temperature *pzc*, diminishes from 7.85° for Pt(111-) water to 1.46° for Pt(111)-CO [35]. Chang and Weaver [36] have found that the water coadsorption at low coverages favours on Pt(111) the formation of bridge CO_{ads} . The vibration frequencies for linear and bridge geometries at high surface coverages by carbon monoxide are at least 20–30 cm^{-1} lower in the electrochemical environments than in UHV conditions. These environmental effects observed for the CO_{ads} bond suggests that the double layer effects are much more important than expected in the early stages of the anodic electrocatalytic reactions. Besides, the same important interaction between water and CO_{ads} has been also observed using *in situ* IRAS and STM techniques [37]. Adsorbed carbon monoxide on Pt(111) at 0.40 V shows a strong interaction with water molecules at the external layer retarding methanol oxidation to carbon dioxide, while its adsorption at 0.050 V reports lower values of oxidation

onset potentials. Moreover, it has been also reported that [29] methanol oxidation starts with the formation of a strong interaction leading to a hydrogen bond between the hydroxyl group of methanol with the water molecule. The first step of the reaction is the anchorage of a carbon-hydrogen bond focused towards the platinum surface. In this sense, our results clearly shows a larger activity in the case of the cathodic treated and the (111-) faceted platinum surfaces where the presence of stepped (111) planes are able to produce this strong interaction between partially dissociated water on (111) steps and adsorbed carbon monoxide from methanol partial oxidation on (100) terraces. The perfect combination of both effects of a proper crystal orientation at the steps and a distinct but adequate in the terraces are the theoretical concept in the catalysts design for the electrocatalytic oxidation reaction. The Pt F111 surface exhibit a good catalytic activity at lower potentials than CT Pt, but the latter exhibits larger charge densities at 0.70 V. This fact is the result of adsorbed hydroxyl species are produced on Pt F111 at lower potentials increasing then the catalytic activity at 0.60 V. However, since methanol posses a larger affinity towards the (100) oriented surfaces (as a consequence of its structural spatial conformation), at 0.70 V the stepped (111) \times (100) produced from the cathodic polarization method will exhibit a higher activity towards methanol oxidation. The relation between crystallographic orientation and oxidation catalytic activities are confirmed in the case of comparing Pt F100 and pc platinum surfaces.

5. Conclusions

(a) The electrochemical perturbation of platinum surfaces through *RSWPS* changes the surface relative distribution of crystallographic planes. This effect reaches the bulk of the metal up to the first layers of platinum, making possible the X-ray diffraction analysis.

(b) A net and practically single (111) plane contribution is obtained after obtaining a Pt F111 surface, however, for Pt F100, a stepped surface with a (220) plane main contribution is developed. The latter seems to be more an intermediate surface between pc and CT platinum. Moreover, the rearrangement produced at the CT platinum surface, yields facets with stepped planes equivalent to $[n(111) \times (100)]$.

(c) The electrocatalytic studies towards methanol oxidation conclude that both Pt F111 and CT Pt exhibit similar results and better than pc platinum with also a better tolerance upon surface poisoning. According to our knowledge water species are activated on (111) terraces at lower potentials than on (100) planes leading to adsorbed OH species with larger adsorption energies. Consequently, methanol adsorbates are not able to displace these ordered water species only enabling its surface diffusion from (111) terraces to (100) steps to finally adsorb there.

(d) The simple application of a constant cathodic current in the true hydrogen evolution region on pc platinum enhances the catalytic activity towards methanol

electrooxidation, since the stepped Pt[$n(111) \times (100)$] are morphologically more adequate to catalyse the reaction.

Acknowledgments

The authors are greatly acknowledged to the PDT Projects of the Education Ministerial Office. V. Díaz, R. Faccio, A.W. Mombrú, and C. F. Zinola are researchers at the Chemistry Area of PEDECIBA United Nations.

References

- [1] P. V. Pávlov and A. F. Jójlov, *Solid State Physics*, chapter 5 and 7, Mir, Moscow, Russia, 1987.
- [2] C. Sanchez and E. Leiva, "The NEMCA effect," in *Handbook of Fuel Cells*, W. Vielstich, H. A. Gasteiger, and A. Lamm, Eds., vol. 2, chapter 5, John Wiley & Sons, Chichester, UK, 2003.
- [3] N. M. Markoví and P. N. Ross Jr., "Surface science studies of model fuel cell electrocatalysts," *Surface Science Reports*, vol. 45, no. 4-6, pp. 117–229, 2002.
- [4] G. A. Somorjai, *Introduction to Surface Chemistry and Catalysis*, chapter 2, John Wiley & Sons, New York, NY, USA, 1994.
- [5] G. A. Somorjai, *Electrochemical Surface Science: Molecular Phenomena at Electrode Surfaces*, American Chemical Society, Washington, DC, USA, 1988.
- [6] A. J. Arvia, J. C. Canullo, E. Custidiano, C. L. Perdriel, and W. E. Triaca, "Electrochemical faceting of metal electrodes," *Electrochimica Acta*, vol. 31, no. 11, pp. 1359–1368, 1986.
- [7] S. Trasatti and O. A. Petrii, "Real surface area measurements in electrochemistry," *Journal of Electroanalytical Chemistry*, vol. 327, no. 1-2, pp. 353–376, 1992.
- [8] M. Fleischmann and B. W. Mao, "In situ X-Ray diffraction measurements of the surface structure of Pt in the presence of "weakly" adsorbed H," *Journal of Electroanalytical Chemistry*, vol. 247, no. 1-2, pp. 311–313, 1988.
- [9] H. P. Klug and L. E. Alexander, *X-Ray Diffraction Procedures for Polycrystalline and Amorphous Materials*, John Wiley & Sons, New York, NY, USA, 2nd edition, 1974.
- [10] L. A. Kibler, A. Cuesta, M. Kleinert, and D. M. Kolb, "In-situ STM characterization of the surface morphology of platinum single crystal electrodes as a function of their preparation," *Journal of Electroanalytical Chemistry*, vol. 484, no. 1, pp. 73–82, 2000.
- [11] D. M. Kolb, "Structure studies of metal electrodes by in-situ scanning tunneling microscopy," *Electrochimica Acta*, vol. 45, no. 15-16, pp. 2387–2402, 2000.
- [12] W. E. Triaca and A. J. Arvia, "The electrochemical faceting of metal surfaces: preferred crystallographic orientation and roughening effects in electrocatalysis," *Journal of Applied Electrochemistry*, vol. 20, no. 3, pp. 347–356, 1990.
- [13] A. S. Dakkouri and D. M. Kolb, "Reconstruction of gold surfaces," *Interfacial Electrochemistry*, chapter 10, Marcel Dekker, New York, NY, USA, 1999.
- [14] N. Tian, Z. Y. Zhou, S. G. Sun, Y. Ding, and L. W. Zhong, "Synthesis of tetrahedral platinum nanocrystals with high-index facets and high electro-oxidation activity," *Science*, vol. 316, no. 5825, pp. 732–735, 2007.
- [15] A. J. Arvia, R. C. Salvarezza, and W. E. Triaca, "The development of metal overlayers with smooth and rough topographies," *Electrochimica Acta*, vol. 34, no. 8, pp. 1057–1071, 1989.
- [16] A. Visintín, J. C. Canullo, W. E. Triaca, and A. J. Arvia, "Changes in real surface area, crystallographic orientation and morphology of platinum electrodes caused by periodic potential treatments: phenomenological approach," *Journal of Electroanalytical Chemistry*, vol. 239, no. 1-2, pp. 67–89, 1988.
- [17] W. E. Triaca, T. Kessler, J. C. Canullo, and A. J. Arvia, "Study of the optimal conditions for the development of preferred oriented platinum surfaces by means of fast square wave potential perturbations," *Journal of the Electrochemical Society*, vol. 134, no. 5, pp. 1165–1172, 1987.
- [18] A. C. Chialvo, W. E. Triaca, and A. J. Arvia, "Changes in the electrochemical response of noble metals produced by square-wave potential perturbations. A new technique for the preparation of reproducible electrode surfaces of interest in electrocatalysis," *Journal of Electroanalytical Chemistry*, vol. 146, no. 1, pp. 93–108, 1983.
- [19] J. Gómez, L. Vázquez, A. M. Baró et al., "Surface topography of (100)-type electro-faceted platinum from scanning tunnelling microscopy and electrochemistry," *Nature*, vol. 323, no. 6089, pp. 612–614, 1986.
- [20] L. Vázquez, J. Gómez, A. M. Baró et al., "Scanning tunneling microscopy of electrochemically activated platinum surfaces. A direct ex-situ determination of the electrode nanotopography," *Journal of the American Chemical Society*, vol. 109, no. 6, pp. 1730–1733, 1987.
- [21] C. Bello and C. F. Zinola, "Crystallographic rearrangement of platinum induced by square wave potentials," *Journal of Colloid and Interface Science*, vol. 258, no. 2, pp. 259–265, 2003.
- [22] C. Lamy, J. M. Leger, J. Clavilier, and R. Parsons, "Structural effects in electrocatalysis. A comparative study of the oxidation of CO, HCOOH and CH₃OH on single crystal Pt electrodes," *Journal of Electroanalytical Chemistry*, vol. 150, no. 1-2, pp. 71–77, 1983.
- [23] M. T. M. Koper, S. C. S. Lay, and E. Herrero, *Fuel Cell Catalysis: A Surface Science Approach*, chapter 6, John Wiley & Sons, New York, NY, USA, 2009.
- [24] J. Shin and C. Korzenicwski, "Infrared spectroscopic detection of CO formed at step and terrace sites on a corrugated electrode surface plane during methanol oxidation," *Journal of Physical Chemistry*, vol. 99, no. 11, pp. 3419–3422, 1995.
- [25] A. V. Tripković and K. D. Popović, "Oxidation of methanol on platinum single crystal stepped electrodes from [110] zone in acid solution," *Electrochimica Acta*, vol. 41, no. 15, pp. 2385–2394, 1996.
- [26] T. H. M. Housmans and M. T. M. Koper, "Methanol oxidation on stepped Pt[$n(111) \times (110)$] electrodes: a chronoamperometric study," *Journal of Physical Chemistry B*, vol. 107, no. 33, pp. 8557–8567, 2003.
- [27] C. Dong, "PowderX: windows-95-based program for powder X-Ray diffraction data processing," *Journal of Applied Crystallography*, vol. 32, no. 4, p. 838, 1999.
- [28] B. Lang, R. W. Joyner, and G. A. Somorjai, "Low energy electron diffraction studies of high index crystal surfaces of platinum," *Surface Science*, vol. 30, no. 2, pp. 440–453, 1972.
- [29] C. Hartnig and E. Spohr, "The role of water in the initial steps of methanol oxidation on Pt(1 1 1)," *Chemical Physics*, vol. 319, no. 1–3, pp. 185–191, 2005.
- [30] C. Hartnig, J. Grimmering, and E. Spohr, "The role of water in the initial steps of methanol oxidation on Pt(2 1 1)," *Electrochimica Acta*, vol. 52, no. 6, pp. 2236–2243, 2007.
- [31] R. Paul and S. J. Paddison, "Variational methods for the solution of the Ornstein-Zernicke equation in inhomogeneous systems," *Physical Review E*, vol. 67, no. 1, part 2, Article ID 161081, 11 pages, 2003.
- [32] Y. Okamoto, O. Sugino, Y. Mochizuki, T. Ikeshoji, and

- Y. Morikawa, "Comparative study of dehydrogenation of methanol at Pt(1 1 1)/water and Pt(1 1 1)/vacuum interfaces," *Chemical Physics Letters*, vol. 377, no. 1-2, pp. 236–242, 2003.
- [33] H. Shiroishi, Y. Ayato, K. Kunimatsu, and T. Okada, "Study of adsorbed water on Pt during methanol oxidation by ATR-SEIRAS (surface-enhanced infrared absorption spectroscopy)," *Journal of Electroanalytical Chemistry*, vol. 581, no. 2, pp. 132–183, 2005.
- [34] A. Cuesta, H. Shiroishi, Y. Ayato, K. Kunimatsu, and T. Okada, "Comments on the paper by H. Shiroishi, Y. Ayato, K. Kunimatsu and T. Okada entitled "Study of adsorbed water on Pt during methanol oxidation by ATR-SEIRAS (surface-enhanced infrared absorption spectroscopy)" [J. Electroanal. Chem. 581 (2005) 132]," *Journal of Electroanalytical Chemistry*, vol. 587, no. 2, pp. 329–332, 2006.
- [35] A. Cuesta, "Measurement of the surface charge density of CO-saturated Pt(1 1 1) electrodes as a function of potential: the potential of zero charge of Pt(1 1 1)," *Surface Science*, vol. 572, no. 1, pp. 11–22, 2004.
- [36] S. C. Chang and M. J. Weaver, "Coverage- and potential-dependent binding geometries of carbon monoxide at ordered low-index platinum- and rhodium-aqueous interfaces: comparisons with adsorption in corresponding metal-vacuum environments," *Surface Science*, vol. 238, no. 1–3, pp. 142–162, 1990.
- [37] K. Yoshimi, M.-B. Song, and M. Ito, "Carbon monoxide oxidation on a Pt(111) electrode studied by in-situ IRAS and STM: coadsorption of CO with water on Pt(111)," *Surface Science*, vol. 368, no. 1–3, pp. 389–395, 1996.

Research Article

Some Applications of Bayes' Rule in Probability Theory to Electrocatalytic Reaction Engineering

Thomas Z. Fahidy

Chemical Engineering Department, University of Waterloo, 200 University Avenue West, Waterloo, ON, Canada N2L 3G1

Correspondence should be addressed to Thomas Z. Fahidy, tfahidy@engmail.uwaterloo.ca

Received 7 February 2011; Accepted 25 April 2011

Academic Editor: Carlos F. Zinola

Copyright © 2011 Thomas Z. Fahidy. This is an open access article distributed under the Creative Commons Attribution License, which permits unrestricted use, distribution, and reproduction in any medium, provided the original work is properly cited.

Bayesian methods stem from the principle of linking prior probability and conditional probability (likelihood) to posterior probability via Bayes' rule. The posterior probability is an updated (improved) version of the prior probability of an event, through the likelihood of finding empirical evidence if the underlying assumptions (hypothesis) are valid. In the absence of a frequency distribution for the prior probability, Bayesian methods have been found more satisfactory than distribution-based techniques. The paper illustrates the utility of Bayes' rule in the analysis of electrocatalytic reactor performance by means of four numerical examples involving a catalytic oxygen cathode, hydrogen evolution on a synthetic metal, the reliability of a device testing the quality of an electrocatalyst, and the range of Tafel slopes exhibited by an electrocatalyst.

1. Introduction

In a comprehensive overall treatment of the subject matter, Bockris and Khan [1] discuss electrocatalysis with respect to various physicochemical properties of substance and surface, for example, exchange current density, work function, bond strength, metal complexes, trace elements adatom effects, enzymatic catalysis, poisons, crystal face effects, and so forth, under the aegis of "phenomenological electrode kinetics". In the domain of ERE, the assessment of electrocatalyst (EC) performance also includes additional parameters related to catalyst preparation (i.e., possible defectiveness in specimens), cell construction, and human factors affecting reactor output.

This paper was written with this dichotomy in mind, from the vantage point of the electrochemical engineer, whose responsibilities dealing with production quota, the possibility of (temporary) reactor breakdown, safety, and environmental considerations reach well beyond purely scientific quantities. Major tools for dealing with these responsibilities are provided by probability-based (e.g., statistical) methods. Bayes' rule is one such tool, whose specific application to scenarios with EC is the subject of this article.

2. Brief Theory

Following a concise definition [2] for the purposes of this paper, Bayes' rule for two events may be expressed as

$$P(A/B) = \frac{P(B/A)P(A)}{P(B)}, \quad (1)$$

where $P(A/B)$ is the probability of event A occurring if event B has already occurred, and

$$P(B) = P(B/A)P(A) + P(B/A')P(A'), \quad (2)$$

which is the probability of event B occurring, given the conditional probabilities (likelihoods) $P(B/A)$ relating it to event A and $P(B'/A)$ relating it to its opposite event A' . In an EC reactor a case for Bayes' rule would exist, for instance, when the loss of effectiveness in an EC may or may not be due to premature detachment of the catalytic layer. If A is the event of detachment and B is the event of deterioration (demise) of the EC, then B/A would be the event of demise due to layer detachment, A' the event of a nondetachment cause of deterioration, and B/A' the event of deterioration due to a nondetachment cause. In terms of event probabilities, (1) yields the probability $P(A/B)$ that

TABLE 1: Postulated distribution pattern of 137 failure occurrences over a fixed time period in three independently operating (hypothetical) electrolytic plants using identical catalytic oxygen cathodes (Application 1).

Source of failure	Number of cathode failures over a fixed period of operation		
	Plant 1 (B_1)	Plant 2 (B_2)	Plant 3 (B_3)
A_1 : Catalyst surface area ⁽¹⁾	12	14	10
A_2 : Pore volume ⁽²⁾	7	8	9
A_3 : Binder content ⁽³⁾	9	5	7
A_4 : Catalyst content ⁽⁴⁾	6	4	5
A_5 : Human error ⁽⁵⁾	14	11	16
Total number of failures	48	42	47

⁽¹⁾ Electrolytic carbon type P33: specific surface area is less than stipulated 1000 m²/g.

⁽²⁾ Electrolytic carbon type P33: specific pore volume is less than stipulated 2.3 cm³/g.

⁽³⁾ PTFE binder content in electrode layer is less than stipulated 10%.

⁽⁴⁾ CoTAA (dibenzotetraazaannulen cobalt II) catalyst content on carbon is less than stipulated 15%.

⁽⁵⁾ Careless stack assemblage and general operation.

deterioration would occur as a result of layer detachment and not due to a different cause, for example, the decomposition of a binder, or the splitting of the electrode frame, and so forth. If A_1, A_2, \dots, A_n are mutually exclusive and exhaustive events, (1) and (2) are generalized to

$$P(A_k/B) = \frac{P(B/A_k)P(A_k)}{\sum_{k=1}^n P(B/A_k)P(A_k)}, \quad (3)$$

taking into account all possible causes of deterioration (the denominator of (3) is also known as the total probability theorem [3]). A lucid discussion of the merits of Bayesian methods by Bulmer [4] and a short set-theoretic proof by Arnold [5] are amply complemented by a sizeable literature on probability and statistics dealing with the subject matter.

Specific exploratory applications to electrochemical processes and technology at various levels of complexity are relatively recent [6–10]. The paper illustrates, via four independent examples, the (potential) utility of Bayes' rule in ERE. Due to the currently insufficient availability of appropriate experimental information in the research literature, hypothetical numerical data are employed with the sole purpose of indicating the course of analysis to which appropriate experimental data could be subjected. With the intention of stimulating at least a modest appetite at present for Bayes' rule, the illustrations are realistic but uncomplicated on purpose.

3. Illustration of the Utility of Bayes' Rule for ERE

3.1. Application No. 1: Estimating the Most Likely Location of Oxygen-Cathode Failure. Table 1 contains the failure-frequency map of identical oxygen cathodes, assumed to possess the structure described by Wiesener and Ohms [11]. These mutually independent failures are stipulated to have occurred in three independently operating electrochemical plants. Denoting A_1, A_2, \dots, A_5 as the source-of-failure events

and B_1, B_2, B_3 as the plant location events, the probability of failure arising, for example, from human error is given by

$$\begin{aligned} P(A_5) &= \sum_{k=1}^3 P(A_5/B_k)P(B_k) = \frac{14}{48} \frac{48}{137} + \frac{11}{42} \frac{42}{137} + \frac{16}{47} \frac{47}{137} \\ &= \frac{41}{137} = 0.2993, \end{aligned} \quad (4)$$

which is about 30%, and Bayes' rule:

$$P(B_j/A_5) = \frac{P(A_5/B_j)P(B_j)}{P(A_5)}, \quad j = 1, 2, 3, \quad (5)$$

yields the probability of failure in any one of the three plants caused by human error: $P(B_1/A_5) = 14/41 = 0.3415$; $P(B_2/A_5) = 11/41 = 0.2683$; $P(B_3/A_5) = 16/41 = 0.3802$. Thus, (next time) failure due to human error can be expected to be the least likely in Plant 2 and the most likely in Plant 3, although not significantly so with respect to Plant 1. The entire set $P(B_k/A_j)$, $j = 1, 2, 3$, $k = 1, 2, \dots, 5$ of likelihoods, obtained in a manner similar to (5) is shown in Table 2. The relatively largest failure probability, about 43%, can be expected in Plant 1 on account of insufficient PTFE binder content in the electrode layer. The contents of Table 2 would guide plant operators in attempting to eliminate (or at least to reduce the extent of) the most likely cause that can be expected in each plant. They would also indicate what cautionary measures would be advisable in the design of future plants.

3.2. Application No. 2: The Effect of Prior Probability on the Anticipated Viability of an EC-Generated H₂ Evolution Process. A recently developed electrocatalyst for a hydrogen evolution process, made up of certain synthetic metals, is expected to possess an exchange current $i_0 \approx 100 \mu\text{A}/\text{cm}^2$ at design operating conditions in a pilot scale electrolyzer. Inspection of Trasatti's [12] "volcano plot" [13, 14] suggests that its catalytic property would presumably fall between that of iridium and gold. It is further anticipated that the novel

TABLE 2: The complete set of probabilities computed via (5) in Application 1.

Source-of-failure events	$P(B_j/A_k)$		
	B_1	B_2	B_3
A_1	0.3333	0.3889	0.2778
A_2	0.2917	0.3333	0.3750
A_3	0.4286	0.2381	0.3333
A_4	0.4000	0.2667	0.3333
A_5	0.3415	0.2683	0.3902

TABLE 3: The effect of prior probability $P(B)$ on decision possibilities related to a new CE (Application 2).

$P(B)\%$	$P(B/A)\%$	$P(B/A')\%$
20	67.4	2.5
40	84.6	6.3
60	92.5	13.2
70	95.1	19.1
80	97.1	28.8
90	98.7	47.6

$P(B/A)$: the probability that a CE will be deemed acceptable upon the Q_2 test, if the results of the Q_1 test were positive.

$P(B/A')$: the probability that a CE will be deemed acceptable upon the Q_1 test, even if the results of the Q_1 test were negative.

catalyst would be less expensive than Ir and Au, it would exhibit good dimensional/geometric stability as well as resistance to parasitic reactions due to possible contamination, and resistance to possible nonuniformity in current distribution. The design team postulates that if, on a pilot-plant scale, electrode specimens will show no loss in catalytic activity up to the passage of $Q_1 \approx 600 \text{ kAh/dm}^2$ electric charge per unit area, then there should exist a priori chance that a catalyst-carrying electrode (CCE), selected randomly from a lot of identically prepared specimens, can sustain its catalytic activity, at an acceptable level, up to the passage of $Q_2 \approx 1200 \text{ kAh/dm}^2$. During the Q_1 tests, 91% of the electrodes were found to be acceptable, but 89% of electrodes, which later failed the Q_2 tests, did not perform in a satisfactory manner. The design team (i) would proceed to consider commercial-scale implementation if there is at least a 95% chance that a survivor of the Q_1 -test would keep its catalytic activity up to the passage of Q_2 , (ii) would abandon further research if favourable results were obtained in only one-fifth or less of the Q_1 tests.

The set of events of interest here, involving a randomly selected CCE, is defined as follows:

A : results obtained during the passage of Q_1 are positive,

A' : results obtained during the passage of Q_1 are negative,

B : the CCE is acceptable,

B' : the CCE is unacceptable,

A/B : Q_1 -results were positive for an acceptable CCE,

A/B' : Q_1 -results were positive for an unacceptable CCE,

A'/B : Q_1 -results were negative for an acceptable CCE,

A'/B' : Q_1 -results were negative for an unacceptable CCE,

B/A : a CCE which showed positive Q_1 -test results is found acceptable,

B/A' : a CCE which showed negative Q_1 -test results is found acceptable.

Consequently, the stipulations can be expressed in terms of their probabilities as follows: $P(A/B) = 0.91$; $P(A'/B') = 0.89$; $P(A/B') = 1 - P(A'/B') = 0.11$. Bayes' rule yields, therefore,

$$P(B/A) = \frac{0.91P(B)}{0.91P(B) + 0.11[1 - P(B)]}, \quad (6)$$

$$P(B/A') = \frac{0.09P(B)}{0.09P(B) + 0.89[1 - P(B)]}.$$

Here, $P(B)$ is the prior probability of a CCE being acceptable. Its value, if not known experimentally, would be a matter of the designers' judgment. Table 3 indicates that in order to satisfy the $P(B/A) \geq 95\%$ and $P(B/A') \geq 20\%$ decision criteria simultaneously, the prior probability of a CCE passing the Q_2 -test would have to be somewhat higher than 70%. If the abandonment criterion were raised to a stricter $P(B/A') \geq 25\%$ probability, $P(B)$ would have to be at least 77% for satisfying the two continuance conditions. Such results provide the design team with important knowledge for establishing proper testing protocols.

3.3. Application 3: Probing Claims Regarding the Reliability of a Catalyst Tester. A device for testing defects in a certain electrocatalyst (EC) is envisaged to be advertised by the catalyst producer, claiming that it is 97% reliable if the EC is defective, and 99% reliable when it is flawless. Independently from any testing device and based upon earlier experience, 4% of said EC may be expected to be defective upon delivery. In order to ascertain the true reliability of the device, Bayes' rule is applied to basic event set A : the EC is defective; A' : the EC is flawless; B : the EC is tested to be defective; B' : the EC is tested to be flawless, equipped with the full set of conditional events of interest here with their probabilities:

B/A : EC is (known to be) defective, and tested defective, $P(B/A) = 0.97$,

B'/A : EC is (known to be) defective, but tested flawless, $P(B'/A) = 1 - P(B/A) = 0.03$,

B/A' : EC is (known to be) flawless, but tested defective, $P(B/A') = 1 - P(B'/A') = 0.01$,

B'/A' : EC is (known to be) flawless, and tested flawless, $P(B'/A') = 0.99$.

The probabilities of events to be computed via Bayes' rule, shown in Table 4, point to the (vexingly) high possibility of rejecting flawless EC's (about 20%) and the (vexingly) low possibility of identifying defective EC's (about 80%) when the tester indicates defectiveness. These findings, hidden by the advertisement without Bayes' rule, should discourage its adoption for routine use.

3.4. Application 4: Probing Claims Regarding Tafel Slopes in an Electrocatalytic Oxidation of Methanol Process Envisaged for Fuel Cells. This example is motivated by an experimental study of Pt:Mo dispersed catalysts (PMDCs) for the electro-oxidation of methanol in acid medium [15], assuming that a

TABLE 4: Probabilities of flawlessness/defectiveness expected from an EC tester (Application No. 3).

Event	Bayes' rule	Event probability
EC tested defective, but found flawless	$P(A'/B) = \frac{P(B/A')P(A')}{P(B/A')P(A') + P(B/A)P(A)}$	0.1983
EC tested flawless, and found flawless	$P(A'/B') = \frac{P(B'/A')P(A')}{P(B'/A')P(A') + P(B'/A)P(A)}$	0.9987
EC tested flawless, but found defective	$P(A/B') = \frac{P(B'/A)P(A)}{P(B'/A)P(A) + P(B'/A')P(A')}$	0.0013
EC tested defective, and found defective	$P(A/B) = \frac{P(B/A)P(A)}{P(B/A)P(A) + P(B/A')P(A')}$	0.8017

$$P(A/B') + P(A'/B') = P(A/B) + P(A'/B) = 1; P(A) = 0.04; P(A') = 1 - 0.04 = 0.96.$$

different research team claims in a new experimental catalyst development program a 65–70 mV/dec Tafel slope range at low current densities, and a 255–265 mV/dec at high current densities (in contrast with the 30–35 and 230–250 mV/dec ranges, resp. in the cited study). The polarization method chosen for investigating the claim is assumed to be 89% reliable when the claim cannot be verified and 99.5% reliable when the claim can be verified. Defining events A : the PMDC exhibits Tafel slopes below the claimed ranges and B : the PMDC is found to exhibit Tafel slopes below the claimed ranges, the complementary events A' : the PMDC exhibits Tafel slopes within the claimed ranges and B' : the PMDC is found to exhibit Tafel slopes within the claimed ranges establish the basis for applying Bayes' theorem. Following the pattern shown by the previous applications, the conditional probabilities are $P(B'/A) = 0.11$, $P(B/A') = 0.005$, $P(B/A) = 0.89$ and $P(B'/A') = 0.995$.

The research team is assumed to report that 96% of the new PMDC possess the claimed Tafel slope ranges; Bayes' theorem yields $P(A'/B) = 0.1188$; $P(A/B') = 0.0046$; $P(A'/B') = 0.9954$; $P(A/B) = 0.8812$. The about 12% probability that a new catalyst complies with the claim although the polarization experiment indicates otherwise raises at least a reasonable doubt about the claim or the reliability of the experimental procedure, in spite of the satisfactory $P(A/B')$ and $P(A'/B')$ values.

4. Discussion and Final Remarks

Perhaps the most striking feature of Bayes' rule is the amount of information that can be gleaned from a few uncomplicated probability ratios (the fact that Bayesian methods are at present more than two hundred years old is equally impressive). Within the Bayesian framework, a prior event probability is updated to a posterior probability of that event by means of a likelihood. The latter provides the (conditional) probability of corroborating the a-priori stated hypothesis; this aspect is numerically illustrated in the Appendix.

The examples presented in this paper provide a small "window" to the realm of Bayesian methods whose further exploration in electrochemical science and engineering requires further work. Bayes' rule is just one of many other mathematical devices of applied probability theory with potential interest to the field.

Appendix

Bayes' Rule: Short Analysis and Illustration via Application No. 3

Let AB and BA denote the combined event of both events A and B occurring, the order of occurrence being immaterial. The veracity of the statement $P(AB) = P(BA) = P(B/A)P(A) = P(A/B)P(B)$ and of (1) immediately follows. Accounting for complementary events A' and B' the (total) probabilities $P(A) = P(A/B)P(B) + P(A/B')P(B')$ and $P(B) = P(B/A)P(A) + P(B/A')P(A')$ are mirror images of each other. In Application No. 3 $P(B/A)P(A) = (0.97)(0.04) = 0.0388$ is the posterior probability of an EC being defective vis-à-vis prior probability. $P(A) = 0.04$. Similarly, $P(B/A')P(A') = (0.01)(0.96) = 0.0096$ is the posterior probability of EC-defectiveness vis-à-vis prior complementary probability $P(A') = 0.96$; the total probability of event B is $0.04 + 0.0096 = 0.0484$. Bayes' rule yields $P(A/B) = 0.0388/0.0484 = 0.8017$, that is the posterior probability that an EC tested defective is, indeed, defective. It is appreciably less than the claimed (i.e. prior) probability of 0.97.

Acknowledgments

Utilities provided by the University of Waterloo and the Natural Sciences and Engineering Research Council of Canada (NSERC) are gratefully acknowledged.

References

- [1] J. O'M. Bockris and S. U. M. Khan, *Surface Electrochemistry*, Plenum, New York, NY, USA, 1993.
- [2] R. Porkess, *Collins Internet-Linked Dictionary of Statistics*, Harper Collins College, Glenview, Ill, USA, 2nd edition, 2005.
- [3] E. B. Manoukian, *Modern Concepts and Theorems of Mathematical Statistics*, Springer, New York, NY, USA, 1986.
- [4] M. G. Bulmer, *Principles of Statistics*, Dover, New York, NY, USA, 2nd edition, 1979.
- [5] S. F. Arnold, *Mathematical Statistics*, Prentice Hall, Englewood Cliffs, NJ, USA, 1990.
- [6] T. Z. Fahidy, "On the utility of certain decision theory techniques in electrochemical process design," in *Current Topics in Electrochemistry*, vol. 7, pp. 119–123, Research Trends, Trivandrum, India, 2000.

- [7] T. Z. Fahidy, "An application of Bayesian risk theory to electrochemical processes," *Electrochimica Acta*, vol. 49, no. 9-10, pp. 1397-1401, 2004.
- [8] T. Z. Fahidy, "Bayesian updating of electrochemical process parameters via natural conjugate probability distributions," *Electrochimica Acta*, vol. 49, no. 27, pp. 5013-5021, 2004.
- [9] T. Z. Fahidy, "Probabilistic methods in the analysis of certain electrochemical systems," in *Recent Research Developments in Electrochemistry*, S. G. Pandalai, Ed., vol. 6, pp. 116-117, Transworld Research Network, Trivandrum, India, 2003.
- [10] T. Z. Fahidy, "Electrochemical applications of net-benefit analysis via Bayesian probabilities," *Journal of Applied Electrochemistry*, vol. 37, no. 6, pp. 747-752, 2007.
- [11] K. Wiesener and D. Ohms, "Electrocatalysis for environmentally orientated electrochemical processes and environmental protection," in *Environmental Oriented Electrochemistry*, C. A. C. Sequeira, Ed., p. 694, Elsevier, Amsterdam, The Netherlands, 1994.
- [12] S. Trasatti, "Work function, electronegativity, and electrochemical behaviour of metals. III. Electrolytic hydrogen evolution in acid solutions," *Journal of Electroanalytical Chemistry*, vol. 39, no. 1, pp. 163-184, 1972.
- [13] J. O'M. Bockris and S. U. M. Khan, loc. cit., Section 3.14.3, Fig. 3.23, p. 268.
- [14] J. O'M. Bockris and S. U. M. Khan, loc. cit., Section 3.21.6, Fig. 3.31, p. 293.
- [15] A. Oliveira Neto, J. Perez, W. T. Napporn, E. A. Ticianelli, and E. R. Gonzalez, "Electrocatalytic oxidation of methanol: study with Pt:Mo dispersed catalysts," *Journal of the Brazilian Chemical Society*, vol. 11, no. 1, pp. 39-43, 2000.

Research Article

Chiral Recognition of Amino Acids by Magneto-electrodeposited Cu Film Electrodes

Iwao Mogi and Kazuo Watanabe

Institute for Materials Research, Tohoku University, Katahira, Aoba-ku, Sendai 980-8577, Japan

Correspondence should be addressed to Iwao Mogi, mogi@imr.tohoku.ac.jp

Received 24 December 2010; Accepted 30 March 2011

Academic Editor: Carlos F. Zinola

Copyright © 2011 I. Mogi and K. Watanabe. This is an open access article distributed under the Creative Commons Attribution License, which permits unrestricted use, distribution, and reproduction in any medium, provided the original work is properly cited.

Chiral behavior of magneto-electrodeposited (MED) Cu film electrodes was investigated for the electrochemical reactions of amino acids. The Cu films were electrodeposited under a magnetic field of 5 T perpendicular to the electrode surface. Such MED Cu films were employed as an electrode, and cyclic voltammograms were measured for the electrochemical reactions of several kinds of amino acids. Chiral behavior was clearly observed as oxidation current difference between the enantiomers of alanine, aspartic acid, and glutamic acid. The MED film electrodes with the thickness of 50~500 nm exhibited such chiral behavior, and their surface morphologies had network structures, which could be induced by the micro-MHD effect.

1. Introduction

When a magnetic field is imposed to an electrodeposition process (magneto-electrodeposition), the Lorentz force acting on the faradaic current causes convection of the electrolytic solution. This is well known as the magnetohydrodynamic (MHD) effect [1, 2]. The MHD effect leads to spiral structures in the two-dimensional growth of magneto-electrodeposited (MED) metals [3–6] and conducting polymers [7], and the three-dimensional helical structures in silicate membrane growth [8]. Thus, magneto-electrodeposition has the potential to produce chiral structures. This is called as magneto-electrochemical chirality. Control of chirality is one of the most significant subjects in biochemistry, and considerable effort has been devoted in exploring chiral catalysts. If the chiral structures can be formed in nanometer scales on the MED films, such film surfaces would serve as an enantioselective catalyst.

Aogaki proposed the micro-MHD effect in the electrodeposition under the magnetic fields parallel to the faradaic current and perpendicular to the electrode surfaces [9]. In electrodeposition processes, nonequilibrium fluctuation produces a lot of humps on the deposit surfaces. The faradaic current around such humps is not parallel to the magnetic

field so that the Lorentz force could cause vortex-like convection in the local areas around the humps. The micro-MHD effect was observed in the circular structures on the MED Cu film surfaces [9] and the network structures in the Ni-alumina composite films [10]. The micro-MHD convection breaks the symmetry of mass transfer around the humps, and such symmetry breaking might lead to the formation of chiral structures on the deposit surfaces [11].

We tried the magneto-electrodeposition of Ag films and employed them as modified electrodes. The MED Ag film electrodes were found to exhibit different oxidation currents between the enantiomers of glucose and cysteine [12, 13]. To demonstrate the universality of magneto-electrochemical chirality, it is necessary to examine the chiral behaviors of the MED films of various kinds of metals. Copper electrodes exhibit electrocatalytic behaviors for the electro-oxidation of alcohols and amino acids in alkaline aqueous solutions [14, 15]. The electrocatalytic reactions are sensitive to the surface structure of the electrode through specific adsorption of reactant molecules. If the reactant has chirality, its electrocatalytic reaction could be sensitive to the chirality of the electrode surface. In this paper, we report the magneto-electrodeposition of Cu films and their characteristic chiral electrode behaviors for amino acids.

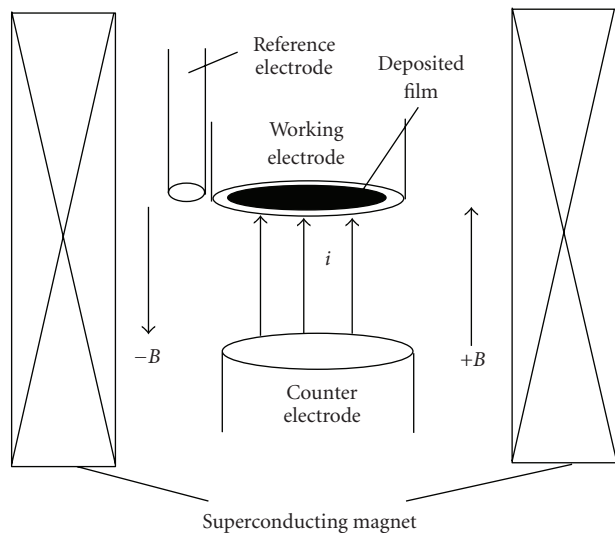


FIGURE 1: Schematic representation of magneto-electrodeposition in a superconducting magnet. Magnetic fields B are applied to parallel (+) or antiparallel (-) to faradaic currents, and they are perpendicular to the electrode surface.

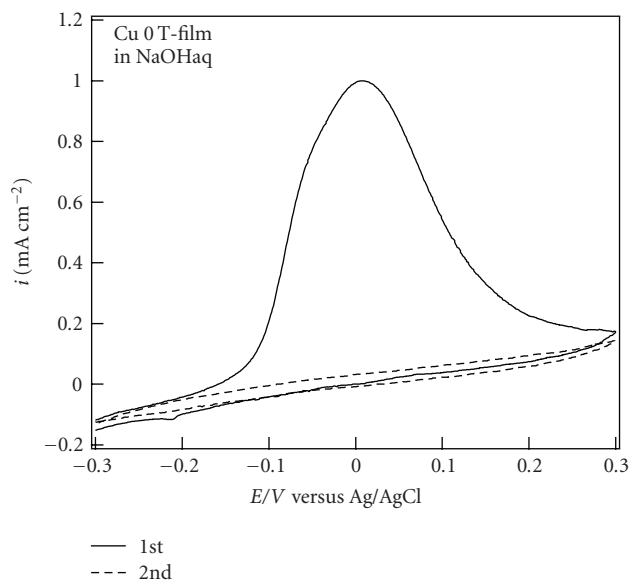


FIGURE 2: CVs of the Cu 0T-film electrode in a 0.1 M NaOH aqueous solution. The 1st sweep (solid line) corresponds to the pretreatment of the Cu film electrode, and the 2nd sweep (dashed line) represents the background current. The potential sweep rate was 10 mV s^{-1} .

2. Experimental

All chemicals were reagent grade and were used as received. For electrochemical experiments, a conventional system with the following three electrodes was employed: a polycrystalline Pt disc working electrode with a diameter of 3 mm, a Cu or Pt plate counter electrode, a Ag | AgCl | NaCl (3 M ($M = \text{mol dm}^{-3}$)) reference electrode. A potentiostat (Princeton Applied Research model 263A) was used for all the electrochemical experiments.

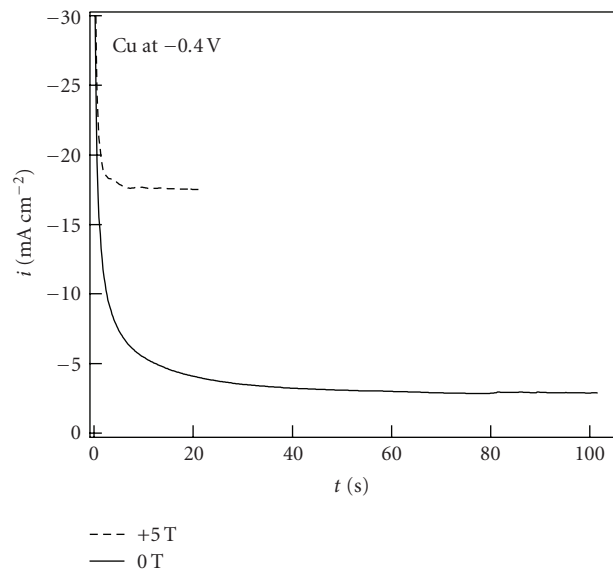


FIGURE 3: Current-time curves during the Cu electrodeposition in 0 T and +5 T.

Cu electrodeposition was conducted in a 50 mM CuSO_4 aqueous solution containing 0.5 M H_2SO_4 . The Cu films were formed on the Pt working electrode by the potentiostatic electrodeposition at a potential of -0.4 V . The film thickness was controlled by a passing charge, and the thickness could be approximately estimated from the density of Cu (8.93 g cm^{-3}), the electrode area and the passing charge. The usual film thickness was c.a. 150 nm at the passing charge of 0.4 C cm^{-2} .

Figure 1 shows a schematic representation of the magneto-electrodeposition. The electrochemical cell was placed at the bore center in a cryocooled superconducting magnet (Sumitomo Heavy Industries Ltd.), which is installed in the High Field Laboratory of Tohoku University and can produce magnetic fields of up to 5 T. An applied magnetic field B was perpendicular to the working electrode surface, and it was parallel (+ B) or antiparallel (- B) to the faradaic current. The films prepared at +5 T or -5 T are called the +5T-film or the -5T-film, respectively. The temperature within the magnet bore was controlled at 25°C by circulating thermoregulated water.

The magneto-electrodeposited (MED) films were used as modified electrodes, and their chiral properties were examined by measuring cyclic voltammograms (CVs) of the enantiomers of several kinds of amino acids (alanine, aspartic acid, lysine, etc.) in a 0.1 M NaOH aqueous solution. Because Cu metal is more easily oxidized than amino acids, the Cu film electrodes underwent a pretreatment of a potential sweep ($-0.3 \sim 0.3 \text{ V}$) in the NaOH solution before the CV measurements, as shown in Figure 2 (the solid line). In this potential sweep, the oxidation from Cu to Cu(I) occurs around -0.05 V , and the oxidation from Cu(I) to Cu(II) occurs around 0.02 V [14], forming a stable oxide film of CuO. The oxidation current became very small in the 2nd potential sweep (the dashed line in Figure 2), indicating that the film surface is covered by CuO after the pretreatment.

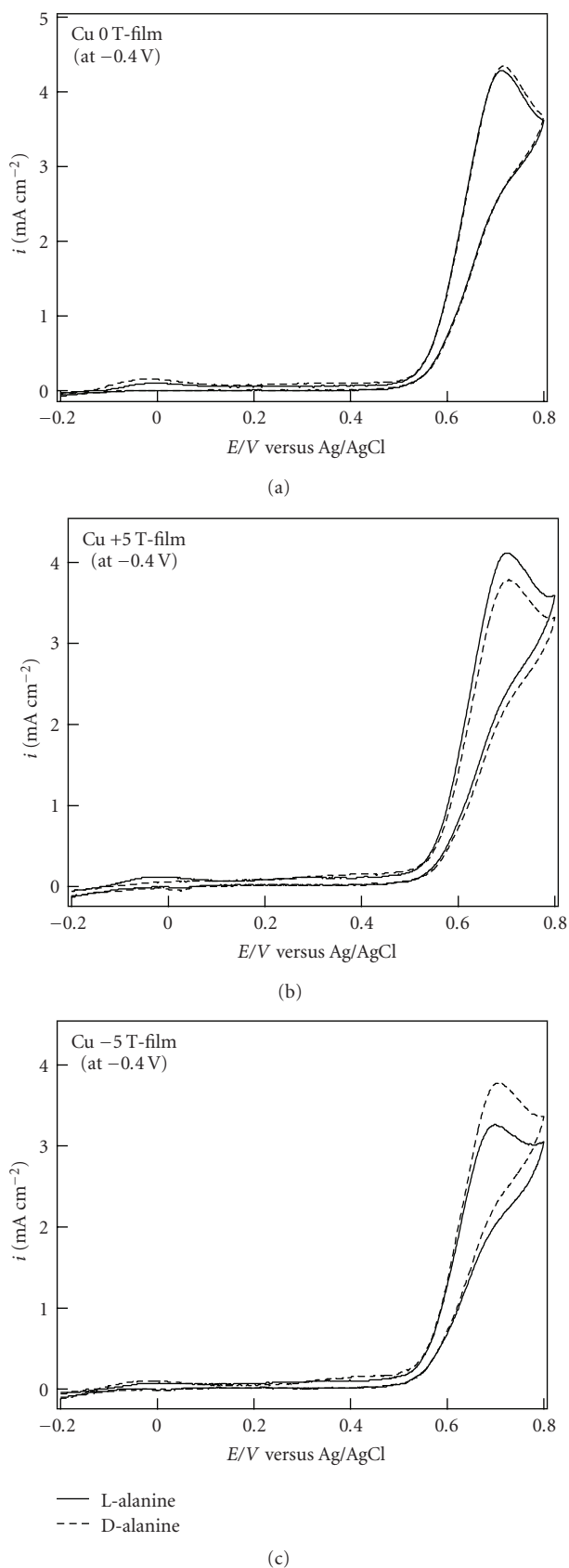


FIGURE 4: CVs of 20 mM L- and D-alanines on the Cu (a) 0T-film, (b) +5T-film, and (c) -5T-film electrodes in a 0.1 M NaOH aqueous solution. The potential sweep rate was 10 mV s^{-1} .

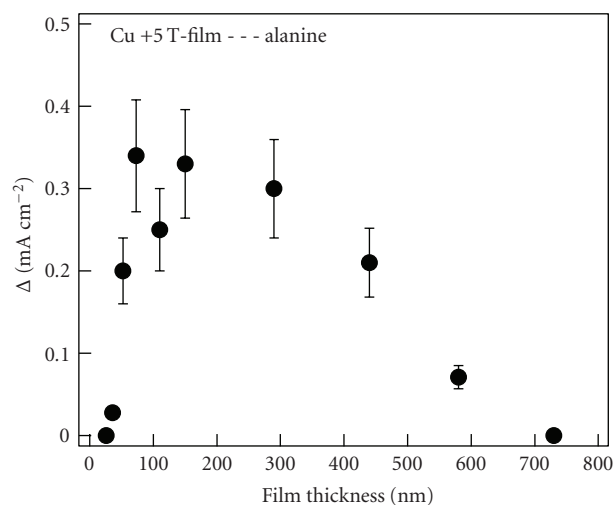


FIGURE 5: Film thickness dependence of the magnetochemical chirality. Δ is the peak current difference between L- and D-alanines in the CVs on the Cu +5T-film electrodes.

The CVs of amino acids were measured with a potential sweep rate of 10 mV s^{-1} in the absence of a magnetic field.

3. Results and Discussion

Figure 3 shows current-time curves during the Cu electrodeposition in 0 T and +5 T. It shows that the magnetic field considerably enhances the electrodeposition currents, even though the applied field is parallel to the faradaic current. The MHD effect is the minimum in, such a configuration, but it never disappears, because the current is not parallel to the magnetic field at the electrode edge and the fluctuated deposit surface. The latter is the micro-MHD effect [9], as mentioned above.

CVs of several amino acids were examined on the MED Cu film electrodes. Figure 4 shows CVs of 20 mM L- and D-alanines on the Cu (a) 0T-film, (b) +5T-film, and (c) -5T-film electrodes. The oxidation reaction of alanine occurs around 0.7 V, where the amino group ($-\text{NH}_2$) in the amino acid is oxidized [15]. Both CVs of the enantiomers are almost coincident each other on the 0T-film electrode (Figure 4(a)). On the +5T-film electrode, difference between the two CVs is seen in the peak currents. The oxidation current of L-alanine is larger than that of D-alanine (Figure 4(b)). On the contrary, the result is opposite for the MED film prepared under the reversal magnetic field. The oxidation current of D-alanine is larger than that of L-alanine on the -5T-film electrode (Figure 4(c)). These results indicate that the magneto-electrodeposition induces the chirality in the Cu films and that the MED films possess the ability of enantioselective recognition for L- and D-alanines. The fact that the chiral behavior depends on the polarity of the magnetic fields indicates that the chirality arises from the Lorentz force and micro-MHD effect.

Similar chiral behavior was observed in the MED Ag film electrode for the glucose oxidation reaction [12, 13]. Both

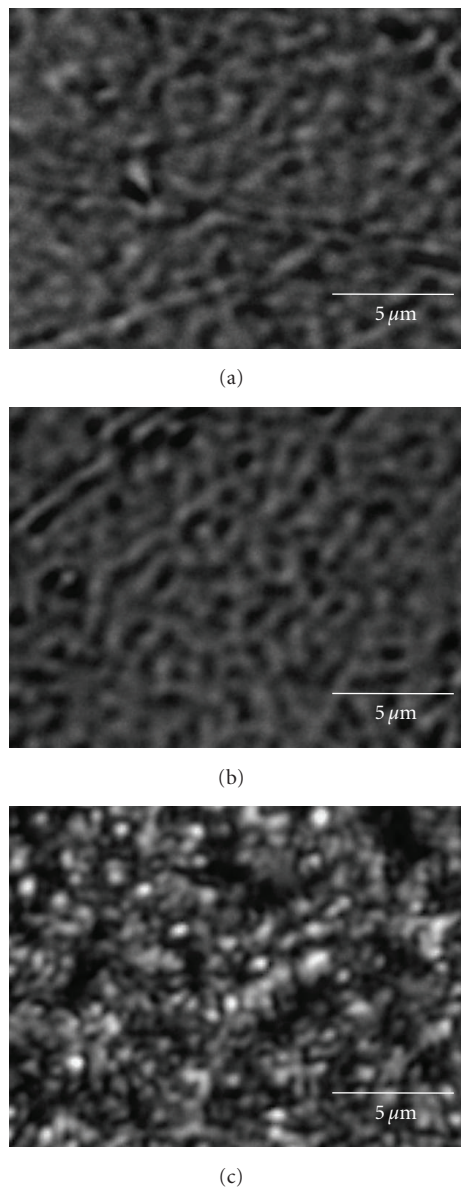


FIGURE 6: Microphotographs of the surface morphology of the Cu +5T-films with the thickness of (a) 150 nm, (b) 440 nm, and (c) 730 nm.

crystal structures of Ag and Cu are face-centered cubic (fcc), and generally, such a highly symmetrical crystal has no chirality. However, Attard et al. pointed out that there exist chiral kinks in certain surfaces, for example, {643}, of the fcc crystal and demonstrated that such a surface exhibits chiral electrode behaviors for the oxidation of D- and L-glucoses [16]. Similarly, they proposed that corner kinks of crystals could be a chiral site [17]. These ideas might be crucial for considering the chiral sites on the MED film surfaces.

The film thickness dependence of the chiral behavior of the +5T-film was examined for the electrochemical reaction of alanine. Figure 5 shows the oxidation current difference $\Delta (= i_p(L) - i_p(D))$ between the enantiomers against the film thickness, where $i_p(L)$ and $i_p(D)$ represent peak currents

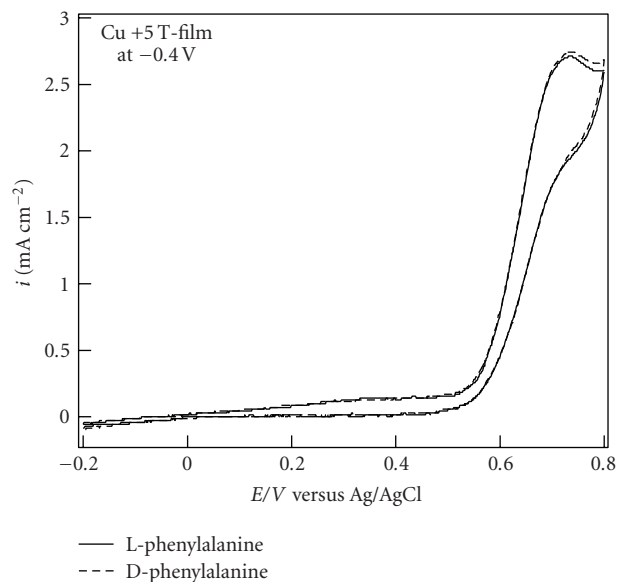


FIGURE 7: CVs of 20 mM L- and D-phenylalanines on the Cu +5T-film electrodes in a 0.1 M NaOH aqueous solution. The potential sweep rate was 10 mV s^{-1} .

of the CVs of L- and D-alanines, respectively. This figure shows that the chiral behavior appears in the thickness range of 50~500 nm. Figure 6 shows the surface morphologies of the Cu +5T-films with the thickness of (a) 150 nm, (b) 440 nm, and (c) 730 nm, where the photomicrographs were taken just after the magnetoelectrodeposition without the pretreatment. The films (a) and (b) exhibit the chiral behavior for alanine, and their surface morphologies possess network structures, which could be caused by the micro-MHD effect. Similar network structures were observed in the MED Ni- Al_2O_3 composite films [9] and magnetocorrosion of Zn single crystals [18]. On the contrary, the film (c) shows no chiral behavior, and the surface morphology is random aggregates of particles with a size of $\sim 1 \mu\text{m}$. These results imply that the micro-MHD effect induces the self-organization of convections and deposit structures in the film formation and that random fluctuation becomes dominant with increasing film thickness. Such self-organization seems to be significant for the formation of chiral surfaces.

We examined chiral response of the MED Cu film electrodes for several kinds of amino acids. Figure 7 shows CVs of 20 mM phenylalanine on the +5T-film electrode. The two CV curves are coincident each other, thus the MED film exhibits no chiral recognition for phenylalanine. This is contrary to the results of alanine, as shown in Figure 4. When amino acids are represented as $\text{R-CH}(\text{COOH})(\text{NH}_2)$, R is a methyl group ($-\text{CH}_3$) in alanine, and it is a benzyl group ($-\text{CH}_2\text{C}_6\text{H}_5$) in phenylalanine. The benzyl group is more bulky than the methyl group, and such a steric effect could prevent the specific adsorption at the chiral sites on the electrode surface, leading to the lack of chiral recognition.

Figure 8 shows CVs of 20 mM (a) aspartic acid, (b) glutamic acid, (c) lysine, and (d) arginine on the +5T-film electrode. While the MED film exhibits the chiral recognition

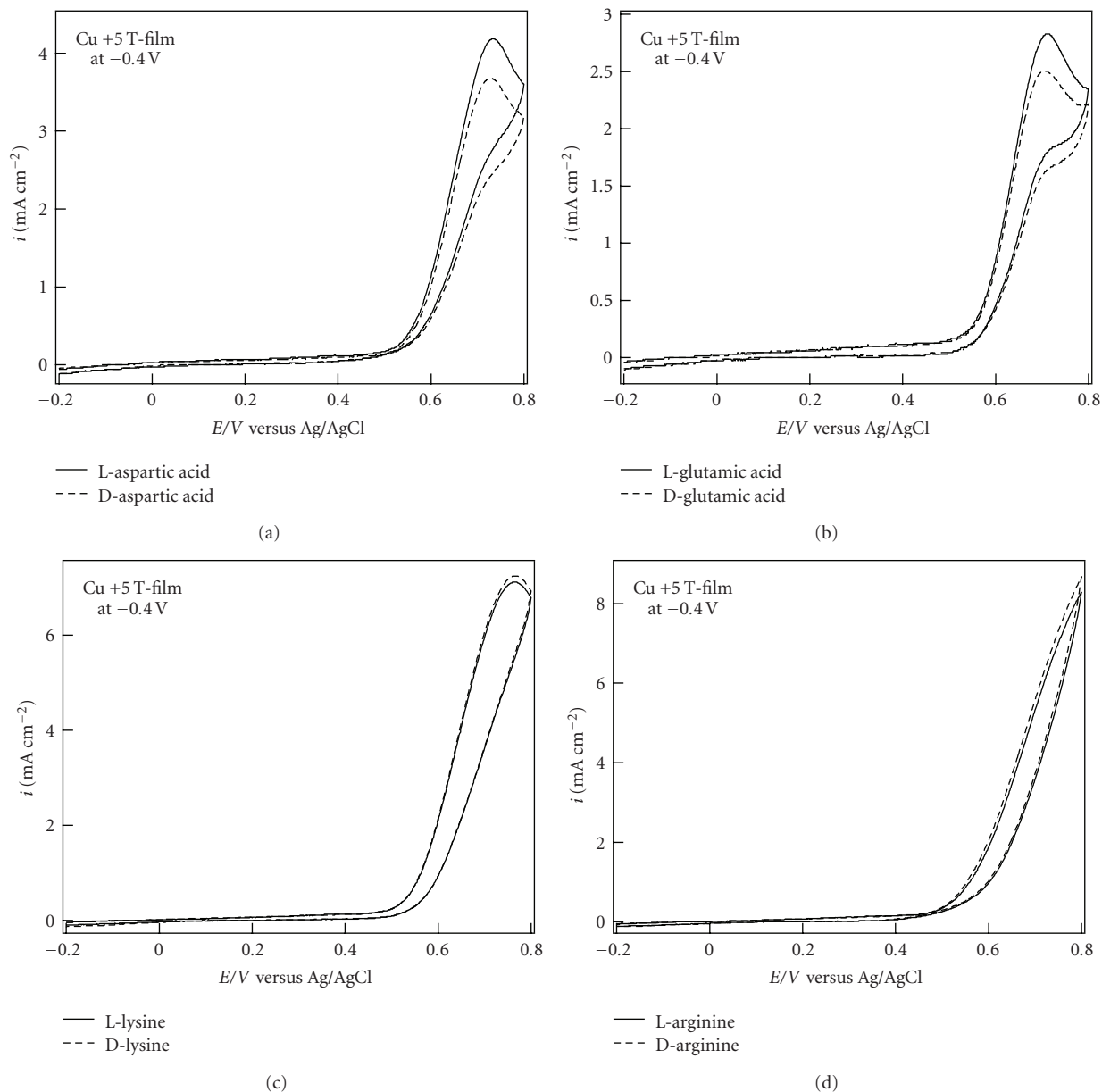


FIGURE 8: CVs of the enantiomers of (a) aspartic acid, (b) glutamic acid, (c) lysine, and (d) arginine on the Cu +5T-film electrodes in a 0.1 M NaOH aqueous solution. The potential sweep rate was 10 mV s^{-1} .

for aspartic and glutamic acids, it shows no chiral behavior for lysine and arginine. The molecular structures of R-groups are clearly different between the formers and the latter. The R-groups of aspartic and glutamic acids involve a carboxyl group ($-\text{COOH}$), on the contrary, those of lysine and arginine involve an amino group ($-\text{NH}_2$). These facts suggest that the carboxyl group promotes the specific adsorption on the electrode surface, leading to the chiral recognition. On the other hands, the amino group participates in the electrode reaction and contributes to the large oxidation currents, as shown in Figures 8(c) and 8(d). This seems to be crucial for the lack of chiral recognition for lysine and arginine.

There remains interesting open issues where the chiral site is on the MED film surface, why such a chiral site can survive after the surface oxidation in the pretreatment process, and how the chiral site recognizes the molecular chirality of amino acids. To elucidate these issues in future studies leads to a design of electrocatalytic chiral surface using the magnetoelectrodeposition technique.

4. Conclusion

We have shown that the MED Cu film electrodes exhibit chiral behaviors for the oxidation of the enantiomers of alanine,

aspartic acid, and glutamic acid and that such magnetoelectrochemical chirality depends on the film thickness. Taking account of our previous results of the chirality of the MED Ag films [12, 13], the observation of the chirality in the MED Cu films implies that the magnetoelectrochemical chirality is a universal phenomenon in the magnetoelectrodeposition of metals. It is noteworthy that the magnetoelectrodeposition is able to provide chiral surfaces without any chiral chemicals, and this novel technique would be applicable to new design of chiral catalysts and sensors.

Acknowledgment

The magnetoelectrochemical experiments were performed in the High Field Laboratory for Superconducting Materials, IMR Tohoku University.

References

- [1] R. Aogaki, K. Fueki, and T. Mukaibo, "Application of magnetohydrodynamic effect to the analysis of electrochemical reactions-1," *Denki Kagaku*, vol. 43, no. 9, pp. 504–508, 1975.
- [2] T. Z. Fahidy, "Magneto-electrolysis," *Journal of Applied Electrochemistry*, vol. 13, no. 5, pp. 553–563, 1983.
- [3] I. Mogi, S. Okubo, and Y. Nakagawa, "Dense radial growth of silver metal leaves in a high magnetic field," *Journal of the Physical Society of Japan*, vol. 60, no. 10, pp. 3200–3202, 1991.
- [4] I. Mogi, M. Kamiko, and S. Okubo, "Magnetic field effects on fractal morphology in electrochemical deposition," *Physica B*, vol. 211, no. 1–4, pp. 319–322, 1995.
- [5] J. M. D. Coey, G. Hinds, and M. E. G. Lyons, "Magnetic-field effects on fractal electrode deposits," *Europhysics Letters*, vol. 47, no. 2, pp. 267–272, 1999.
- [6] V. Heresanu, R. Ballou, and P. Molho, "Electrochemical growth of Zn and Fe arborescence under normal magnetic field," *Magnetohydrodynamics*, vol. 39, no. 4, pp. 461–469, 2003.
- [7] I. Mogi and M. Kamiko, "Pattern formation in magnetoelectropolymerization of pyrrole," *Denki Kagaku*, vol. 64, no. 7, pp. 842–844, 1996.
- [8] W. Duan, S. Kitamura, I. Uechi, A. Katsuki, and Y. Tanimoto, "Three-dimensional morphological chirality induction using high magnetic fields in membrane tubes prepared by a silicate garden reaction," *Journal of Physical Chemistry B*, vol. 109, no. 28, pp. 13445–13450, 2005.
- [9] R. Aogaki, "Micro-MHD effect on electrodeposition in the vertical magnetic field," *Magnetohydrodynamics*, vol. 39, no. 4, pp. 453–460, 2003.
- [10] T. Yamada and S. Asai, "Distribution control of dispersed particles in a film fabricated by composite plating method using a high magnetic field," *Journal of the Japan Institute of Metals*, vol. 69, no. 2, pp. 257–262, 2005.
- [11] R. Aogaki, R. Morimoto, A. Sugiyama, and M. Asanuma, "Origin of chirality in magnetoelectrodeposition," in *Proceedings of the 6th International Conference on Electromagnetic Processing of Materials*, pp. 439–442, Dresden, Germany, 2009.
- [12] I. Mogi and K. Watanabe, "Chiral electrode behavior of magnetoelectrodeposited silver films," *ISIJ International*, vol. 47, no. 4, pp. 585–587, 2007.
- [13] I. Mogi and K. Watanabe, "Magneto-electrochemical chirality in Ag electrodeposition," *Journal of Chemistry and Chemical Engineering*, vol. 4, no. 11, pp. 16–22, 2010.
- [14] N. Torto, T. Ruzgas, and L. Gorton, "Electrochemical oxidation of mono- and disaccharides at fresh as well as oxidized copper electrodes in alkaline media," *Journal of Electroanalytical Chemistry*, vol. 464, no. 2, pp. 252–258, 1999.
- [15] P. Luo, F. Zhang, and R. P. Baldwin, "Constant potential amperometric detection of underivatized amino acids and peptides at a copper electrode," *Analytical Chemistry*, vol. 63, no. 17, pp. 1702–1707, 1991.
- [16] G. A. Attard, C. Harris, E. Herrero, and J. Feliu, "The influence of anions and kink structure on the enantioselective electro-oxidation of glucose," *Faraday Discussions*, vol. 121, pp. 253–266, 2002.
- [17] G. A. Attard, A. Ahmadi, D. J. Jenkins et al., "The characterisation of supported platinum nanoparticles on carbon used for enantioselective hydrogenation," *ChemPhysChem*, vol. 4, no. 2, pp. 123–130, 2003.
- [18] K. Shinohara, K. Hashimoto, and R. Aogaki, "Hexagonal corrosion pattern upon cleavage of a zinc single crystal under a vertical high magnetic field," *Chemistry Letters*, vol. 31, no. 8, pp. 778–779, 2002.